NUCLEOPHILE ASSISTED CARBON DIOXIDE FIXATION FOR A CLEANER ENVIRONMENT

By

SHAUN REDGARD

February 2019

NUCLEOPHILE ASSISTED CARBON DIOXIDE FIXATION FOR A CLEANER ENVIRONMENT

By

SHAUN REDGARD

A dissertation submitted to meet the requirements for the degree of

MAGISTER SCIENTIAE

in the

DEPARTMENT OF CHEMISTRY

in the

FACULTY OF NATURAL AND AGRICULTURAL SCIENCES

at the

UNIVERSITY OF THE FREE STATE

Supervisor

PROF. ANDREAS ROODT

February 2019

Acknowledgements

All my thanks and appreciation are foremost given to God who has granted me wisdom and knowledge through all the trials and tribulations that I have experienced in my life thus far. So that regardless of my endeavour and its result, I will always give thanks to God.

Thank you Prof. Andreas Roodt for taking me on as a student and being my supervisor. Your approach towards critical thinking and rarely accepting the norm, especially towards chemistry has helped better shape my vision towards life. Most importantly, thank you for not leading me with my research but rather guiding me so that I may form my own paths.

Dr. Kama, Dr. Mokolokolo and Dr. Alexander, thank you being great friends and for helping me with my endless and sometimes needless questions. Also, thank you for all the jokes, support and random conversations.

Thank you Dr. Koen for helping me with jokes and advice over the holidays to assist me as best you could, without complaining too much.

Zaskia, thank you for supporting me during the final months of my dissertation. I know it was not always easy, but it would have been a lot more difficult without you.

To my parents, Mike and Elize Redgard, thank you for being patient and supportive of me and allowing me to follow my dreams unrestricted. I will always love you for it.

Lastly, I would like to thank the University of the Free State and SASOL for the financial assistance they provided towards this research.

~ The laws of nature are the thoughts of God ~

Table of Contents

Abbreviations

Abbreviation	Description
CO_2	Carbon dioxide
ppm	Parts per million
nm	Nanometre
DBU	1,8-diazabicyclo[5.4.0]undec-7-ene
DBN	1,5-diazabicyclo[4.3.0]non-5-ene
TBD	1,5,7-triazabicyclo[4.4.0]dec-5-ene
TMG	1,1,3,3-tetramethylguanidine
COD	1,5-Cyclooctadiene
DMAP	4-dimethylaminopyridine
IR	Infrared
NMR	Nuclear magnetic resonance
SC-XRD	Single crystal X-ray diffraction
UV/Vis	Ultra-violet/ visible
^{o}	Degree
^{o}C	Degrees Celsius
K	Kelvin
Å	Angstrom
$\bar{\nu}$	IR stretching frequency (cm^{-1})
λ	Wavelength (nm)
δ	Chemical shift (ppm)
A	Absorbance
k_{obs}	Observed rate constant
k_1	Rate constant (forward reaction)
k_{-1}	Rate constant (reverse reaction)
K_1	Equilibrium constant

Abbreviation	Description
ψ	*Jaw* angle
χ	*Bite* angle
τ	*twist* angle
$\Delta H^{\neq}$	Standard enthalpy change of activation
$\Delta S^{\neq}$	Standard entropy of activation
$\Delta G^{\neq}$	Gibbs free energy of activation
mg	Milligram
mmol	Millimole
µl	Microliter
M	$mol \cdot dm^{-3}$
$CDCl_3$	Deuterated chloroform
C_6D_6	Deuterated benzene

Abstract

Nature has perfected CO_2-fixation in plants through the C_3, C_4 and CAM (crassulacean acid metabolism) mechanisms. Thus, by applying a biomimetic approach to CO_2-fixation the knowledge and approach can be ameliorated. This led to the identification of four "non-nucleophilic" bases, which can be categorized as amidines or guanidines, that have an innate ability to coordinate to CO_2. The amidines were 1,8-diazabicyclo[5.4.0]undec-7-ene (**DBU**) and 1,5-diazabicyclo[4.3.0]non-5-ene (**DBN**) and the guanidines were 1,5,7-triazabicyclo[4.4.0]dec-5-ene (**TBD**), 1,1,3,3-tetramethylguanidine (**TMG**).

Overall, the main pursuit of this study was to elucidate on the relevant aspects pertaining to the assimilation and activation pathways of CO_2. This was performed by firstly confirming the coordination ability of the bases to CO_2 through preliminary solution studies, which indicated that TBD had the strongest ability followed by DBU, DBN and TMG. Thereafter, two model complexes were identified in literature that contained the bases. The general formulae for the two model complexes that were synthesized and characterized were *trans*-$[Pd(L)_2Cl_2]$ and [Rh(L)(COD)Cl] (L = (DBU, DBN, TMG, TBD)), except for the TBD-Rh(I) complex.

Of the complexes synthesized, three yielded single crystals, of which two were novel complexes, that were suitable for single-crystal X-ray diffraction (SC-XRD); namely *trans*-$[Pd(DBN)_2Cl_2]$, [Rh(COD)(DBU)Cl] and [Rh(COD)(TMG)Cl]. The novel Pd(II) complex packed centrosymmetrically, while the Rh(I) complexes were evaluated on the influence the bases had on the 1,5-cyclooctadiene (COD) conformation by assessing three dihedral angles within the COD. Of the three angles, the most significant difference is seen in the *jaw* angle (ψ) – between the two complexes (ψ = 75.3(3)° and 64.7(4)° for the DBU and TMG complexes respectively). This was attributed to increased electron density in the π antibonding orbitals on the metal centre, for the latter complex, which resulted in an increase in steric hindrance from the metal centre towards the back-bones of the COD. Therefore, in theory, substitution reactions of the bases by other strong bases would lead to a faster reaction in the TMG-containing complex as opposed to the DBU-Rh(I) complex. This is due to increased reactivity from the two electron donating pathways (σ and π donation) to the metal centre aiding the π back-donation to the diolefin.

This notion was confirmed through extremely fast substitution kinetic reactions observed in the two Rh(I) complexes by 4-dimethylaminopyridine (DMAP) at different temperatures, because the leaving group (being DBU or TMG) determines the rate of attack based on its electron density contribution to the metal centre. Furthermore, the substitution reaction followed a typical and classical associative mechanism and was supported by the negative $\Delta S^{\neq}$ value determined for both complexes. The forward rate constant k_1 was ten times slower and *ca.* 3 % less entropy driven for the DBU-complex than for the TMG-complex, with neither experiencing a strong solvation/reverse pathway.

Thus, similar rates may be achieved with CO_2 but the rate being limited by the initial activation of CO_2 by the bases. Additionally, the large solvent pathway may add to the reaction by performing the reaction under supercritical CO_2.

Keywords: CO_2, DBU, DBN, TMG, TBD, DMAP, COD, X-ray diffraction, kinetic reactions.

Opsomming

Die natuur het CO_2-fiksering in plante deur middel van die C3, C4 en CAM ("Crassulacean"-suurmetabolisme) meganismes vervolmaak. Dus, deur die toepassing van 'n biomimetiese benadering tot CO_2-fiksering kan die fundamentele kennis uitgebrei word. Dit het gelei tot die identifisering van vier "nie-nukleofiele" basisse, wat as amidiene of guanidiene gekategoriseer kan word, wat 'n inherente vermoë het om CO_2 te koördineer. Die amidiene was 1,8-diazadisiklo[5.4.0]undek-7-een (**DBU**) en 1,5-diazadisiklo[4.3.0]non-5-een (**DBN**) en die guanidiene was 1,5,7-triazadisiklo[4.4.0]dek-5-een (**TBD**), 1,1,3,3-tetrametielguanidien (**TMG**).

Die hoofdoel van hierdie studie om relevante aspekte rakende die assimilasie- en aktiveringsbane van CO_2 te ondersoek. Dit is bewerkstellig deur eerstens die koördinasievermoë van die basisse aan CO_2 te evalueer deur middel van voorlopige oplossingstudies, wat daarop dui dat TBD die sterkste vermoë het, gevolg deur DBU, DBN en TMG. Daarna is twee modelkomplekse in die literatuur geïdentifiseer wat die basisse bevat. Die algemene formules vir die twee modelkomplekse wat gesintetiseer en gekarakteriseer, was *trans*-$[Pd(L)_2Cl_2]$ en [Rh(L)(COD)Cl] (L = (DBU, DBN, TMG, TBD)).

Van die komplekse wat gesintetiseer is, het drie enkelkristalle gelewer, waarvan twee nuwe komplekse was en geskik vir enkel-kristal X-straaldiffraksie; naamlik *trans*-$[Pd(DBN)_2Cl_2]$, [Rh(COD)(DBU)Cl] en [Rh(COD)(TMG)Cl]. Die nuwe Pd(II) kompleks het sentrosymmetries gepak. Die Rh(I) komplekse is geëvalueer deur middel van die invloed wat die basisse op die konformasie van 1,5-siklooktadieen (COD) gehad het, soos gemanifesteer deur drie hoeke binne die COD. Vanuit hierdie drie hoeke is die belangrikste verskil in die kaakhoek (Eng. Jaw angle) (ψ) waargeneem - tussen die twee komplekse (ψ = 75.3 (3) ° en 64.7 (4) ° vir die DBU en TMG komplekse onderskeidelik). Dit is toegeskryf aan verhoogde elektrondigtheid in die π-antibindingsorbitale op die metalsentrum, vir laasgenoemde kompleks, wat gelei het tot 'n toename in steriese interaksie met die ruggraat van die COD. Gevolglik in teorie, sal substitusiereaksies van hierdie basisse deur ander sterk nukleofiele lei tot 'n vinniger reaksie in die TMG-bevattende kompleks in teenstelling met die DBU-Rh(I) kompleks. Dit is te wyte aan verhoogde reaktiwiteit

van die twee elektrondonerende interaksies (σ en π) aan die metalsentrum wat die π terugdonering aan die diolefin help.

Hierdie is bevestig deur middel van baie vinnige substitusiekinetiese reaksies wat by verskillende temperature in die twee Rh(I) komplekse deur 4-dimetielaminopiridien (DMAP) waargeneem word, omdat die verlatende groep (DBU of TMG) die tempo van aanval bepaal op grond van die elektrondigtheidsbydrae tot die metaal sentrum. Verder het die substitusiereaksie 'n tipiese en klassieke assosiatiewe meganisme gevolg soos afgelei van die negatiewe $\Delta S^{\neq}$ waarde wat vir beide komplekse waargeneem is. Die voorwaartse tempokonstante k_1 was tien keer stadiger en ongeveer 3% minder entropie gedrewe vir die DBU-kompleks in vergelyking met die TMG-kompleks, en het nie 'n sterk oplosmiddel/ terugwaartse getoon nie.

Dus, soortgelyke tempos kan met CO_2 behaal word, maar die relatiewe tempo sal afhang van die aanvanklike aktivering van CO_2 deur die basisse. Daarbenewens kan die groot oplosmiddelpad bydrae tot die reaksie, deur dit onder superkritiese CO_2 uit te voer.

Sleutelwoorde: CO_2, DBU, DBN, TMG, TBD, DMAP, COD, X-straal diffraksie, kinetiese reaksie.

1 Aim of the study

What to expect

General overview of carbon dioxide (CO_2) pollution, and its fixation in nature and in organic and organometallic systems, followed by the aims of the study.

1.1 Introduction

The world has been migrating to a more environmentally conscious approach to the future for the past two decades. This is due to the damage being done to all the ecosystems, including those not inhabited by people. Various forms of pollution contribute to the effect on the ecosystems, namely water, land and air pollution – due to the industrialization of natural resources. The major pollutant that is emitted, is considered to be anthropogenic carbon dioxide (CO_2), which is one of the many gases that contribute to the greenhouse effect. In April 2018, CO_2 concentrations in the atmosphere reached a record high of 410 ppm [1], and the concern is that there is no cost-effective option to reduce the levels of CO_2 in the atmosphere. Moreover, although governments are introducing stricter emission laws to reduce the rate of greenhouse gas emissions such as the Paris Agreement, this does not mitigate the need to reduce the overall gas emissions in the atmosphere [2].

An issue with CO_2 is that it is a very inert and stable gas. The consequence of this is that it has poor reactivity and needs to be activated through either the electrophilic carbon or nucleophilic oxygens, since the brute electrochemical approach is energy intensive [3]. The irony is that nature has perfected CO_2 storage and fixation in biological systems through various mechanisms and cycles, most notably, photosynthesis in plants [4–6]. Thus, through the study of biomimetic systems (human imitation of models/ systems from nature) such as photosynthesis, a better understanding may be achieved by which synthetic systems or models can be utilized to reduce the rate or levels of anthropogenic CO_2 being emitted [7].

The primary purpose of photosynthesis is energy storage in the form of carbohydrates [4]. This is achieved through a series of steps where CO_2 is activated and fixated, with the energy being

supplied by light photons with a specific wavelength (400 nm to 700 nm). These photons are absorbed by chlorophyll and, by means of charge separation, the photon energy is transferred to an electron and goes through an electron chain to eventually produce adenosine triphosphate (ATP) and nicotinamide adenine dinucleotide phosphate hydrogen (NADPH) [4]. Both ATP and NADPH play a role in CO_2 fixation by supplying the energy for both the ribulose-1,5-bisphosphate carboxylase/oxygenase (RuBisCO) enzyme, which produces 3-phosphoglyceraldehyde (G3P), and the Calvin cycle to subsequently form carbohydrates. However, CO_2 is also stored in the form of malic acid or oxalic acid by the phosphoenolpyruvate carboxylase (PEPc) enzyme in certain plants, and decarboxylated at a later point to be used in the above-mentioned processes [5,6].

1.2 Organic and organometallic biomimetic systems

With biomimetics in mind, CO_2 fixation/storage via organic and organometallic systems have shown promise. A recurring factor in both systems is the presence of amidine and guanidine bases (Fig. 1.1). The two prominent amidines that feature often are 1,8-diazabicyclo[5.4.0]undec-7-ene (DBU) and 1,5-diazabicyclo[4.3.0]non-5-ene (DBN), and for guanidine are 1,5,7-triazabicyclo[4.4.0]dec-5-ene (TBD) and 1,1,3,3-tetramethylguanidine (TMG) [8].

The reoccurring appearance of these four bases in nature can be attributed to their ability to coordinate to CO_2 in solution and form carbonate and carbamate salts [9,10]. This led researchers to incorporate amidines and guanidines into other organic systems with switchable ionic liquids (SWILs) to capture CO_2 and be able to remove it by sparging with an inert gas or by heating [11]. Additionally, in 2017 Seipp *et al*. created a TMG-containing ligand (2,6-pyridine-bis(iminoguanidine)) that in aqueous solution could absorb CO_2 from ambient air and be released through heating [12]. In the Morita-Baylis-Hillman reaction, an activated alkene derivative is coupled to an aldehyde in the presence of 1,4-diazabicyclo[2.2.2]octane triethylenediamine (DABCO) as the catalyst, but when DABCO was replaced by DBU the reaction time decreased from 96 hours to 6 hours and the yield was greater in the latter case (87% and 89% respectively) [13,14].

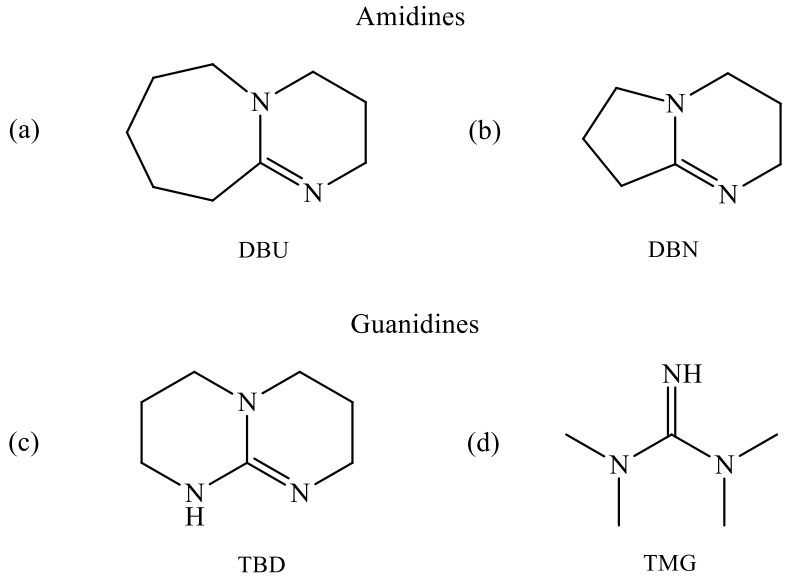

Figure 1.1: Chemical structures of the two types of amidines; (a) 1,8-diazabicyclo[5.4.0]undec-7-ene (**DBU**), (b) 1,5-diazabicyclo[4.3.0]non-5-ene (**DBN**), and guanidines; (c) 1,5,7-triazabicyclo[4.4.0]dec-5-ene (**TBD**), (d) 1,1,3,3-tetramethylguanidine (**TMG**) [8].

One metal catalyst that performed exceptionally well in the presence of DBU, as a cocatalyst, was the catalyst $[Ru(OAc)(PMe_3)_4]$ in supercritical carbon dioxide ($scCO_2$), pentafluorophenol and H_2 resulted in a turnover frequency (TOF) that was too excessive to measure with the equipment [15]. However, the reaction with the base, triethylamine (NEt_3), had a TOF of 95000 h^{-1}, but preliminary tests on the reaction rate showed that the NEt_3 was ten times slower than DBU, which illustrates the possibly larger TOF that could be expected for DBU.

Due to amidines and guanidines being able to activate CO_2, their presence as a co-catalyst or ligand on metal complexes have yielded improved turnover numbers (TON), turnover frequencies (TOF) and product selectivity when compared to prior ligands and co-catalysts, even in CO_2-free reactions, as illustrated in the above examples. In addition to the above mentioned examples, the catalyst *trans*-$[Pd(DBU)_2Cl_2]$ was used for the selective double carbonylation or aryl iodides with 90% selection and 91% selectivity in place of the prior used phosphine ligands [16]. Another catalyst, [Rh(DBU)(COD)Cl], which was patented for its ability to hydrogenate double bonds, notably a C=N or C=C double bond, illustrated different reaction examples with their TON values – the largest TON of 329 was recorded for the hydrogenation of oleic acid to stearic acid [17,18].

1.3 Aim of the study

Based on the above information, guanidines and amidines have shown to play an active role in CO_2 fixation, though not exclusively, as evident by some of the mentioned examples. The use of compounds which mitigate the energy requirement for CO_2 activation and fixation, be it through organic or organometallic catalysts, require more insight to better understand and develop improved systems to reduce CO_2 levels. Thus, a study of the mechanistic and kinetic pathways by which CO_2 is activated by biological, organic or organometallic systems may assist in identifying further research approaches towards CO_2 as a C_1-feedstock as performed through nature.

In this study, the amidines (DBU and DBN) and guanidines (TBD and TMG) were evaluated to further understand their ability to activate CO_2. Furthermore, the complexes; *trans*-[$Pd(DBU)_2Cl_2$] and [Rh(DBU)(COD)Cl] were chosen as model complexes with the general formulae *trans*-[$Pd(L)_2Cl_2$] and [Rh(L)(COD)Cl] (L = (DBU, DBN, TMG, TBD)) , due their ability to carbonylate (former complex) and hydrogenate double bonds (latter complex).

Considering the above, a set of stepwise aims were set for the study.

1. Research the environmental contribution of numerous pollutants and understand the contribution of CO_2 and its influences.
2. Develop an improved understanding of the different ways in which CO_2 fixation and storage occurs in nature, namely C_3, C_4 and CAM plants for biomimetic application.
3. Identify organic systems/ nucleophiles which perform or show promise for CO_2 fixation.
4. Identify organometallic systems that can be enhanced through application of the organic systems identified in the previous step.
5. Synthesize and evaluate organic and metal systems through IR, ^{1}H and ^{13}C NMR spectroscopy and use single-crystal XRD (X-ray diffraction) to elucidate examples of structures and evaluate coordination modes within these systems.
6. Preliminary kinetic and mechanistic comparison study of neutral ligand substitution reactions by means of UV/Vis spectroscopy associated with these bases' solution and coordination behaviour.
7. Analysis of results with respect to CO_2 fixation and literature.

CHAPTER 1

The first four aims are addressed in the following chapter, as a brief literature review, to motivate the study of CO_2-fixation through the identified organic and organometallic systems. Following that, three experimental chapters are presented which covers the last three aims. Finally, the dissertation concludes with an evaluation of the study based on the results from the final aim.

1.4 References

[1] R. A. Berner, "A History of Atmospheric CO2 and Its Effects on Plants, Animals, and Ecosystems", **177,** *Springer New York*, (2005)

[2] C. Streck, P. Keenlyside, & M. von Unger Atlas, "The Paris Agreement: A New Beginning", *J. Eur. Environ. Plan. Law*, **13,** 1–27 (2016).

[3] L. J. Murphy, K. N. Robertson, R. A. Kemp, H. M. Tuononen, & J. A. C. Clyburne, "Structurally simple complexes of CO2", *Chem. Commun.*, **51,** 3942–3956 (2015).

[4] S. Berardi, S. Drouet, L. Francàs, C. Gimbert-Suriñach, M. Guttentag, C. Richmond, T. Stoll, & A. Llobet, "Molecular artificial photosynthesis", *Chem. Soc. Rev.*, **43,** 7501–7519 (2014).

[5] J. Shi, Y. Jiang, Z. Jiang, X. Wang, X. Wang, S. Zhang, P. Han, & C. Yang, "Enzymatic conversion of carbon dioxide", *Chem. Soc. Rev.*, **44,** 5981–6000 (2015).

[6] A. Bar-Even, E. Noor, N. E. Lewis, & R. Milo, "Design and analysis of synthetic carbon fixation pathways", *Proc. Natl. Acad. Sci.*, **107,** 8889–8894 (2010).

[7] J. F. V. Vincent, O. A. Bogatyreva, N. R. Bogatyrev, A. Bowyer, & A. K. Pahl, "Biomimetics: Its practice and theory", *J. R. Soc. Interface*, **3,** 471–482 (2006).

[8] T. Ishikawa, "Superbases for Organic Synthesis", *John Wiley & Sons, Ltd*, (2009)

[9] D. J. Heldebrant, P. G. Jessop, C. A. Thomas, C. A. Eckert, & C. L. Liotta, "The Reaction of 1,8-Diazabicyclo[5.4.0]undec-7-ene (DBU) with Carbon Dioxide", *J. Org. Chem.*, **70,** 5335–5338 (2005).

[10] F. S. Pereira, E. R. deAzevedo, E. F. da Silva, T. J. Bonagamba, D. L. da Silva Agostíni, A. Magalhães, A. E. Job, & E. R. Pérez González, "Study of the carbon dioxide chemical fixation-activation by guanidines", *Tetrahedron*, **64,** 10097–10106 (2008).

[11] J. Yao, D. B. Lao, X. Sui, Y. Zhou, S. K. Nune, X. Ma, T. P. Troy, M. Ahmed, Z. Zhu, D. J. Heldebrant, & X.-Y. Yu, "Two coexisting liquid phases in switchable ionic liquids", *Phys. Chem. Chem. Phys.*, **19,** 22627–22632 (2017).

[12] C. A. Seipp, N. J. Williams, M. K. Kidder, & R. Custelcean, "CO 2 Capture from Ambient Air by Crystallization with a Guanidine Sorbent", *Angew. Chemie Int. Ed.*, **56,** 1042–1045 (2017).

[13] J. E. Taylor, S. D. Bull, & J. M. J. Williams, "Amidines, isothioureas, and guanidines as nucleophilic catalysts", *Chem. Soc. Rev.*, **41,** 2109–2114 (2012).

[14] V. K. Aggarwal, & A. Mereu, "Superior amine catalysts for the Baylis-Hillman reaction: The use of DBU and its implications", *Chem. Commun.*, 2311–2312 (1999).

[15] P. Munshi, A. D. Main, J. C. Linehan, C. C. Tai, & P. G. Jessop, "Hydrogenation of carbon dioxide catalyzed by ruthenium trimethylphosphine complexes: The accelerating effect of certain alcohols and amines", *J. Am. Chem. Soc.*, **124,** 7963–7971 (2002).

[16] V. De La Fuente, C. Godard, E. Zangrando, C. Claver, & S. Castillón, "A phosphine-free Pd catalyst for the selective double carbonylation of aryl iodides", *Chem. Commun.*, **48,** 1695–1697 (2012).

[17] L. Jiang, J. Timothy, & F. Zou, "Catalytic hydrogenation",Patent no. US8242318B2, 1–7 (2012).

[18] U. Flörke, U. Ortmann, & H. J Haupt, "Rhodium(I)-cyclooctadiene (cod) complexes with the N-donor ligands 1,8-diazabicyclo[5.4.0]undec-7-ene (dbu) and 1,5-diazabicyclo[4.3.0]non-5-ene (dbn)", *Acta Crystallogr. Sect. C,* **48,** 1663–1665 (1992).

2 Literature review related to this study

What to expect

This chapter elucidates on pollution, specifically carbon dioxide (CO_2), and current control and reduction methodologies. The naturogenic CO_2 fixation pathway is additionally discussed, which relates research on past and present biomimetic systems that uses natures blueprint to recycle CO_2.

2.1 Introduction

With the world shifting to a more environmentally friendly approach to all aspects of life, stricter laws, such as the Paris Agreement, are continually being integrated to achieve this [1]. To better facilitate the transition, researchers are focusing more on using less environmentally hazardous chemicals, as well as attempting to reduce those chemicals that are already present in the environment; namely CO_2. A few valuable aspects that relate to CO_2 fixation and storage will be presented in this chapter.

2.2 Environmental Pollution

The world is plagued with various forms of pollution that damage and change our ecosystems. The major forms of pollution that contribute to this are mentioned below:

- Air pollution
- Light pollution
- Littering
- Noise pollution
- Plastic pollution
- Soil contamination
- Radioactive pollution
- Water pollution

These forms of pollution can be attributed to two groups; naturogenic (natural-made) and anthropogenic (human generated), with the largest being air pollution because of its 'butterfly effect' which has consequential effects on all ecosystems. The butterfly effect can be defined as the sensitive dependence on the primary state in which a minimal change can result in large differences at a later point [2]. To better understand this concept, air pollution can again be divided into two groups; particulate matter (PM) and greenhouse gases (GHGs).

Particulate matter are microscopic solids/liquids that are suspended in the atmosphere, with those having the greatest effect, consisting of a size between 2.5 μm ($PM_{2.5}$) and 10 μm (PM_{10}). Examples of these particulates are; pollen, dust, allergens, black carbon (BC), organic carbon compounds, chemical salts and heavy metals [3]. Though they contribute to climate change, their biggest influence is on human health because they are able to penetrate the lungs and bloodstream unfiltered, resulting in lung cancer, heart attacks and DNA mutations, to mention a few. As a result, they are designated as group 1 carcinogens by the International Agency for Research on Cancer (IARC) and the World Health Organization (WHO) and can clearly be seen as the deadliest direct form of pollution [4,5].

Though it is a cause for concern, GHGs reek more havoc indirectly and contributes the majority to the 'butterfly effect' known as global warming, which is the measured average increase in global temperatures, due to GHGs, and its related effects. Radiative forcing (RF) is used to measure the influence that a given climatic factor has on the amount of radiant energy, which is downward-directed, that strikes the Earth's surface [6]. Climatic factors that cool the Earth's surface exert 'negative forcing' and those that increase the temperature exert 'positive forcing'.

Though chlorofluorocarbons (CFCs) and hydrochlorofluorocarbons (HCFCs) contribute to radiative forcing, those that contribute the most, in increasing order, are three of the long-lived greenhouse gases (LLGHGs); nitrous oxide (N_2O), methane (CH_4) and carbon dioxide (CO_2). The Annual Greenhouse Gas Index (AGGI), by the National Oceanic and Atmospheric Administration (NOAA), represents the annual collective RF of the LLGHGs with respect to the Kyoto Protocol baseline year (1990) which had a value of 2.16 Wm^{-2}. The aim of this agreement is to reduce greenhouse gas emissions with regards to the baseline year. The total RF attributed to the

LLGHGs, in 2017, was 3.06 Wm^{-2}; nitrous oxide, which is also an ozone-depleting substance, contributed 6.5% (0.2 Wm^{-2}), methanol made up 16% (0.5 Wm^{-2}) and CO_2 consisted of 66% (2.01Wm^{-2}) [7].

The resulting increase in temperatures has several consequences. The most well-known effect is probably the melting of the polar caps which leads to increased sea levels. However, permafrost, which is ground that is at or below the freezing point of water, is also present at the polar caps and will release dormant methane gas that will contribute further to the greenhouse effect. Another cause of increased temperatures is coral bleaching, which is when corals release algae that live within them that turn the corals white and can also result in their death [7]. The increase also influences weather patterns due to a higher humidity and dryer air, which in turn causes more natural disasters. This is exacerbated by the El Niño phenomenon which disrupts normal weather patterns, resulting in heavier rains and droughts, as well as a possible increase in CO_2 levels due to several factors such an increased CO_2 emission by plants in Africa and reduced absorption by growing plants in South America [7]. The El Niño phenomena are due to the warmer than normal waters in the Pacific Ocean and occurs every two to seven years, while approximately every 20 years a 'super' El Niño occurs which causes more extreme weather patterns, yet this number may reduce to every 10 years if temperatures continue to increase.

There are two other alleged effects of increased temperature to humanity, a higher crime and suicide rate [8,9]. In the case of the former, when temperatures rose above 1 ºC of the seasonal average, in the United Kingdom, there was a 2 % increase in crime compared to the normal and the opposite held true when the temperature decreased by more than 1 ºC. In terms of suicide, a study found that, in the United States and Mexico, the suicide rate increased by 0.7 % and 2.1 % respectively when the temperatures increased by 1 ºC compared to the monthly average. While the alleged influence of temperature on these factors are interesting a global study may confirm its influences to know if crime and suicide are additional factors to be concerned about due to global warming.

Considering the large impact that higher temperatures have, further understanding is required on the largest contributor to the greenhouse effect i.e. CO_2.

2.3 Carbon dioxide (CO_2)

Most of the CO_2 released into the atmosphere is the result of the combustion of carbon containing compounds for energy utilization. These carbon containing compounds come in the form of three fossil fuels; natural gas, coal and petroleum. Since the start of the industrial revolution, in 1750, approximately 400 billion tons CO_2 has been released due to fossil fuel consumption and cement production. However, ***half*** of these CO_2 emissions has been released only since the 1980s [10]. In 2014, anthropogenic emissions already accounted for about 9855 million metric tons of CO_2, solid and liquid fuels accounted for 75.1%, gas fuels made up for 18.5% and cement production released about 5.8 % of CO_2, with gas flaring contributing less than 1% (Fig. 2.1) [10]. Recent estimates have calculated that approximately half of the CO_2 emission remains in the atmosphere and that about a quarter goes to plants, with the rest being absorbed by the oceans.

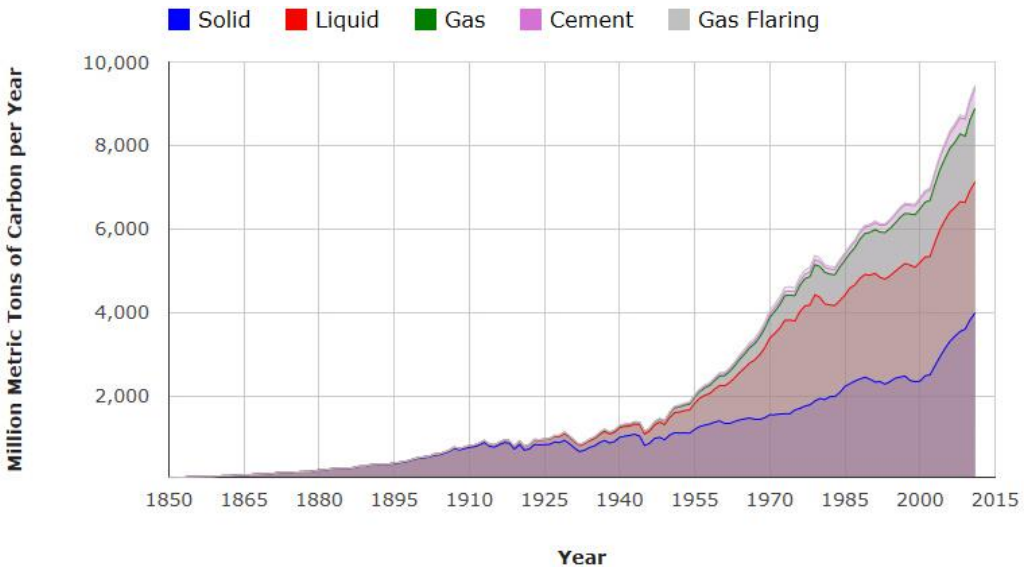

Figure 2.1: The total aggregate anthropogenic CO_2 contributors until 2014, with the contributors being added on top of one another from left (solid; blue) to right (gas flaring; grey) [10].

Carbon dioxide emissions in the atmosphere have been continuously measured, since 1958, at the Mauna Loa observatory (MLO) in Hawaii by Charles Keeling, with the resulting data producing what is often referred to as the Keeling Curve (Fig. 2.2). The abundance of atmospheric CO_2 was approximately 315 ppm (parts per million in dry air) in that year and reached a high of 410 ppm in April 2018 [11]. Prior atmospheric CO_2 concentrations were measured by extracting air from ice in Antarctica and Greenland and it was determined that CO_2 levels were ~278 ppm in 1750 [7].

When considering the change in 200 years, the rate of increase was nominal when compared to that in the past 60 years. Then again, 535-460 million years ago, concentrations were about *20 times* that of current levels. However, it then dropped to levels similar to current concentrations 310-270 million years ago and again increasing to about 6 times current levels about 230 million years ago [12]. These observations indicate nature's ability to regulate CO_2 emissions, even when levels are excessive, through photosynthesis.

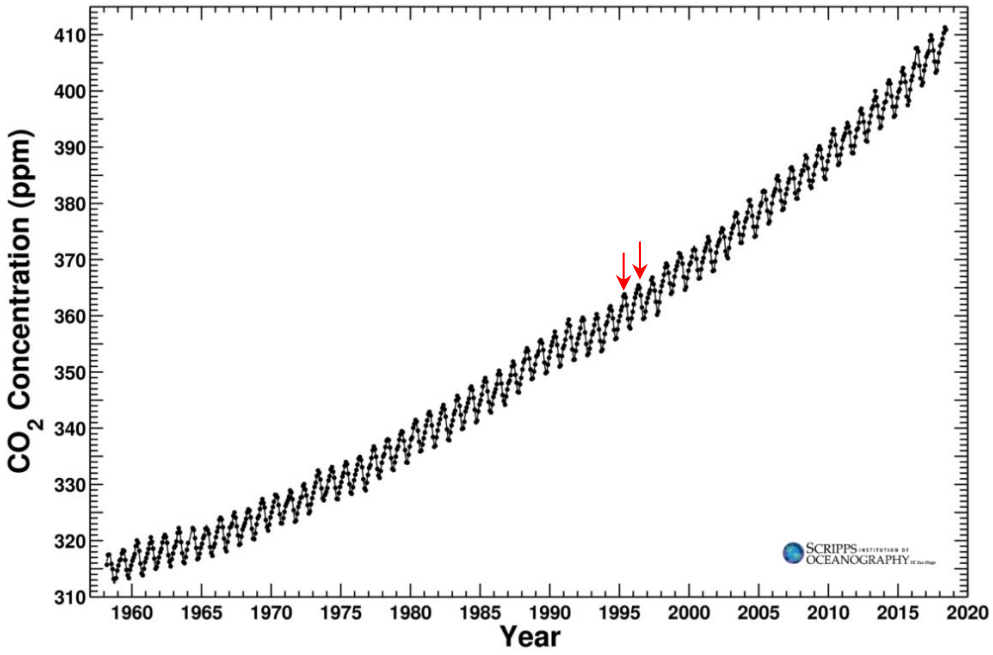

Figure 2.2: The monthly average atmospheric CO_2 concentrations from March 1958 to July 2018, where the distance between the red arrows represents one year. Measurements were taken at the Mauna Loa Observatory, in Hawaii, which sits 19.5362° (2171 km) North of the equator [11].

A majority of the CO_2 emissions occur in the northern hemisphere, due to anthropogenic and naturogenic reasons, and can be seen in Fig. 2.3 and 2.4. The reason nature contributes also is due to a larger percentage of the 'green' vegetation from agriculture and natural sources such as forests are present in the northern hemisphere, which consequently results also in high photosynthesis rates as opposed to the southern hemisphere. These images (Fig. 2.3 and 2.4) were extracted from a video compiled by an ultra-high-resolution computer model (GEOS-5), which assimilated real data to show how and where carbon dioxide traverses the globe. This work was created by scientists at NASA's Goddard Space Flight Centre [13].

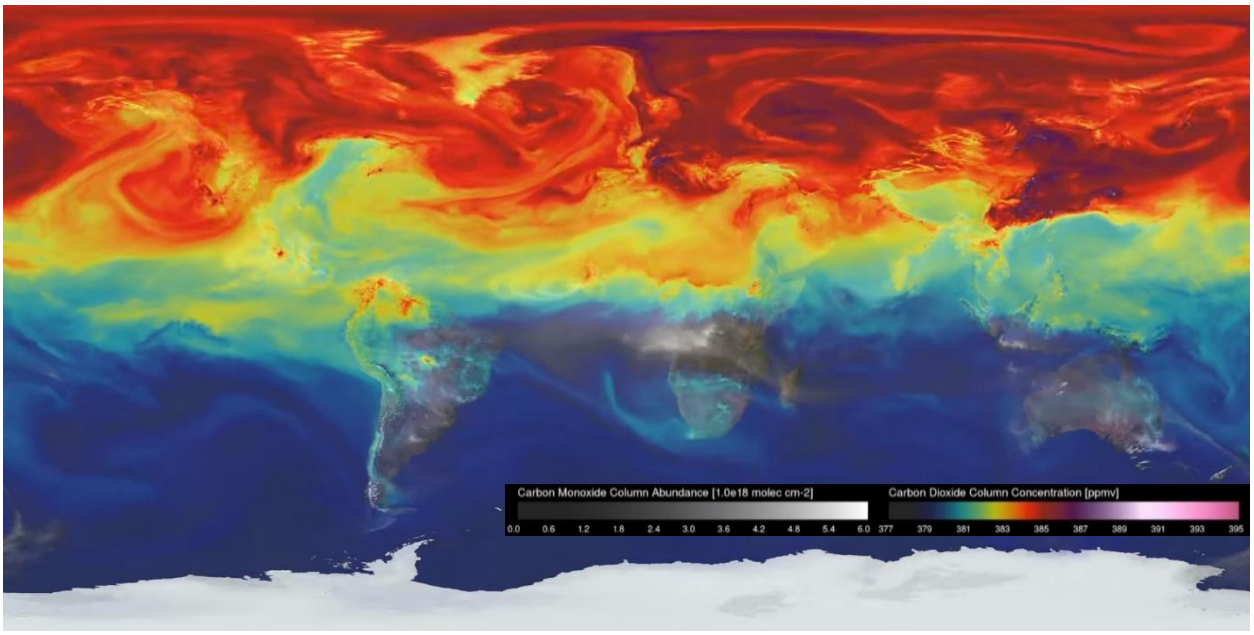

Figure 2.3: The computer-generated image of atmospheric CO_2 concentrations, at a maximum on 29 April 2006, a month after the beginning of spring in the Northern Hemisphere. The colour indicates CO_2 emissions and the white represents carbon monoxide (CO) emissions [13].

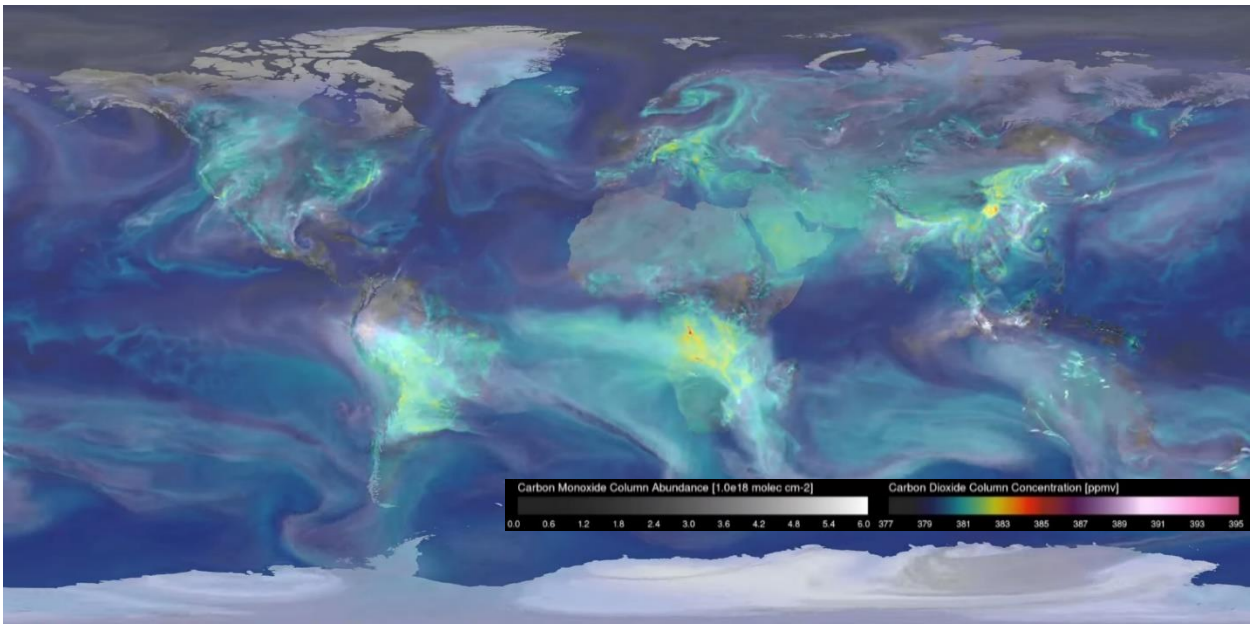

Figure 2.4: The computer-generated image of atmospheric CO_2 concentrations, at a minimum on 29 September 2006, a month before the start of autumn. The colour indicates CO_2 emissions and the white represents carbon monoxide (CO) emissions [13].

The high and low CO_2 concentrations in the NASA images can be seen in the annual trend of CO_2 concentrations taken at MLO (Fig. 2.5), which show a high and low at the same time as Fig. 2.3 and 2.4. These changes are due to the seasons, which effectively regulate photosynthesis. As spring rolls in during March, leaves begin to increase, and the rate of photosynthesis increases until autumn in September. At this point the leaves begin to wither to save energy and results in photorespiration causing a naturogenic increase in CO_2. These fluctuations are notably smaller in the southern hemisphere due to less anthropogenic CO_2 and less vegetation.

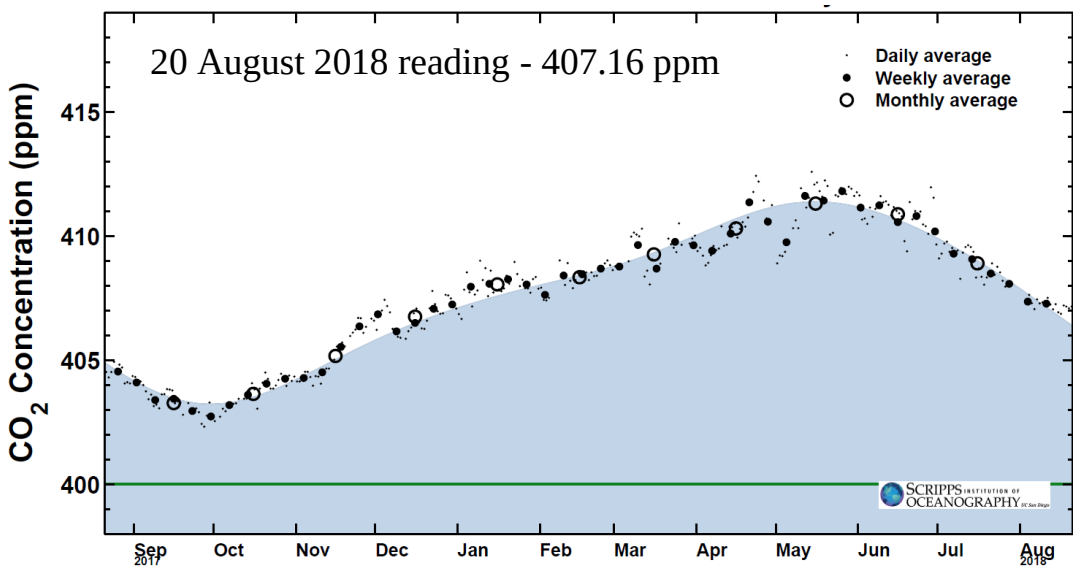

Figure 2.5: The annual CO_2 emission trend between 20 August 2017-2018, noting the minimum at the end of September and the increase during autumn and winter, in the Northern Hemisphere, until the maximum during May [11].

Although one notices where CO_2 emissions end up (air, oceans and plants), there are ramifications other than global warming. A study, done on a crew from the International Space Station, showed that when exposed to a CO_2 concentration of 5000ppm, they experienced sleep disruption, lethargy, emotional irritation, mental slowness and headaches [14]. These concentrations may be excessive but an understanding of the other effects of CO_2, such as the acidification of the ocean, are vital. The decreasing pH of the ocean is caused by the formation of carbonic acid when CO_2 dissolves in the ocean, and causes a challenge for organisms that produce calcium carbonate ($CaCO_3$) shells [7]. However, plants may show a general positive attribute which will be discussed later with elaboration on photosynthesis through biomimetic systems, as seen in the introductory chapter.

Although one may identify three important CO_2 sinks, all of them are natural and not anthropogenic. This does not mean there are not any but rather their contribution is stifled, by the chemistry of CO_2, to be used as a C_1-feedstock to effectively reduce CO_2 emissions (Table 2.1).

Table 2.1: Examples of CO_2 utilization and the consequence of their use [15].

Application	Consequence
Electronic cleaning	CFC substitute
Air-conditioning	CFC and HCFC substitute
Dry cleaning	Halogenated solvent (NH_3) substitute
Carbon Capture and Storage (CCS)	Mitigate contribution to greenhouse effect
Enhanced Oil Recovery (EOR)	Water vapour substitute; CCS (50% remains in well)
Caffeine and fragrances extraction	Organic solvent substitute
Metal cleaning	Metal scrubbing after soldering, cuts and moulding
Dry-ice (solid CO_2)	Cooling agent
Additive to beverages	Effervescence agent (beer, water, wine, etc)
Antibacterial and Fumigant	Antibacterial and Fumigant agent
Food packaging and preservatives	Effective N_2 or other inert gas substitute
Water treatment	pH regulator, alternative to H_2SO_4 (paper industry)
Supercritical CO_2 as reagent/solvent	Manufacturing and modification of polymers
Anti-flame	Oxygen deprivation

Other methods that involve CO_2 conversion into other chemicals include [16]:

- Biological conversion using microalgae in photobioreactor or bio-catalysis.
- Transformation by carbonatation/ mineralization or organic reactions.
- Conversion by electrocatalytic reduction or photocatalysis.
- Chemical transformation using techniques like hydrogenation, dry reforming, etc.

None of the above-mentioned applications are used in a quantifiable manner to effectively reduce CO_2 emissions, such as using it as a reagent or C_1-feestock. This is due to the inert nature of the CO_2 molecule (Fig. 2.6), which is a linear triatomic molecule that is a colourless and odourless gas, with two equivalent yet short carbon-oxygen bonds (1.1602(8) Å) [17]. The molecular geometry, arrangement and electron distribution of CO_2, leads to a nonpolar molecule that produces a molecular quadrupole, which account for most of its chemical and physical properties (Table 2.2) in its different phases (Solid, liquid and gas).

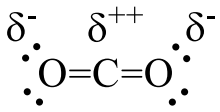

Figure 2.6: The CO_2 Lewis structure with expected charge distribution with respect to Pauling electronegativity differences [17].

It is also clear that nucleophilic attack will occur typically at the carbon atom and electrophilic attack will primarily occur at the oxygen atoms. Also, evidence from ab initio calculations, radio-frequency spectroscopy, microwave and infrared spectroscopy showed that CO_2 acts as a Lewis acid when in the presence of Lewis and Brønsted bases such as amides, amines and water [18]. This is due to a change in the linear structure of CO_2 which results in a change in polarity making it more reactive due to its ability to accept an electron pair from a donor compound.

Although the data in Table 2.2 provides some insight into carbon dioxide's stability as a lone molecule, applications and induced reactivity, natures adept ability to harness CO_2 as a C_1-building block for energy storage is unparalleled. Thus, a biomimetic approach, which is the imitation of systems and models from nature to solve complex human issues, is needed to better facilitate the inclusion of concepts which can contribute to improved methods of reducing the levels of CO_2 in the atmosphere [19].

Table 2.2: Chemical and physical properties of CO_2 (* at 25 °C) [20].

Property	Value and unit
Molecular weight	44.01 g/mol
Solid density	1560 g/L
Heat of formation (ΔH° gas) *	-393.5 kJ/mol
Entropy of formation (S° gas) *	213.6 J/K.mol
Gibbs free energy of formation (ΔG° gas) *	-394.3 kJ/mol
Heat capacity (constant pressure) *	37.1 J/mol.°C
Heat capacity (constant volume) *	28.1 K.mol.°C
Thermal conductivity	14.65 mW
Liquid density at	
0 °C and 1 atm (101.3 kPa)	0.928 g/cm^3
25 °C and 1 atm (101.3 kPa)	0.712 vol/vol
Gas density at	
0 °C and 1 atm (101.3 kPa)	1.976 g/L
Specific volume at	
21 °C and 1 atm (101.3 kPa)	0.546 m^3/kg
Water solubility at	
0 °C and 1 atm (101.3 kPa)	0.3346 g CO_2/100 g H_2O
	1.713 ml CO_2/ml H_2O
25 °C and 1 atm (101.3 kPa)	0.1449 g CO_2/100 g H_2O
	0.759 ml CO_2/ml H_2O
Viscosity at	
0 °C and 1 atm (101.3 kPa)	0.0001372 Poise
25 °C and 1 atm (101.3 kPa)	0.00015 Poise
Sublimation point at	
1 atm (101.3 kPa)	-78.5 °C
Triple point at	
5.1 atm (518 kPa)	-56.5 °C
Triple point pressure	5.1 atm (518 kPa)
Critical values of	
Critical temperature (T_c)	31.04 °C
Critical pressure (P_c)	72.85 atm (7383 kPa)
Critical density (ρ_c)	0.468 g/cm^3
Latent heat of vaporization at	
Triple point (-78.5 °C)	353.4 J/g
0 °C	231.3 J/g

2.4 Biomimetics

The ability to imitate a system or model from nature requires an extensive elucidation to better facilitate its synthetic imitation for a specific human issue. In this scenario, it is to imitate nature's ability to fix CO_2 from the atmosphere and transform it in follow-up steps. Therefore, to achieve this, the following discussion will be separated into three parts: phytochemistry (plant chemistry), organic systems and organometallic systems, respectively. The latter two discuss current and past methods of synthetic models of CO_2 fixation.

2.4.1 Phytochemistry

The majority of CO_2 fixation occurs in plants by means of photosynthesis. These are separated into three groups based on the methodology used to assimilate CO_2, namely the C_3, C_4 and CAM (crassulacean acid metabolism) mechanisms. The latter two mechanisms evolved, from C_3, based primarily on environmental factors such as temperature, water, and atmospheric CO_2 concentration. Before this can be discussed, an understanding of photosynthesis and the C_3 mechanism will however first be elaborated on.

Photosynthesis is essentially the conversion of sunlight into chemically stored energy. This occurs by the absorption of photons (400-700 nm) by photosystem II (PSII) in the chloroplasts and causes a charge separation (electron-hole pairs) which provides the power required to perform redox reactions. The oxygen evolving centre (OEC) is thus activated by the oxidative holes which leads to the oxidation of H_2O to molecular oxygen, which is released into the atmosphere. These electrons progress to PSI (a second photosystem) and eventually produces adenosine triphosphate (ATP) and nicotinamide adenine dinucleotide phosphate hydrogen (NADPH), which are energy enriched bio-reducing agents that are used in the Calvin cycle (Fig. 2.7) [21].

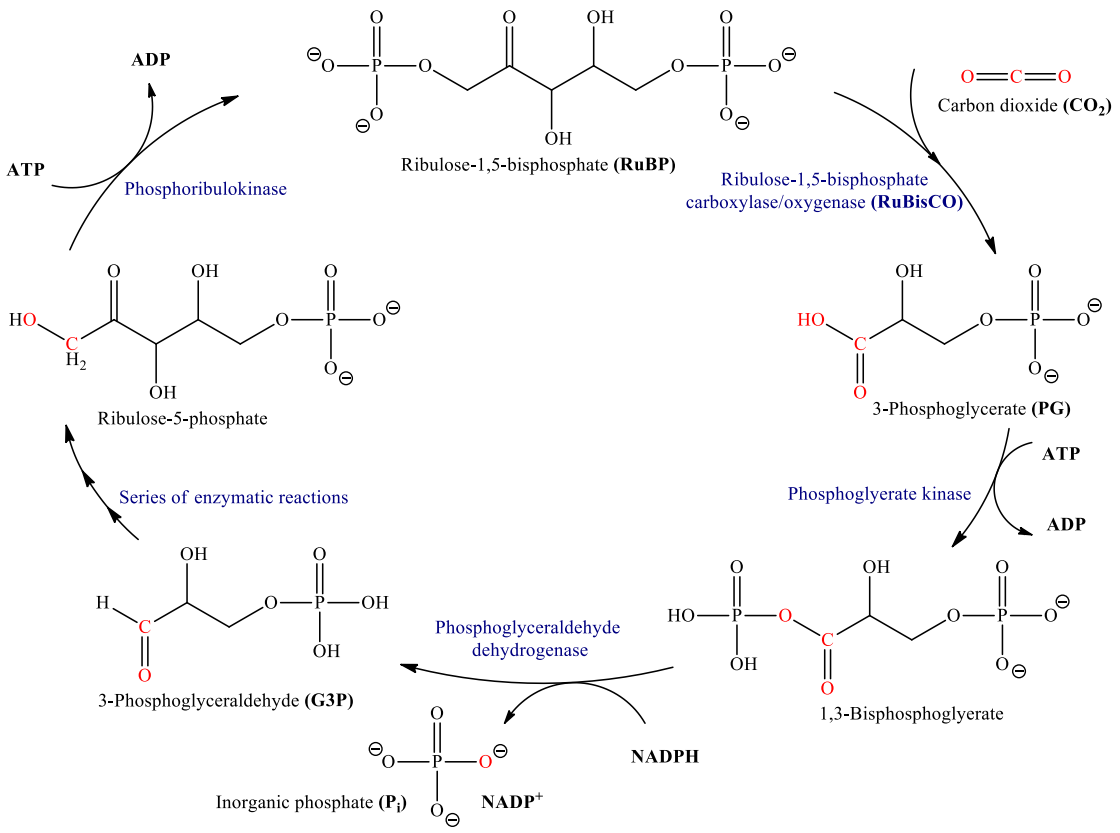

Figure 2.7: The Calvin cycle in plants, where CO_2 is assimilated from the atmosphere into the precursor (3-phosphoglycerate) for glucose production [22,23].

The Calvin cycle is where CO_2 fixation occurs to produce glucose ($C_6H_{12}O_6$) by repeating the cycle six times, and occurs in three stages; CO_2 fixation, reduction and ribulose regeneration. The ribulose-1,5-bisphosphate carboxylase/oxygenase (RuBisCO) enzyme catalyses the reaction between ribulose-1,5-bisphosphate (RuBP) which produces 3-phosphoglycerate (PG). In the next stage, 1,3-bisphosphoglyerate is made by introducing an inorganic phosphate (P_i) to PG from ATP (P_i liberation forms adenosine diphosphate (ADP)) with assistance from phosphoglycerate kinase. This product is then further reduced by phosphoglyceraldehyde dehydrogenase with the assistance of NADPH. During this process, the carbonyl is transferred to the enzyme from the phosphate group with the NADPH eventually donating a hydride, resulting in the release of 3-phosphoglyceraldehyde (G3P), P_i and $NADP^+$. Finally, through a series of enzymatic reactions, G3P ($C_3H_7O_6P$) is converted to ribulose-5-phosphate, which in turn regenerates RuBP, through the donation of a P_i group (PO_4^{3-}) from ATP in the presence of phosphoribulokinase [22].

Since two G3P molecules are required to form a glucose molecule, and RuBP contains 5 carbons, the net sugar formation is 1/6th of a glucose molecule per turn in the cycle, due to the introduction of one CO_2 per RuBP. This is illustrated in the equation (Eq. 2.1) below which shows the sum of the Calvin cycle to produce one G3P molecule

$$3CO_2 + 6NADPH + 5H_2O + 9ATP \rightarrow G3P + 2H^+ + 6NADP^+ + 9ADP + 8P_i \quad \text{(Eq. 2.1)}$$

The cycle is not without flaws, because the fixation of CO_2 is in competition with the concentration of oxygen (O_2) present (which causes photorespiration) due to the relatively high ratio of O_2 to CO_2 in the cell, even though RuBisCO has greater affinity for the latter. This results in oxygenation occurring at the enzyme and reduces the net photosynthetic efficiency by 20-50%, depending on temperature, which ultimately results in the release of CO_2. However, this fact has led to the understanding that CO_2 fixation is not saturated at current levels in C_3 plants and an increase in global emissions may well be moderately controlled by these plants without influencing the nitrogen uptake in the plants, while also stimulating increased photosynthesis and plant growth (based on a survey of 60 experiments) [24]. The only concern is that photosynthesis is highly effective during the summer months, but as noted above, during the winter months photorespiration contributes largely to the CO_2 concentrations in the atmosphere due to a reduced rate of photosynthesis.

As mentioned previously, when CO_2 concentrations were high during the prehistoric era, C_3 plants strived due to the high concentrations. However, when the levels were considerably lower, C_4 plants performed better than C_3 plants, and CAM plants could also but in xeric environments [25]. This is due to the addition of an extra step to the C_3 pathway and some biological evolution.

With respect to C_4, fixation occurs through two types of cells (mesophyll and bundle-sheath) and C_3 only occurs in one (mesophyll). The reason for this extra cell is to first fix CO_2 to pyruvate, by the phosphoenolpyruvate carboxylase (PEPc) enzyme, to form malic acid ($C_4H_6O_5$) or oxalic acid ($C_2H_2O_4$). These acids are then shuttled to the bundle-sheath cell where the CO_2 is removed and is then subsequently fixed by RuBisCO and the C_3 pathway. This additional step results in a higher CO_2 concentration in the cell, which suppresses oxygenation from occurring, and improves the plants ability to photosynthesis at lower CO_2 concentrations. The only requirement is warmer climates due to the need for extra energy for the first fixation process. Consequently, an increase

in CO_2 emissions will not greatly improve C_4 plants ability to fix CO_2 due to the plants ability to already increase the CO_2 concentrations around RuBisCO [12,23,26].

Lastly, the CAM pathway bears a strong resemblance to the previous pathway in that it also increases the CO_2 concentrations around RuBisCO, however, there are two differences. Firstly, the initial fixation occurs at night to minimize water loss due to transpiration. The second is that both fixation processes occur in a single cell (mesophyll), with the fixed CO_2 stored overnight in the large vacuole and released into the cell during the day, with a concentration ranging from 2 to 60-fold of that the atmosphere, for photosynthesis. This also accounts for why many CAM plants have thick succulent leaves, due to the large volume of water required [12]. Paradoxically, CAM plants can also be found in aquatic habitats where atmospheric CO_2 concentrations are low during the day, due other plants and algae being present. The result is that during the night when the plants and algae increase the CO_2 concentrations in the water (due to respiratory processes) the CAM plants fix and store the CO_2, and during the day the CO_2 is released into the cell and fixed during photosynthesis. There also some C_3/CAM intermediate species which can express either pathway, depending on the environmental conditions [27].

Baring all the pathways in mind, evidence has shown that at elevated atmospheric CO_2 concentrations, C_3 plants show the largest biomass increase (+45; 300 species) and C_4 plants the lowest (+12%; 40 species), with CAM plants between them (23%; 6 species). These results are indicative of the CO_2 concentration surrounding the RuBisCO enzyme in the various pathways and the levels of saturation. What is also noteworthy is the ability of some CAM species to fix CO_2 during the day via the C_3 pathway and to increase CO_2 fixation during the night due to PEPc being stimulated at higher concentrations, which results in an improved biomass increase with respect to C_4 plants [28].

Based on the above knowledge, the research towards CO_2 fixation has been through an organic and inorganic approach. Both constitute the same goals of temporarily storing or catalysing the fixation of CO_2, while showing improving results as their respective research continues.

2.4.2 Organic systems

To reduce the amount and cost that some catalysts contribute towards environmental pollution, metal-free, or organic systems have been investigated for CO_2 fixation. One such example is the use of enzymes, though not categorically "metal-free". This involved the extraction of known carboxylating enzymes and introducing them to reactants in the presence of CO_2 (Fig. 2.8). Moreover, it is demonstrated by the phenylphosphate enzymes of *Thauera aromatica* that were partially purified and applied to phenol, under ambient conditions and in the presence of CO_2, to synthesise *p*-hydroxybenzoic acid with high selectivity (ca. 100%) and a TON of ~16 000 [22].

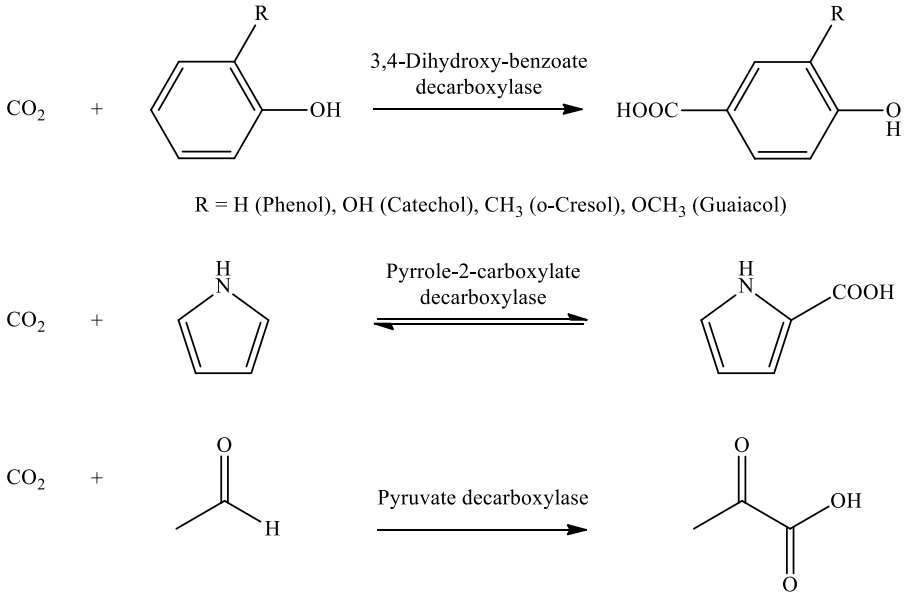

Figure 2.8: Examples of synthetic enzymatic reactions where CO_2 is used as a reagent to introduce a carboxylic functional group in the respective products [22].

Although the enzymatic or bio-catalytic approach to CO_2 fixation is a good example of biomimetics at play, the focus of finding pure organic systems that utilize the electrophilic carbon of CO_2 for fixation was assessed. This ultimately led to two classes of organic bases, namely; amidines and guanidines, that were introduced in Chapter 1 due to their recurring presence in organic and organometallic systems, resulting from their ability to coordinate to CO_2.

The aforementioned bases are termed as “superbases”, but the definition of this term varies. One definition that describes the term “superbase”, without bias, was proposed by Caubère, which stated: *The term ‘superbases should only be applied to bases resulting from a mixing of two (or more) bases leading to new basic species possessing inherent new properties. The term ‘superbase’ does not mean a base is thermodynamically and/or kinetically stronger than another, instead it means that a basic reagent is created by combining the characteristics of several different bases* [29]. The relevance of the definition is seen with the general structures (Fig. 2.9) of the aforementioned superbases and their constituents. Amidines (Fig. 2.9(c)) contain one amine and one imine functional group whereas guanidines (Fig. 2.9(d)) consist of three functional groups (one imine and two amine).

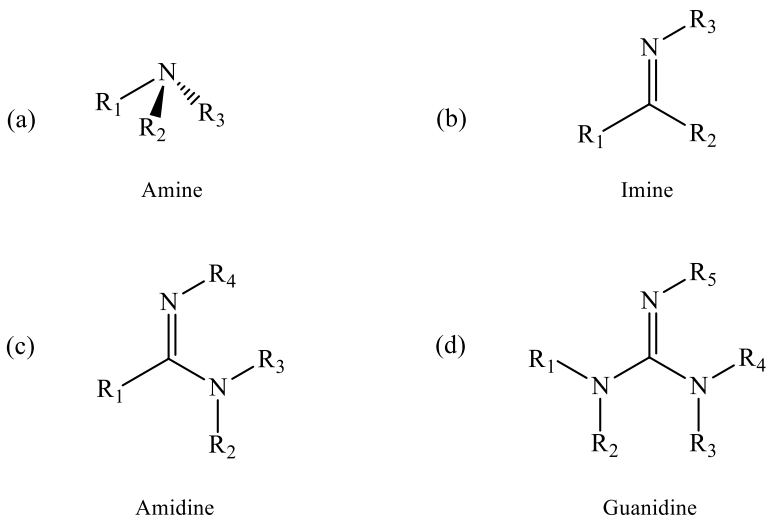

Figure 2.9: The general structure of (a) amines, (b) imines, (c) amidines and (d) guanidines [29].

The result of the additional nitrogen functional groups on the same carbon atom as in Fig. 2.9 (c) and (d) is a proportional increase in basicity. However, the basicity is brought upon by the well-constructed conjugation (resonance) system, of the amine derivatives, following protonation under reversible conditions (Fig. 2.10), which also indicates the reason for the improved basicity of guanidines over the amidines.

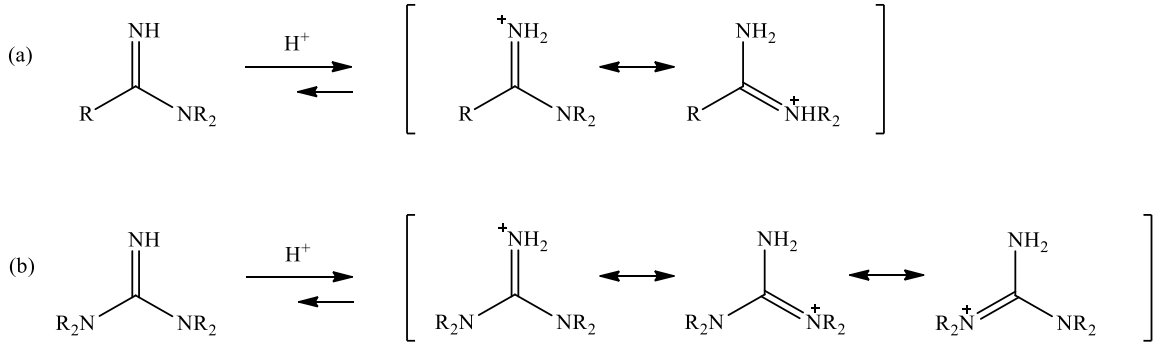

Figure 2.10: The resonance structures of (a) amidinium and (b) guanidinium ions in the presence of an electrophile [29].

These superbases, as a result, contribute to medicinal chemistry because of their high coordination ability, basicity control and nitric oxide source – with examples of them present in medicinal drugs are shown in Fig. 2.11. The amidine based drug, pentamidine (Fig. 2.11(a)), is used for the treatment of protozoan infections while souamidine and pafuramidine (Fig. 2.11(b, c)) are in clinical trials for malaria and African Sleeping sickness. Guanfacine (Fig. 2.11(e)), on the other hand, is used to treat people that suffer from attention deficit hyperactivity disorder (ADHD) and zanamivir (Fig. 2.11(d)) is used as an anti-influenza drug. Lastly, the drugs, cimetidine and famotidine (Fig. 2.11(f, g)) which contain both the amidine and guanidine functional groups are used to treat peptic ulcers and heartburn [30,31].

Although the amidines and guanidines derivatives show medicinal properties, they also have applicability towards CO_2 fixation and catalysis. In particular, the derivatives in question are those mentioned in Chapter 1 (Fig. 1.1), namely 1,8-diazabicyclo[5.4.0]undec-7-ene (DBU), 1,5-diazabicyclo[4.3.0]non-5-ene (DBN), 1,5,7-triazabicyclo[4.4.0]dec-5-ene (TBD), 1,1,3,3-tetramethylguanidine (TMG). The former two amidines (DBU and DBN) are widely accepted to be "non-nucleophilic" bases due to their sterically hindered structures, however, they do show the ability to be nucleophilic. Bertrand *et al*. were the first to explicitly state, in 1993, that DBU and DBN could function as strong nucleophiles [30]. Yet, the case most frequently referred to is the Baylis-Hillman reaction (Fig. 2.12) where a C-C bond forms between a carbon electrophile and an α-β unsaturated carbonyl compound. The original catalyst for this reaction was 1,4-diazabicyclo[2.2.2]octane triethylenediamine (DABCO), but in 1999, Aggarwal *et al*. found that DBU performed better than DABCO, with a faster reaction rate (6 hours and 96 hours respectively) and improved yield (89% and 87% respectively) [30].

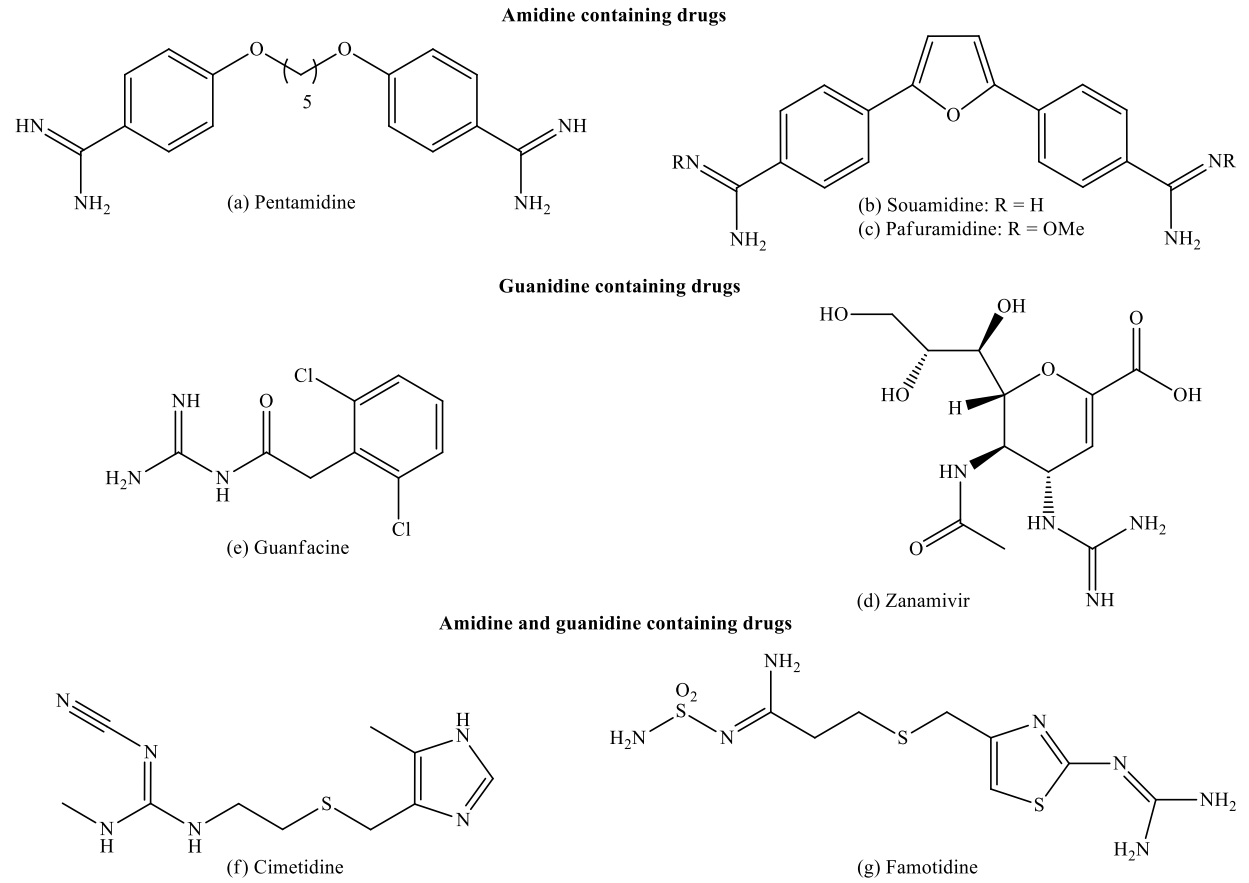

Figure 2.11: The structures of amidine and guanidine containing drugs [30,31].

This led Mayr *et al*., in 2008, to establish the nucleophilicity and Lewis basicity of DBU, DBN, DADCO and 4-dimethylaminopyridine (DMAP) to explain the improved reaction rates seen in the Baylis-Hillman reaction. The results (including those of TBD and TMG), in descending order, for the nucleophilicity was; DABCO > DBN > TBD > DBN > DBU > TMG > DMAP and for the Lewis basicity; TBD > TMG > DBN ~ DBU > DMAP > DABCO [32–35]. While Table 2.3 shows the nucleophilicity and pK_a values for the bases, DBN has a larger Lewis basicity than DBU, even though their pK_a values are similar. This led them to conclude that the reason that DBU is a superior catalyst is because of its higher Lewis basicity, with respect to a Lewis acidic carbon, and a nucleophilicity comparable to DMAP.

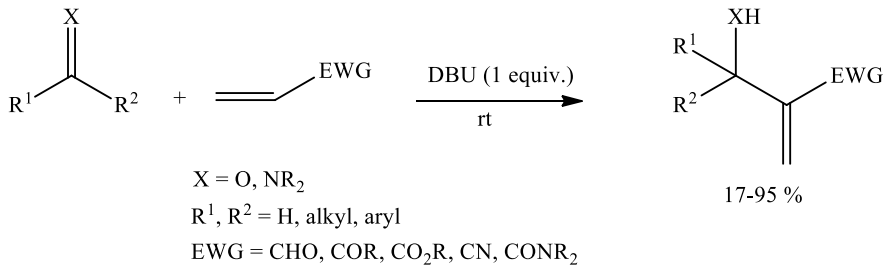

Figure 2.12: The Morita-Baylis-Hillman reaction with DBU to form a C-C bond between a carbon electrophile and an α-β unsaturated carbonyl compound [30].

Table 2.3: The comparison of the pK_a values in aqueous solution and nucleophile specific reactivity parameters (N) in acetonitrile [32,34–36].

Base	p*K*a	Nucleophilicity (N)
DBU	13.5	15.3
DBN	13.5	16.3
DMAP	9.2	15.0
TMG	13	13.6[a]
TBD	15.2	16.2[a]
DABCO	8.6	18.8

[a] Nucleophilicity parameter in dichloromethane from ref. [36].

This also accounts for the varied catalytic applications of the amidines and guanidines on electrophilic carbons, most notably, CO_2 [30]. These include the formation of oxazolidinones and quinazolines in the presence of CO_2 and their respective starting materials, where the bases were the catalyst [37].

In 2004 Pérez *et al*. sought to confirm the existence of an intermediate adduct formed between the bases (specifically amidines) and CO_2, which other authors had claimed promoted its catalytic ability. Though they claimed that the presence of a zwitterionic complex had formed, through ^{13}C NMR, attempts to crystallise the adduct only resulted in the formation of the bisamidinium bicarbonate salts [38]. They further claimed that elemental and thermogravimetric analysis suggested that the zwitterionic adduct is probably associated with a molecule of water (Fig. 2.13). However, less than a year later, Jessop *et al*. refuted the claim of a zwitterionic adduct forming [39]. They conducted a similar experiment which contained adventitious water (as was the case with the former experiment) and another where all reagents and solvents were thoroughly dried. The results (Fig. 2.13) denied the formation of the zwitterion in adventitious water, only the bicarbonate, where as in the strictly anhydrous conditions, no product formed.

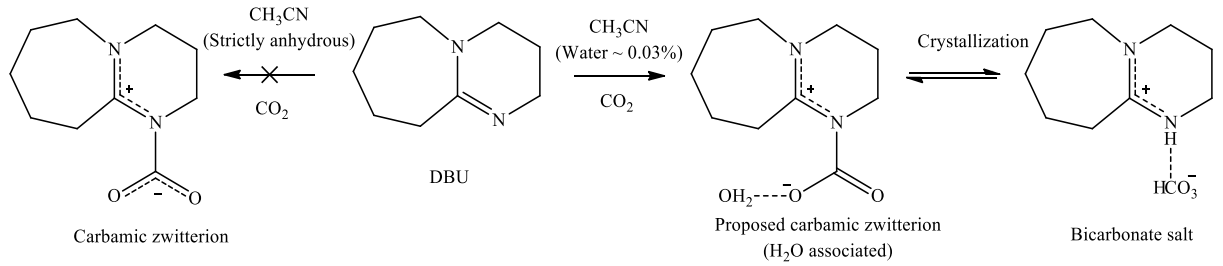

Figure 2.13: The dry and wet reaction of DBU with CO_2, where no product forms in the dry reaction and the bicarbonate salt forms in the wet reaction. Indicating that no zwitterionic product forms.

Thus Jessop *et al*. concluded that, although theoretically possible, no unambiguous evidence supports the zwitterion existence yet and proposed that fixation was likely promoted, in organic solvents, by the stabilizing and solubilizing ability of DBU on the bicarbonate anion. A similar process, once again, followed in 2008 by Pereira *et al*., with respect to the guanidines. They noted that these bases also captured CO_2 and formed bicarbonates, likely through a water-solvated carbamic intermediate, and that the resulting compound could react with nucleophilic amines by transcarboxylation. This suggested biomimetic activity similar to the non-metal carbonic anhydrase and transcarboxylase enzymes.

Based on the prior three articles, Villiers *et al*. successfully isolated the zwitterionic adduct of TBD-CO_2 under strict anhydrous conditions (Fig. 2.14), which showed to have an almost planar structure [40]. The zwitterionic nature, of the adduct, was demonstrated through the delocalised cationic system of the guanidine functional group, with an average C-N distance of 1.346(16) Å, and the anionic carboxylate-type CO_2, with a mean C-O distance of 1.243(14) Å. The bond length of the hydrogen with the nitrogen (N-H 0.95 Å) is shorter than it is with the oxygen (O···H 1.70 Å), which also supports the formation of a zwitterion. Both the charge delocalization and the hydrogen bonding to the carboxylate oxygen assist in stabilising the adduct. The distance (1.480(3) Å) between the N-CO_2 bond was also recorded to be longer than the typical value for other carbamates (1.35 Å). Unsurprisingly, the adduct is sensitive to hydrolysis, leading to the formation of the bisguanidinium bicarbonate salts.

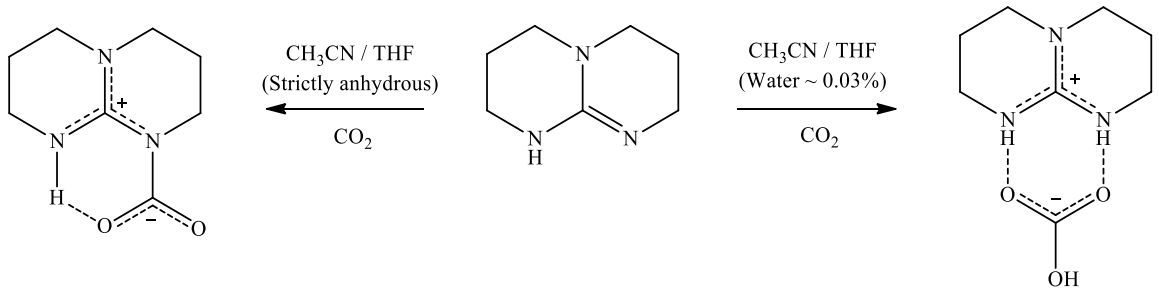

Figure 2.14: The dry and wet reactions of TBD with CO_2, where the zwitterionic product was isolated in the dry conditions and the bicarbonate in the wet conditions [40].

These properties of the amidines and guanidines led to their subsequent use in carbon dioxide-binding organic liquids (CO_2BOLs) or switchable ionic liquids (SWILs) for CO_2 capturing (Fig. 2.15) [41]. These systems consist of a liquid mixture of a base and an alcohol (both neutral), which goes through reversible complexation with CO_2 and results in a highly ionic liquid. The process results in the formation of an amidinium or guanidinium alkyl carbonate salt which forms when the CO_2 inserts into the O-H bond, with the hydrogen protonating the base. The SWILs can contain 1:1 mol % ratio (15 wt %) of chemically fixed CO_2 at STP (Standard temperature and pressure) and even more so under pressure. The process occurs at low or moderate pressures and is reversible under mild conditions (e.g. purge using nitrogen or argon gas, under vacuum or mild heating) with minimal substrate loss [42,43].

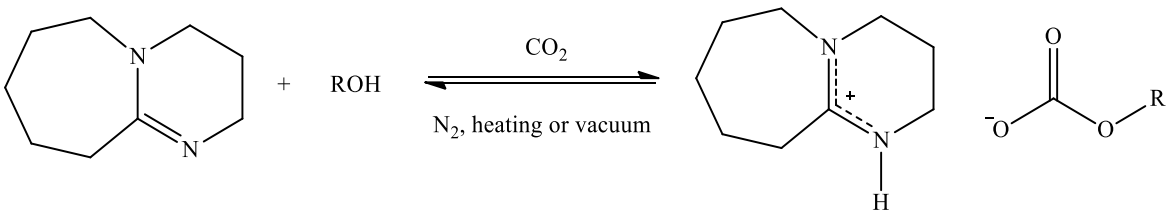

Figure 2.15: The SWIL system, constituting of a base (DBU) and an alcohol, stores CO_2 with minimal energy input required to release CO_2 from the system [42].

Although SWILs highlight the ability to temporarily capture CO_2 with minimal energy input, a recent article described the capture of CO_2 from ambient air using a guanidine sorbent [44]. The ligand, 2,6-pyridine-bis(iminoguanidine) (PyBIG), was left in an aqueous solution for a few days in ambient air which resulted in the formation of crystals ($PyBIGH_2(CO_3)(H_2O)_4$) which indicated the presence of carbonate in the crystal structure (Fig. 2.16). To preliminary quantify the yield

through crystallization of the product, the reaction was performed for two days in ambient air and resulted in an average yield of 50.3(4) %, without optimisation. Through heating (Between 80-120 °C), the release of CO_2 and H_2O were noted with quantitative regeneration of PyBIG ligand. The efficacy to capture atmospheric CO_2 was thus attributed to the presence of the electron-withdrawing pyridine enhancing the Lewis basicity of the guanidines groups to become protonated in alkaline carbonate/bicarbonate solutions (pH 8.5-10.5), along with the very low aqueous solubility of the CO_2 containing crystal complex, which enhanced the bis-guanidinium carbonate salt to crystallize. This approach provides another way for CO_2 capture and is energy sustainable.

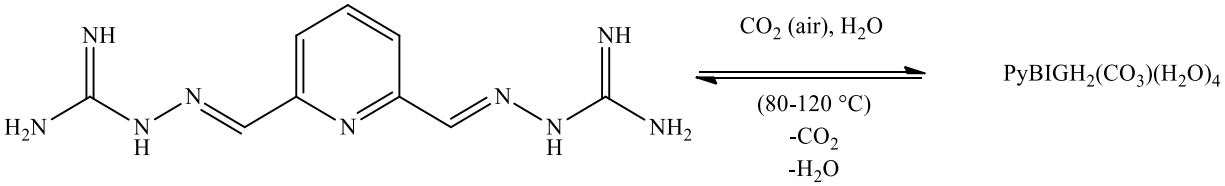

Figure 2.16: The reaction of PyBIG in aqueous solution, while exposed to ambient air, absorbs CO_2 from the atmosphere and is released through heating [44].

The organic systems discussed, with specific focus on the superbases, have shown inherent properties that has propagated its use in catalysis and carbon capture and sequestration (CCS) technology. However, they additionally have application in inorganic systems by being incorporated as ligands, cocatalysts or in conjunction with SWILs.

2.4.3 Organometallic systems

The contribution that metal containing complexes have on catalysis far exceeds organic catalysts, primarily due to their superior stability, recoverability and catalytic abilities as well as their economic viability and absent/ lack of by-product formation. Considering that none of the amidines or guanidines showed CO_2 fixation into high yielding products as yet, the catalysts that contain and lack the presence of the superbases will be evaluated with respect to CO_2 assimilation. Additionally, the superbases containing catalytical reactions will incorporate CO_2-absent reactions to discern the role or effect that the superbases contribute.

Systems that incorporate the superbases are used as an additive to promote the reactions, ligands on the catalyst or in conjunction with other systems. For example, the formation of acrylic acid derivatives from-1,3-butadiene, allene and acetylene are catalysed by $Ni(COD)_2$, where DBU is used to promote the reaction, presumably through carbamate/bicarbonate formation, is an illustration of its promoting ability [45].

This is further exemplified by hydrogenation of $scCO_2$ by $[RuCl(OAc)(PMe_3)_4]$ as the catalyst (Fig. 2.18(a)) with the addition of a base and a protic solvent as a cocatalyst, by Munshi *et al*. [46]. Through evaluating the different effects i.e. of the bases and alcohols, a TOF of 95 000 h^{-1} was achieved using triethylamine (NEt_3) and pentafluorophenol (C_6F_5OH) as cocatalysts. However, this was the highest recordable result because of equipment limitations. Using the catalyst and methanol for hydrogenation, the organic bases with intermediate basicity (pK_a between 8-12) gave the best results, with the stronger bases' poor solubility suggested as the reason for their lacklustre performance. Of the intermediate bases, DBU gave the best reaction rate, while being 8 times faster than the second-best base TMEDA (*N,N,N',N'*-tetramethylethylenediamine) and 10 times more than NEt_3. The effect of the alcohol showed that the pK_a must be lower than that of the protonated amine, with pentafluorophenol (C_6F_5OH) giving the best results. With C_6F_5OH as the protic solvent, the formic acid yields (formic acid mol/ base mol) after an hour for NEt_3 and DBU were 0.66 and 1.36, respectively, and 1.54 and 1.60 after 10 hours. Due to the maximum theoretical yield being 1, the yield after one hour should give an indication of the base promotion ability and not the eventual yield. Therefore, the TOF value using C_6F_5OH and DBU may well exceed that of NEt_3, however, the comparison of other amidines and guanidines were not assessed in this study.

Zhang *et al*. also made use of a superbase (TMG) as a cocatalyst for Heck reactions using aryl halides and terminal olefins (Fig. 2.17) [47]. Their results indicated that TONs of up to a million could be achieved in the reaction of butyl acrylate and iodobenzene, claiming that TMG may act as a ligand, stabilizing the Pd(0) species in the reaction.

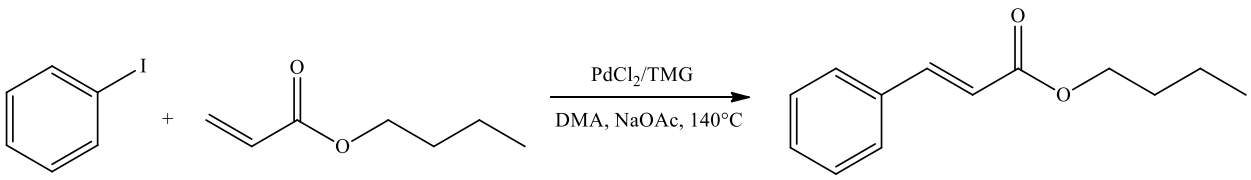

Figure 2.17: The Heck reaction between butyl acrylate and iodobenzene, where TMG acts as a co-catalyst [47].

The superbases, in SWILs, have also been incorporated with catalysts to determine their use as CO_2 capture and reduction systems. This is assumed to be due to solvent stabilization promoting CO_2 hydrogenation by stabilising the formic salts and acids, based on the polarity of the solvent. The stabilizing ability followed the decreasing trend of; ethers, alcohols > water > ionic liquids (SWIL) [48]. One system was able to achieve a TON of 5100 at a substrate-to-catalyst loading of 8650, using $RuCl_2(PPh_3)_3$ as the catalyst. However, DBU was hydrolysed into a cyclic lactam, by water that was released during esterification – similar to the hydrolysed DBN lactam. This was found to be from water produced by the catalyst during the reaction, with drying agents failing to prevent the DBU hydrolysis [48].

Another example was noted wherein *cis*-$[Ru(PNP)_2(H)_2]$ (PNP = $CH_3N[CH_2P(CH_2CH_3)_2]$) was used as the catalyst, and the SWIL consisted of DBU and 1-hexanol. The results suggested that the rate of reduction of CO_2 by the catalyst appeared slower than the carbonate reduction, probably due to a different mechanism or low CO_2 solubility, relative to the SWIL. This was eventually corroborated by basic thermodynamic calculations. The authors also hypothesized that an inner-sphere mechanism took place where direct insertion of an anionic alkylcarbonate into the complex's metal hydride bond [49].

The use of a biphasic medium (H_2O/Me-THF) with a base and Ru-MACHO^{TM}-BH as the catalyst (Fig. 2.18(b)) was evaluated by Prakash *et al*. [50]. The results showed that DBU, DABCO and TMG gave the best results, however, DBU was not further evaluated due to hydrolysis. Through optimization (17 mmol base in 6ml water, 2μmol catalyst, 10 ml dioxane with 2ml additional water), TMG and DABCO gave TON values of 7375 and 6500, respectively.

(a)

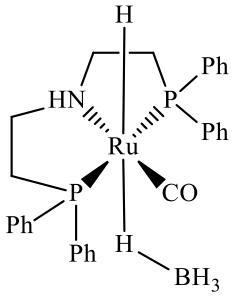

Ru-MACHO^{TM}-BH

(b)

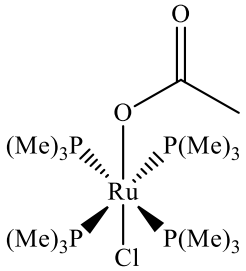

$RuCl(OAc)(PMe_3)_4$

Figure 2.18: The catalysts used in conjunction with a superbase which produced high TON values [46,50].

Although the examples reported above illustrate the promoting ability of the superbases, their use as ligands on metal centres also show promise in CO_2-free reactions. One such case is the selective double carbonylation of aryl iodides (Fig. 2.19), where the catalyst *trans*-[$Pd(DBU)_2Cl_2$] gave 91% conversion and 90% selectivity (Fig. 2.19(a)) [51]. The authors stated that DBU is vital in that it performed as a base, nucleophile (acyl transfer agent) and ligand.

Finally, the catalyst [Rh(L)(COD)Cl], (L = (DBU, DBN)), was patented in 2012 for the hydrogenation of double bonds, notably between C=N or C=C double bonds, although the C=O double bonds are also mentioned to a lesser extent. The peak TON mentioned was for the reaction between stearic acid and oleic acid, with a value of 329 TON and 89 % conversion [52]. The crystal structures (Fig 2.20) for the catalysts showed that the substitution of DBU (Fig. 2.20(a)) *vs.* DBN (Fig. 2.20(b)) left the Rhodium-ligand bond length nearly unchanged, with DBU having a slightly shorter bond length than DBN. Additionally, the deviation from planarity was larger in the DBU substituted complex than that of the DBN complex [53]. Further comparisons can be made on the structures of the complexes by comparing the cyclooctadiene (COD) ligand and evaluating its conformity with respect to the amidine ligands, as was done by Hill *et al*. on COD-containing complexes [54]. Although examples exist of the uses of superbases in CO_2 fixation, especially with DBU, there are also examples of fixation occurring in their absence.

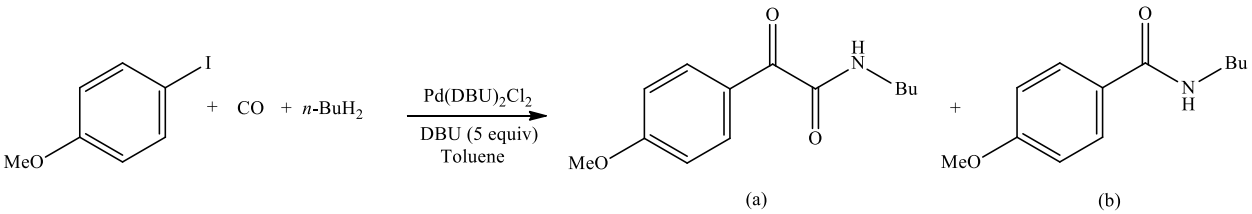

Figure 2.19: The selective double carbonylation where DBU is used as a ligand/ cocatalyst [51].

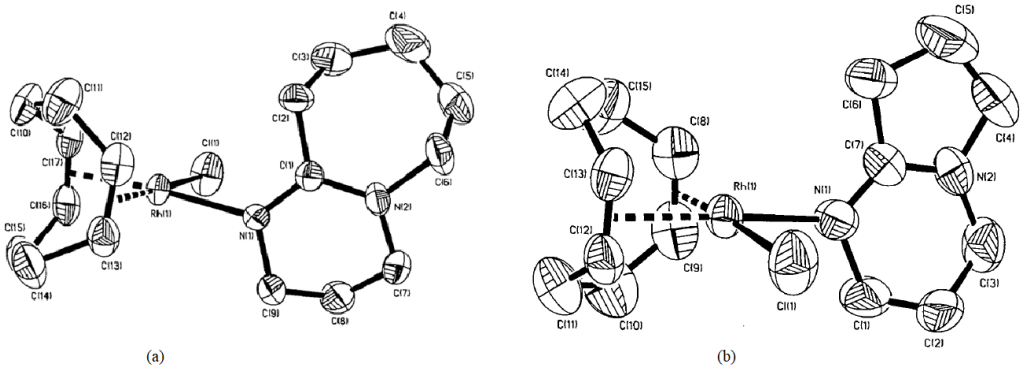

Figure 2.20: The crystal complexes of (a) [Rh(COD)(DBU)Cl] and (b) [Rh(COD)(DBN)Cl] [53].

Studies have been done on electrochemical reduction of CO_2, but more biomimetically appropriate reactions involve photocatalytic conversion of CO_2. Three such catalysts are illustrated in Fig. 2.21 and are briefly discussed below. The catalyst shown in Fig. 2.21(a), [Re(Mebpy)$(CO)_3$Cl]-BODIPY, reduced CO_2 to CO, achieving a TON of ~ 20 when irradiated with light ($\lambda_{ex} \geq 400$ nm) of approximately 5 hr^{-1} [55]. Similarly, benzaldehyde was produced between benzene and CO_2, using Fig. 2.21(b), as the catalyst, upon UV irradiation [56]. This was achieved by metal-ligand cooperation (MLC)-based CO_2 splitting, which may provide an alternative to using carbon monoxide. The reaction is not fully catalytic because each step requires different conditions, but the authors aim to transform the reaction into a catalytic cycle. Finally, CO_2 reduction to formate in a biphasic liquid-condensed gas system, using a catalyst $[Ru(bpy)_2(CO)H]^+$ and photosensitizer [Tris(2,2′-bipyridyl)dicarbonylruthenium(0)] (Fig. 2.21(c)), yielded a TON in excess of a 1000 [57].

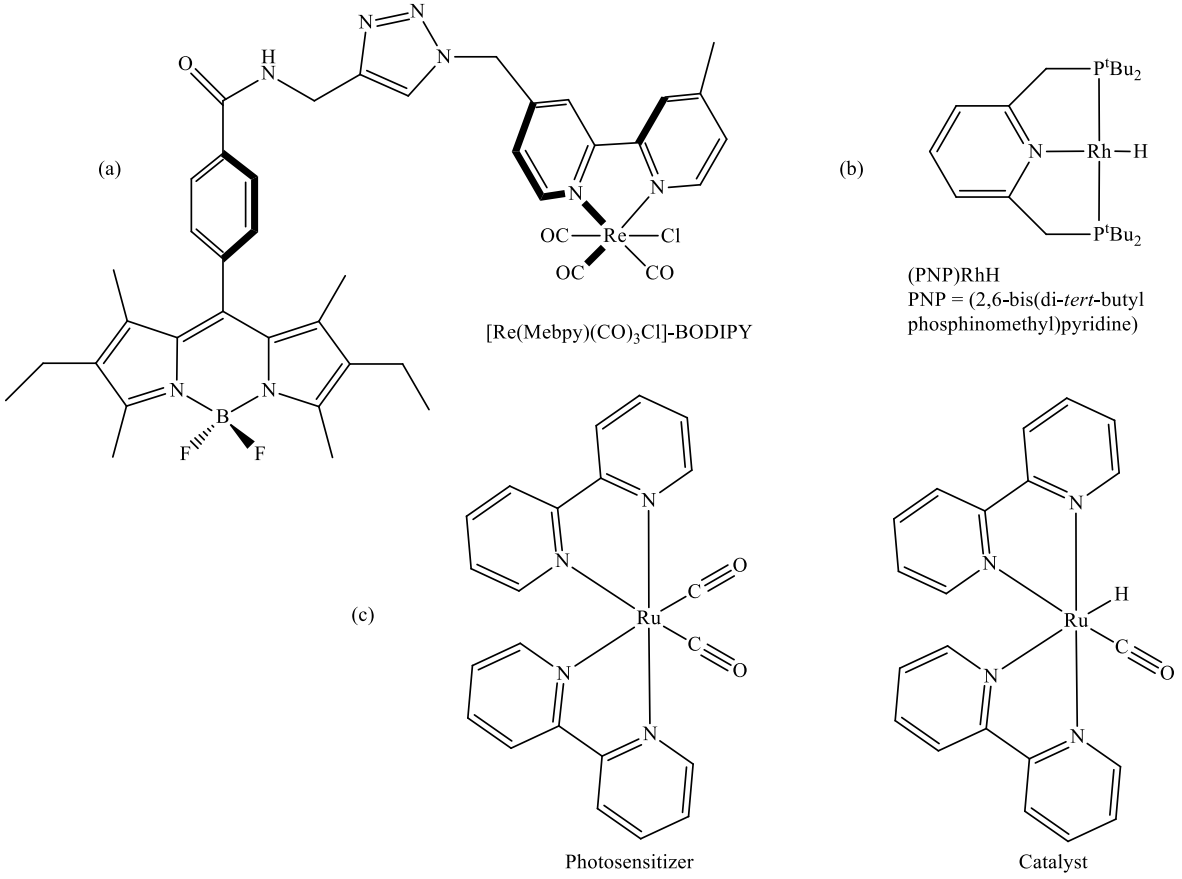

Figure 2.21: Three photocatalysts that can reduce carbon dioxide. (a) [Re(Mebpy)$(CO)_3$Cl]-BODIPY, (b) [(PNP)RhH] and (c) $[Ru(bpy)_2(CO)H]^+$ and photosensitizer [Tris(2,2′-bipyridyl)dicarbonylruthenium(0)] [55–57].

2.5 Conclusion

Different approaches and a variation of applicable systems have been briefly described in this chapter, which also highlighted relevant background on carbon dioxide fixation/ utilisation processes.

Through comparison of the systems that contain and lack the presence of a superbase, current evidence suggests that the former holds promise for CO_2 fixation. While these bases seem to play a pivotal role, their mechanistic involvement has not been fully elucidated, especially in the scenarios where they are used as ligands on metal complexes. By means of synthesis of known complexes, containing the superbases, and attempting to replicate their synthesis with the superbases that have not been characterized, new model catalysts may be found. Based also on the known complexes, kinetic studies using neutral ligands may illustrate the mechanistic and kinetic pathways that CO_2 may proceed to be activated by.

This will be further addressed in the proceeding chapters, commencing with the basic theory of the characterization methods, synthesis methods and their characterization, followed by reactivity studies on selected systems.

2.6 References

[1] C. Streck, P. Keenlyside, & M. von Unger Atlas, "The Paris Agreement: A New Beginning", *J. Eur. Environ. Plan. Law*, **13,** 1–27 (2016).

[2] G. Boeing, "A Visual Introduction to Nonlinear Systems: Chaos, Fractals, and the Limits of Prediction", *Systems*, **4,** 1–18 (2016).

[3] European Environment Agency, "Particulate matter from natural sources and related reporting under the EU Air Quality Directive in 2008 and 2009", *EEA Technical report* (2012)

[4] O. Raaschou-Nielsen *et al.*, "Air pollution and lung cancer incidence in 17 European cohorts: prospective analyses from the European Study of Cohorts for Air Pollution Effects (ESCAPE)", *Lancet Oncol.*, **14,** 813–822 (2013).

[5] A. Nahrstedt, & C. Weber, "Outdoor Particulate Matter Exposure and Lung Cancer: A Systematic Review and Meta-Analysis", *Dtsch. Apotheker Zeitung*, **145,** 62–64 (2005).

[6] J. Lin *et al.*, "Global climate forcing of aerosols embodied in international trade", *Nat. Geosci.*, **9,** 790–794 (2016).

[7] G. Hartfield, J. Blunden, & D. S. Arndt, "State of the Climate in 2017", *Bull. Am. Meteorol. Soc.*, **99,** 1–270 (2018).

[8] S. Field, "The effect of temperature on crime", *Br. J. Criminol.*, **32,** 340–351 (1992).

[9] M. Burke, F. González, P. Baylis, S. Heft-Neal, C. Baysan, S. Basu, & S. Hsiang, "Higher temperatures increase suicide rates in the United States and Mexico", *Nat. Clim. Chang.*, **8,** 723–729 (2018).

[10] T. A. Boden, G. Marland, & R. J. Andres, "Global, Regional, and National Fossil-Fuel CO2 Emissions. Carbon Dioxide Information Analysis Center, Oak Ridge National Laboratory, U.S. Department of Energy, Oak Ridge, Tenn., U.S.A.", (2017). Available at: http://cdiac.ess-dive.lbl.gov/trends/emis/tre_glob_2014.html. (Accessed: 21st August 2018)

[11] R. A. Berner, "A History of Atmospheric CO2 and Its Effects on Plants, Animals, and Ecosystems", **177,** *Springer New York*, (2005)

[12] U. Lüttge, "Plant Physiology", *Encyclopedia of Ecology Elsevier*, (2019)

[13] W. Putman, K. Sharghi, A. . Lepsch, & P. Lynch, "A Year In The Life Of Earth's CO2", (2014). Available at: http://svs.gsfc.nasa.gov/11719. (Accessed: 22nd August 2018)

[14] D. Law J., Watkins S., Alexander, & W. S. Law J., "In-Flight Carbon Dioxide Exposures and Related Symptoms: Associations, Susceptibility and Operational Implications", *NASA Tech. Rep.*, 1–21 (2010).

[15] M. Aresta, A. Dibenedetto, & A. Dutta, "Energy issues in the utilization of CO2 in the synthesis of chemicals: The case of the direct carboxylation of alcohols to dialkyl-carbonates", *Catal. Today*, **281,** 345–351 (2017).

[16] W. Zhang, Y. Hu, L. Ma, G. Zhu, Y. Wang, X. Xue, R. Chen, S. Yang, & Z. Jin, "Progress

and Perspective of Electrocatalytic CO2 Reduction for Renewable Carbonaceous Fuels and Chemicals", *Adv. Sci.*, **5,** 1–24 (2018).

[17] L. J. Murphy, K. N. Robertson, R. A. Kemp, H. M. Tuononen, & J. A. C. Clyburne, "Structurally simple complexes of CO2", *Chem. Commun.*, **51,** 3942–3956 (2015).

[18] J. C. Meredith, K. P. Johnston, J. M. Seminario, S. G. Kazarian, & C. a Eckert, "Quantitative Equilibrium Constants between CO 2 and Lewis Bases from FTIR Spectroscopy", *J. Phys. Chem.*, **100,** 10837–10848 (1996).

[19] J. F. V. Vincent, O. A. Bogatyreva, N. R. Bogatyrev, A. Bowyer, & A. K. Pahl, "Biomimetics: Its practice and theory", *J. R. Soc. Interface*, **3,** 471–482 (2006).

[20] C. Song, "Global challenges and strategies for control, conversion and utilization of CO2 for sustainable development involving energy, catalysis, adsorption and chemical processing", *Catal. Today*, **115,** 2–32 (2006).

[21] S. Berardi, S. Drouet, L. Francàs, C. Gimbert-Suriñach, M. Guttentag, C. Richmond, T. Stoll, & A. Llobet, "Molecular artificial photosynthesis", *Chem. Soc. Rev.*, **43,** 7501–7519 (2014).

[22] J. Shi, Y. Jiang, Z. Jiang, X. Wang, X. Wang, S. Zhang, P. Han, & C. Yang, "Enzymatic conversion of carbon dioxide", *Chem. Soc. Rev.*, **44,** 5981–6000 (2015).

[23] A. Bar-Even, E. Noor, N. E. Lewis, & R. Milo, "Design and analysis of synthetic carbon fixation pathways", *Proc. Natl. Acad. Sci.*, **107,** 8889–8894 (2010).

[24] B. G. Drake, M. A. Gonzàlez-Meler, & S. P. Long, "More efficient plants: a consequence ofrRising atmospheric CO2 ?", *Annu. Rev. Plant Physiol. Plant Mol. Biol.*, **48,** 609–639 (1997).

[25] P. Hunter, "The impact of CO2", *Eur. Mol. Biol. Organ.*, 2–4 (2007).

[26] M. D. Hatch, A. Agostino, & J. N. Burnell, "Photosynthesis in phosphoenolpyruvate carboxykinase-type C4 plants: Activity and role of mitochondria in bundle sheath cells", *Arch. Biochem. Biophys.*, **261,** 357–367 (1988).

[27] J. C. Hull, H. S. Neufeld, & F. S. Gilliam, "Plant Ecology", *Encyclopedia of Ecology Elsevier*, (2019)

[28] H. Poorter, & M.-L. Navas, "Plant growth and competition at elevated CO2: on winners, losers and functional groups", *New Phytol.*, **157,** 175–198 (2003).

[29] T. Ishikawa, "Superbases for Organic Synthesis", *John Wiley & Sons, Ltd*, (2009)

[30] J. E. Taylor, S. D. Bull, & J. M. J. Williams, "Amidines, isothioureas, and guanidines as nucleophilic catalysts", *Chem. Soc. Rev.*, **41,** 2109–2114 (2012).

[31] J. W. Shaw, D. H. Grayson, & I. Rozas, "Synthesis of Guanidines and Some of Their Biological Applications", *in Topics in Heterocyclic Chemistry* **50,** 1–51 (2015)

[32] E. A. Castro, P. R. Campodónico, R. Contreras, P. Fuentealba, J. G. Santos, J. R. Leis, L. García-Río, J. A. Saez, & L. R. Domingo, "Experimental and theoretical study on the substitution reactions of aryl 2,4-dinitrophenyl carbonates with quinuclidines", *Tetrahedron*, **62,** 2555–2562 (2006).

[33] A. O. Konuray, F. Liendo, X. Fernández-Francos, À. Serra, M. Sangermano, & X. Ramis, "Sequential curing of thiol-acetoacetate-acrylate thermosets by latent Michael addition reactions", *Polymer (Guildf).*, **113,** 193–199 (2017).

[34] M. Baidya, & H. Mayr, "Nucleophilicities and carbon basicities of DBU and DBN", *Chem. Commun.*, 1792–1794 (2008).

[35] K. Kaupmees, A. Trummal, & I. Leito, "Basicities of Strong Bases in Water: A Computational Study", *Croat. Chem. Acta*, **87,** 385–395 (2014).

[36] B. Maji, "Reactivity Parameters for Understanding Nucleophilic Organocatalysis", *Phd Thesis Ludwig Maximilian University of Munich*, (2012)

[37] T. Sakakura, J. Choi, & H. Yasuda, "Transformation of Carbon Dioxide", *Chem. Rev.*, **107,** 2365–2387 (2007).

[38] E. R. Pérez, R. H. A. Santos, M. T. P. Gambardella, L. G. M. De Macedo, U. P. Rodrigues-Filho, J. C. Launay, & D. W. Franco, "Activation of carbon dioxide by bicyclic amidines", *J. Org. Chem.*, **69,** 8005–8011 (2004).

[39] D. J. Heldebrant, P. G. Jessop, C. A. Thomas, C. A. Eckert, & C. L. Liotta, "The Reaction of 1,8-Diazabicyclo[5.4.0]undec-7-ene (DBU) with Carbon Dioxide", *J. Org. Chem.*, **70,** 5335–5338 (2005).

[40] C. Villiers, J. P. Dognon, R. Pollet, P. Thuéry, & M. Ephritikhine, "An isolated CO2 adduct of a nitrogen base: Crystal and electronic structures", *Angew. Chemie - Int. Ed.*, **49,** 3465–3468 (2010).

[41] M. Ç. Öztürk, C. S. Ume, & E. Alper, "Reaction Mechanism and Kinetics of 1,8-Diazabicyclo[5.4.0]undec-7-ene and Carbon Dioxide in Alkanol Solutions", *Chem. Eng. Technol.*, **35,** 2093–2098 (2012).

[42] J. Yao, D. B. Lao, X. Sui, Y. Zhou, S. K. Nune, X. Ma, T. P. Troy, M. Ahmed, Z. Zhu, D. J. Heldebrant, & X.-Y. Yu, "Two coexisting liquid phases in switchable ionic liquids", *Phys. Chem. Chem. Phys.*, **19,** 22627–22632 (2017).

[43] D. B. Lao, B. R. Galan, J. C. Linehan, & D. J. Heldebrant, "The steps of activating a prospective CO2 hydrogenation catalyst with combined CO2 capture and reduction", *Green Chem.*, **18,** 4871–4874 (2016).

[44] C. A. Seipp, N. J. Williams, M. K. Kidder, & R. Custelcean, "CO2 Capture from Ambient Air by Crystallization with a Guanidine Sorbent", *Angew. Chemie Int. Ed.*, **56,** 1042–1045 (2017).

[45] H. Ochiai, M. Jang, K. Hirano, H. Yorimitsu, & K. Oshima, "Nickel-catalyzed carboxylation of organozinc reagents with CO2", *Org. Lett.*, **10,** 2681–2683 (2008).

[46] P. Munshi, A. D. Main, J. C. Linehan, C. C. Tai, & P. G. Jessop, "Hydrogenation of carbon dioxide catalyzed by ruthenium trimethylphosphine complexes: The accelerating effect of certain alcohols and amines", *J. Am. Chem. Soc.*, **124,** 7963–7971 (2002).

[47] S. Li, H. Xie, S. Zhang, Y. Lin, J. Xu, & J. Cao, "Tetramethylguanidine as an Inexpensive and Efficient Ligand for the Palladium-Catalyzed Heck Reaction", *Synlett*, **2005,** 1885–1888 (2005).

[48] M. Yadav, J. C. Linehan, A. J. Karkamkar, E. van der Eide, & D. J. Heldebrant, "Homogeneous Hydrogenation of CO 2 to Methyl Formate Utilizing Switchable Ionic Liquids", *Inorg. Chem.*, **53,** 9849–9854 (2014).

[49] J. Kothandaraman, A. Goeppert, M. Czaun, G. A. Olah, & G. K. Surya Prakash, "CO2 capture by amines in aqueous media and its subsequent conversion to formate with reusable ruthenium and iron catalysts", *Green Chem.*, **18,** 5831–5838 (2016).

[50] J. Artz, T. E. Müller, K. Thenert, J. Kleinekorte, R. Meys, A. Sternberg, A. Bardow, & W. Leitner, "Sustainable Conversion of Carbon Dioxide: An Integrated Review of Catalysis and Life Cycle Assessment", *Chem. Rev.*, **118,** 434–504 (2018).

[51] V. De La Fuente, C. Godard, E. Zangrando, C. Claver, & S. Castillón, "A phosphine-free Pd catalyst for the selective double carbonylation of aryl iodides", *Chem. Commun.*, **48,** 1695–1697 (2012).

[52] L. Jiang, J. Timothy, & F. Zou, "Catalytic hydrogenation",Patent no. US8242318B2, 1–7 (2012).

[53] U. Flörke, U. Ortmann, & H. -J Haupt, "Rhodium(I)-cyclooctadiene (cod) complexes with the N-donor ligands 1,8-diazabicyclo[5.4.0]undec-7-ene (dbu) and 1,5-diazabicyclo[4.3.0]non-5-ene (dbn)", *Acta Crystallogr. Sect. C*, **48,** 1663–1665 (1992).

[54] T. N. Hill, A. Roodt, & G. Steyl, "Probing the 'Venus fly-trap' parameters of cyclo-octadiene in selected β-diketonato complexes of platinum(II) and the nickel-triad from a spectroscopic, X-ray crystallographic and DFT study", *Polyhedron*, **50,** 82–89 (2013).

[55] G. A. Andrade, A. J. Pistner, G. P. A. Yap, D. A. Lutterman, & J. Rosenthal, "Photocatalytic Conversion of CO2 to CO Using Rhenium Bipyridine Platforms Containing Ancillary Phenyl or BODIPY Moieties", *ACS Catal.*, **3,** 1685–1692 (2013).

[56] A. Anaby, M. Feller, Y. Ben-David, G. Leitus, Y. Diskin-Posner, L. J. W. Shimon, & D. Milstein, "Bottom-Up Construction of a CO2-Based Cycle for the Photocarbonylation of Benzene, Promoted by a Rhodium(I) Pincer Complex", *J. Am. Chem. Soc.*, **138,** 9941–9950 (2016).

[57] P. Voyame, K. E. Toghill, M. A. Méndez, & H. H. Girault, "Photoreduction of CO2 using [Ru(bpy)2(CO)L] n+ catalysts in biphasic solution/supercritical CO2 systems", *Inorg. Chem.*, **52,** 10949–10957 (2013).

3 Synthesis and characterization of amidine and guanidine containing complexes

What to expect

The basic theory of the characterization methods used, followed by the synthesis and characterization of the complexes.

3.1 Introduction

The synthesis and characterization of Rh(I) and Pd(II) complexes containing amidines or guanidines (Fig. 3.1) as potential ligands are primarily discussed in this chapter, along with preliminary solution studies of the bases with CO_2. Characterization was performed by various techniques which included IR, ^{1}H and ^{13}C NMR and UV/Vis spectroscopy. Three of the complexes that were synthesized were fully characterized by single crystal X-ray diffraction (SC-XRD) and will be discussed in Chapter 4. The techniques used play a major role in identifying reactants, possible intermediates and products within a reaction mixture. The reaction mechanisms can also be evaluated by chemical kinetics, using UV/Vis spectroscopy, and was performed on two of the Rh(I) complexes that were synthesized (Chapter 5).

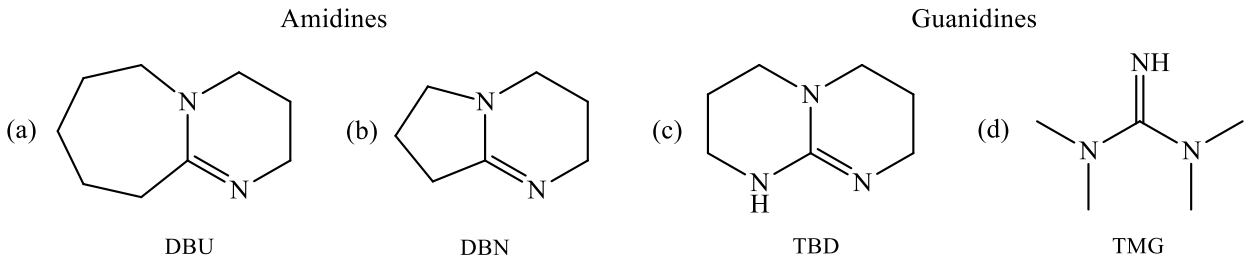

Figure 3.1: Structures of the four bases/ligand models being assessed. The amidines; (a) 1,8-diazabicyclo[5.4.0]undec-7-ene (**DBU**) and (b) 1,5-diazabicyclo[4.3.0]non-5-ene (**DBN**). The guanidines; (c) 1,5,7-triazabicyclo[4.4.0]dec-5-ene (**TBD**) and (d) 1,1,3,3-tetramethylguanidine (**TMG**) .

To motivate the use of these techniques, the basic theory concepts relating to the characterization methods will be discussed first, along with the applicable theory of chemical kinetics, before continuing with the characterization of the synthesized complexes.

3.2 Spectroscopic techniques

3.2.1 Infrared spectroscopy

Infrared (IR) radiation has low energy due to its long wavelength (lower frequency) and is found in the electromagnetic spectrum between the visible and microwave regions. The energy from IR radiation is absorbed and converted by organic molecules into molecular vibrations, with IR spectroscopy utilizing the region between 251 cm^{-1} and 4000 cm^{-1} to collect the absorption data of these molecular vibrations. The wavelength or frequency of absorption can be influenced by the geometry of atoms, the force constants of the bonds and even the relative masses of the atoms [1]. The absorption band intensity is usually reported in semiquantitative terms (w = weak, m = medium and s = strong), while the positions in the IR spectra are presented as wavenumbers $\bar{\nu}$ (often referred to as "frequencies") whose units are cm^{-1} and is reciprocally related to wavelength. The energy of the wavenumber can be calculated from the following equation

$$E = h\nu = hc\bar{\nu} \qquad \text{Eq. 3.1}$$

In Eq. 3.1 h is Planck's constant, ν is the frequency and c is the speed of light.

Molecular vibrations consist of different types, of which stretching and bending are two important ones. The former is a rhythmic movement that occurs along the bond axis where the interatomic distance is decreasing or increasing. The latter involves a change in the bond angles with a common atom or the movement of a group of atoms with respect to the rest of the molecule, with the group of atoms not moving with respect to each other, such as twisting, rocking and torsional vibrations. Not all vibrations in a molecule are observed in the IR spectra; only those that result in a rhythmic change in the dipole moment. This occurs when the vibration causes a fluctuation in the charge distribution, and consequently the molecule's electric field, which interacts with the electric field of the radiation. If the frequency of the natural vibration of the molecule and the radiation match, the amplitude increases.

The general trend of the IR spectra shows that the stretching frequencies are higher than the corresponding bending frequencies, and hydrogen bonds have a higher stretching frequency than bonds to heavier atoms, while stretching frequencies increase with increasing bond strengths. In the case of organometallic complexes, the specific frequency regions that are generally assigned to organic compounds are between 5000-500 cm^{-1}, whereas metal bonds are below 500 cm^{-1} and are often cumbersome to assign. However, the abundance of tables containing organic bond identification (fingerprint) regions assist in allocating the known organic compounds to their peaks.

Thus, for inorganic synthesis, IR spectroscopy is used as a method to broadly identify the coordination of ligands to a metal centre by comparing the fingerprint regions of the free ligand, and by noting a shift in the peaks, the product formation may be confirmed. This is because of the donating or withdrawing of the electron density about the coordinating atom of the ligand which should result in a theoretical shift (higher or lower, respectively) of the affected peaks [2]. The equation below (Eq. 3.2) explains the shift by relating the wavenumber to the force constant between the bonds i.e. bond strength.

$$\bar{\nu} = \frac{1}{2\pi c}\sqrt{\frac{k}{\mu}} \qquad \text{Eq. 3.2}$$

Here *c* is the speed of light, μ is the reduced mass and *k* is the force constant between the bonds of two atoms. Since *c* and μ are both constants, the wavenumber is directly proportional to the force constant. Thus, an increased force constant translates to a stiffer "spring" (stronger bond) which causes a higher wavenumber, and vice versa.

3.2.2 NMR spectroscopy

Nuclear magnetic resonance (NMR) spectroscopy makes use of the absorption of electromagnetic radiation (Radio-frequency region between 4 – 900 MHz) when in a strong magnetic field. Unlike IR and UV/Vis absorption, the nuclei of the atoms are involved in the absorption process, and not the electrons. This inherently means that the assessment is element specific, with ^{1}H and ^{13}C being the most common. The theory relating to this technique is more complex than IR and UV/Vis spectroscopy but affords more clarity on the structure determination of the compound, as well as

impurities, than the aforementioned techniques. Thus, an overview of the important aspects relating to NMR spectroscopy will be discussed.

All nuclei carry a charge but only some can generate a magnetic dipole by spinning about the nuclear axis, when the number of protons and neutrons are not equal [1]. The quantum spin number (*I*) helps to describe the angular momentum of the magnetic dipole. The spin number (*I*) can be determined by using the atomic number (*A*) and the atomic mass (*M*) of an element which may lead to one of three sets of values:

- When *A* and *M* are both even, the nucleus will have no net spin (*I* = 0); e.g. ${}^{12}_{6}C(0)$, ${}^{16}_{8}O(0)$.
- When *A* and *M* are both odd, or *A* is even and *M* is odd, the nucleus will have a half-integer spin (*I* = 1/2, 3/2, 5/2, etc); e.g. ${}^{1}_{1}H(\frac{1}{2})$, ${}^{13}_{6}C(\frac{1}{2})$.
- When *A* is odd and *M* is even, the nucleus will have an integer spin (*I* = 1, 2, 3, etc); e.g. ${}^{2}_{1}H(1)$, ${}^{14}_{7}N(1)$.

From the examples above it can be seen that elemental isotopes are vital for there to be a magnetic dipole. That is why ^{1}H NMR is the most prevalent (99.98 % abundance), followed by ^{13}C NMR (1.1 % abundance).

A nucleus that has a *I* = ½ will have two possible orientations (2*I* + 1) of equal energy. When a magnetic field is applied, the energy levels split; one is anti-parallel (+½, high energy level) to the magnetic field and the other parallel (-½, low energy level) to it. The nuclei are differentiated from one another, due to shielding and deshielding effects caused by the magnetic field created by the electrons around the nucleus [3]. This field opposes the applied field. When the electron density around the nucleus increases the effective magnetic field that it experiences decreases (shielding), resulting in a smaller energy difference between the two spin states and a lower resonance frequency. The opposite holds true for deshielding. The chemical shifts that, in this case, the protons experience is small and are rather converted to a more convenient value by making use of a proton reference frequency. For ^{1}H and ^{13}C nuclei, tetramethylsilane (TMS) is adopted as the reference frequency because all twelve protons are equivalent and have a single peak. The shifts (δ) are converted using Eq. 3.3 and expressed in ppm (parts per million).

$$\delta = (v - v_0)/v_0 \qquad \text{Eq. 3.3}$$

With v being the specific nuclei resonance frequency and v_0 the reference frequency. These shifts vary depending on the nuclei in question and the general ranges for hydrogen and carbon atoms are 1-10 ppm (^{1}H) and 0-220 ppm (^{13}C).

Proton NMR is affected by two types of environmental effects; chemical shifts (discussed above) and spin-spin coupling. The latter effect is caused by changes in the magnetic fields by adjacent nuclei that result in multiple transitions because the energy levels split, resulting in more than one peak. The difference between the peaks are independent of the applied magnetic field and are called the coupling constant (*J*) and is measured in hertz.

Carbon NMR, on the other hand, has two main advantages over ^{1}H NMR, even though it is about 6000 times less sensitive. Firstly, it provides information on the molecular backbone of the structure, where the protons describe the periphery. The chemical shifts, noted early, are a lot larger and result in less spectral overlap, as would be seen in the proton spectra. Various forms of spin-spin coupling between carbons is not observed because of the low natural abundance of ^{13}C, which means the probability of two identical isotopes being adjacent to one another is unlikely. While the theory relating to NMR for both carbons and protons are more extensive than has been discussed above, the basic theory and application has been addressed to validate its uses.

3.2.3 UV/Vis spectroscopy

Ultraviolet (UV) and visible radiation lies in the region from 200-800 nm. Their absorption by atoms and molecules leads to the excitation of electrons within them, from lower to higher energy levels. The light that is absorbed have precise energy values (because the energy levels of the matter are quantized) causing specific energy level transitions based on the absorbed energy. These precise energies are related to a certain wavelength, as shown with Eq. 3.1, which can cause the possible electronic transitions shown in Fig. 3.2. The diagram shows that the energy required increases in the order of; σ-bonding orbitals > π-bonding orbitals > non-bonding (*n*) orbitals.

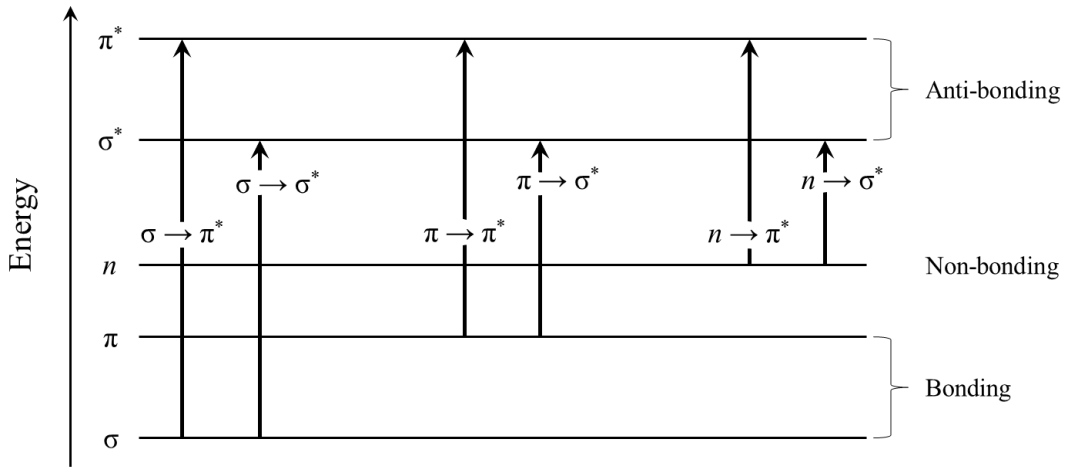

Figure 3.2: The electronic transitions that are possible within a typical metal complex in the UV/Vis energy range. The horizontal lines indicate the energy level and the arrows show the transition from one level to another.

Each arrow indicates the excitation of an electron from the ground state (HOMO – highest occupied molecular orbital) to the excited state (LUMO – lowest unoccupied molecular orbital). The gap between the two energy levels relates to the energy required (i.e. the larger the gap, the larger the energy must be), which correlates to a shorter wavelength being absorbed. The absorption intensity can then be related to the concentration of the complex, using the Beer-Lambert law (Eq. 3.4) [4].

$$A = \varepsilon l c \qquad \text{Eq. 3.4}$$

Here l is the optical path length and ε the molar extinction coefficient (which is constant for a specific compound at a certain wavelength) provided that the absorbance A is < 1. This is useful in reaction kinetic studies, where the absorbance change versus time will aid in evaluating the rate of change in the concentration of the reactants or products. From the data, the rate order and rate equation can be determined, and a reaction mechanism proposed. Reaction kinetics is explained in more detail, below, in Par. 3.2.4.

3.2.4 Chemical kinetics

A main purpose of kinetic studies is the elucidation of the reaction mechanism and possible transition states. This is achieved by studying the reaction rate of the chemical process at different experimental conditions such as temperature, pressure, solvent and concentration. Due to each molecule having a unique absorption spectrum, spectroscopy is often used to measure kinetic reactions. The use of UV/Vis spectrometry is one method that measures reaction rates based on the change in absorption, which can then be related to a change in concentration using Eq. 3.4. Therefore, the reaction rate is defined as the measured change in the concentration of the products or reactants per unit time [5]. For a simple reaction (Eq. 3.5) such as:

$$aA + bB \rightleftharpoons cC \qquad \text{Eq. 3.5}$$

Where a, b and c are the coefficients of the reactants (A and B) and the product (C). The values k_1 and k_{-1} are the forward and reverse rate constants respectively, which relates the rate of change to the reagent concentrations, with [ ] denoting concentration (Eq. 3.6).

$$Rate = \frac{-1}{a}\frac{d[A]}{dt} = \frac{-1}{b}\frac{d[B]}{dt} = \frac{1}{c}\frac{d[C]}{dt} = k_1[A]^m[B]^n - k_{-1}[C] \qquad \text{Eq. 3.6}$$

The values *m* and *n* represent the order of the reaction with respect to the concentrations of A and B, with the sum of the values for m and n describing the order of the overall reaction (rate law). The order describes the dependence in a change in concentration of one or both reacting species. The order can be experimentally determined, often with difficulty, but is circumvented by applying pseudo first-order conditions were one reactant is in excess (at least 10 equivalence in excess) with respect to the other reactant, for example {[A] >> [B]; [C]} [6]. Using Eq. 3.6, pseudo first-order conditions and integration, the observed pseudo first-order rate constant (Eq. 3.7) can be expressed as

$$k_{obs} = k_1[A]^m + k_{-1} \qquad \text{Eq. 3.7}$$

If the order of B is $n = 1$, then the reaction in A is first-order and the rate constants can thus be determined by plotting the observed rate constants (k_{obs}) at various concentrations of [A], where k_1 is the gradient of the graph and k_{-1} is the intercept. If the intercept, k_{-1}, is not through the origin, it may indicate the presence of parallel reaction or an equilibrium (reverse reaction) or even higher order in some of the reactants.

In the case of a reverse reaction, the equilibrium constant, *K*, (Eq. 3.8) is defined by

$$K = \frac{k_1}{k_{-1}} \quad \text{Eq. 3.8}$$

The k_{obs} values can be obtained from the kinetic runs at various concentration of entering ligand from the absorbance *vs.* time graphs, Eq. 3.6 was integrated, in terms of [C], between time $t = 0$ and $t = t$, yielding the logarithmic form of the rate equation (Eq. 3.9).

$$\ln\frac{[C]_t}{[C]_0} = k_{obs}t \quad \text{Eq. 3.9}$$

Incorporating the Beer-Lambert law into Eq. 3.9 (where $\frac{[C]_t}{[C]_0} = \frac{A_\infty - A_t}{A_\infty - A_0}$) and manipulating the result, leads to exponential form of Eq. 3.9 as

$$A_t = A_\infty - (A_\infty - A_0)e^{k_{obs}t} \quad \text{Eq. 3.10}$$

Here A_t and A_∞ are the absorbances after time *t* and infinite time, respectively. The time at which the reaction is complete, for all practical purposes, is A_∞. Thus, the k_{obs} (if the reaction is first order) can be determined from a plot of the least-squares fit of the absorbance (Eq. 3.10) *vs.* time data. The time it takes for half of the reaction to be complete, for a first order reaction, can then be determined from the k_{obs} value from Eq. 3.11

$$t_{1/2} = \frac{\ln 2}{k_{obs}} = \frac{0.6932}{k_{obs}} \quad \text{Eq. 3.11}$$

The equations above describe the reaction rate, but by performing the kinetic study at different temperatures and using the Eyring equation, insight into the mechanism can also be established.

Finally, by plotting the pseudo first-order constants as determined from Eq. 3.10 vs. [A] in Eq. 3.8, the second order forward k_1, and parallel or reverse rate constant k_{-1}, may be obtained.

3.3 Single-crystal X-ray diffraction (SC-XRD)

Electromagnetic radiation in the X-ray region ranges from 10^{-2} to 10 nm and has a longer wavelength than gamma rays but shorter than UV rays. Two common types of X-ray diffraction (XRD) techniques are powder and single-crystal XRD [7]. The former technique is a fast and accurate approach to identifying a known substance (such as e.g. in mineralogy) or to verify that unknown samples are of the same material. However, the structural data is difficult to obtain because the molecules in the powder do not have periodicity. That is the benefit of SC-XRD, even

though obtaining appropriate solid samples (specifically single crystals) may be difficult to grow. It is often time and data intensive, and has a high cost associated with the equipment. Simply put, single-crystal XRD is a method in which a crystal is bombarded from various angles with an X-ray beam, with the resulting diffraction patterns being measured and recorded. The diffraction patterns are then aggregated and converted (Fourier transform) to an electron density map, from which a unit-cell can be created. Through refinement of the data the average bond lengths, atomic positions and the relative orientations of the molecules in the crystal can be obtained.

The periodicity of crystal structures is the result of the arrangements of the atoms or molecules in the lattice. This can be considered a repetition of a unit-cell, which has the same symmetry as the entire crystal. The unit-cell is the smallest volume, which best describes the crystal, and can be repeated in all directions, and can be primitive (contain one lattice point) or non-primitive (more than one lattice point). It can further be defined by three edge lengths (*a, b, c*), angles (α, β, γ) and crystal planes called Miller indices (*h k l*). The unit-cell can also be categorized under a Bravais lattice, crystallographic point group and space group, of which there are 14, 32 and 230 possibilities respectively [8].

Since the unit-cell represents the crystal, the diffraction pattern that results from one unit-cell is small but is amplified because of the periodicity. The way in which primary diffraction occurs is best described by Bragg's law, which also helps detail how the geometric data of the molecule, mentioned above, is determined.

3.3.1 Bragg's Law

Bragg's law (Eq.3.12) helps to define the conditions necessary for diffraction to occur in a crystalline solid, more importantly, for constructive interference [9].

$$n\lambda = 2d \sin\theta \qquad \text{Eq. 3.12}$$

Here n is a positive integer, λ is the wavelength of the incident X-rays, d is the distance between the planes and θ is the scattering angle. The diagram (Fig. 3.3) below helps illustrate Bragg's law.

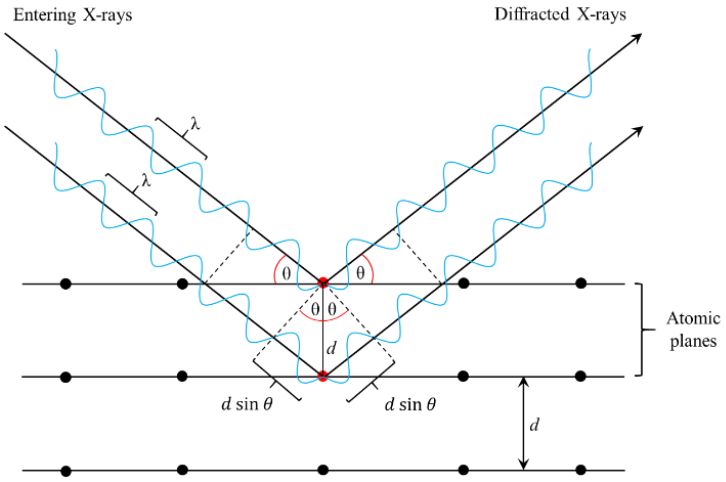

Figure 3.3: X-ray diffraction according to Bragg's law. Where λ is the wavelength of the X-rays, θ is the scattering angle and *d* is the distance between the planes.

The X-rays are not limited to diffraction from atoms on the surface of the crystal and can penetrate deeper into the lattice and diffract constructively if it abides to Bragg's law. The crystal is also rotated slowly to have a more comprehensive collection of diffraction patterns to provide sufficient data to determine the structure.

The resulting diffraction spots of the crystal lattice is represented through the reciprocal lattice, which has planes (Miller indices) that can be indexed and be assigned to a Laue class. However, none of the above information accounts for the relative intensities of the reflections. By applying a Fourier transformation method to the relative intensities, they can be discerned from each other.

3.3.2 Structure factor

The reflections that are possible in a crystal are described by the reciprocal lattice through Miller indices (*hkl*), with the intensities effected by various factors of the cell contents. The intensities and the phase of the diffracted X-rays are described by a Fourier series and are quantified through the structure factor ($\boldsymbol{F}_{hkl}$) and is formulated from the displacement vector ($\boldsymbol{r}_j$) towards the j^{th} atom in a unit-cell, which is expressed in terms of fractional coordinates (Eq.3.13).

$$\boldsymbol{r}_j = x_j a_1 + y_j a_2 + z_j a_3 \qquad \text{Eq. 3.13}$$

Here x_j, y_j and z_j are the coordinates of each atom in the unit-cell and a_1, a_2 and a_3 are the basis vectors. The reciprocal lattice position vector ($\boldsymbol{G}_j$) is expressed as

$$\boldsymbol{G}_j = hb_1 + kb_2 + lb_3 \qquad \text{Eq. 3.14}$$

Here *h*, *k* and *l* are the Miller indices and b_1, b_2 and b_3 are the reciprocal basis vectors. The above two equations help to determine the phase difference (ϕ_j) when the incident X-ray beam is diffracted by one set of atoms in a plane and also by another set of atoms in a parallel plane that is offset by a displacement vector ($\boldsymbol{r}_j$). The pathlength of the phase difference can be determined from the dot product (Eq. 3.15) of Eq. 3.13 and Eq.3.14, from which it can be seen that the mathematical relationship of the dual basis vectors are integral multiples of 2π.

$$\phi_j = \boldsymbol{G}_j \cdot \boldsymbol{r}_j = 2\pi(hx_j + kx_j + lz_j) \qquad \text{Eq. 3.15}$$

The structure factor equation (Eq. 3.16) takes the scattering power of each atom (f_j – scattering factor of j^{th} atom) and atom positions (Eq. 3.15) into account.

$$\boldsymbol{F}_{hkl} = F_{hkl}e^{i(\phi_{hkl})} = \sum_{j=1}^{N} f_j e^{2\pi i(hx_j + kx_j + lz_j)} \qquad \text{Eq. 3.16}$$

The above equation illustrates the dependence of the structure factor on the relative atom positions. The equation (Eq. 3.16) can also be expanded to the cosine waves (Eq. 3.17)

$$\boldsymbol{F}_{hkl} = \sum_{j=1}^{N} f_j \left[\cos 2\pi\left(hx_j + kx_j + lz_j\right) + i \sin 2\pi\left(hx_j + kx_j + lz_j\right)\right] \qquad \text{Eq. 3.17}$$

The result of the above equation allows the experimental intensity (energy) of the scattered wave ($I_{0(hkl)}$) to be related to the structure factor ($F_{0(hkl)}$) because the energy in cosine waves are proportional to the square of wave amplitudes (Eq. 3.18).

$$I_{0(hkl)} \propto \left| F_{0(hkl)} \right|^2 \qquad \text{Eq. 3.18}$$

The above equations allow for the resultant diffraction wave intensities of the atoms to be quantified through $I_{0(hkl)}$. However, the measured $F_{0(hkl)}$ can further be used to determine the electron density of the atoms. Since the X-ray waves are diffracted by the electrons of an atom, when the atomic number increases (more electrons) the number of reflected waves increase due more electrons being able to diffract the X-rays which results in a larger diffraction intensity, and vice versa. Therefore, to determine the relative electron densities the calculations must be performed in three dimensions, which means that the unit-cell volume (*V*) must be considered.

Thus, the relative electron density at the location, ρ(x_j, y_j, z_j), of the j^{th} atom is shown below [9].

$$\rho(x_j, y_j, z_j) = \frac{1}{V}\sum_{hkl} F_{hkl} e^{-2\pi i(hx_j + kx_j + lz_j)} \quad \text{Eq. 3.19}$$

This allows for the known atoms of the proposed compound to be assigned based on the relative electron densities from Eq. 3.19. If the atoms in the crystal are not known, the ability to solve the crystal becomes extremely difficult, which is why preliminary evaluation of the compound must be done and can include NMR, IR spectroscopy, synthesis method and solvents used for recrystallization.

3.3.3 Phase problem

As mentioned before, the amplitude and the phase difference are needed to determine the structure factor and the relative electron densities, but only the amplitude can be measured and not the corresponding phase. Therefore, to determine the structure, the phase angles must be solved indirectly. There are two approaches that are commonly used; direct method and Patterson function. The former method is used when the crystal structure contains no heavy atoms and the latter approach is used when there are one or a few heavy atoms present.

3.3.3.1 Direct methods

The direct method takes advantage of the fact that the electron density cannot be negative within the crystal, which restricts the possible phase angles between reflections. Using a trial and error process, whereby the reflections that contribute the most to *F* are chosen as approximations that appear promising, an initial estimate of the real structure can be determined and further refined [8].

3.3.3.2 Patterson function

The Patterson function (Eq. 3.20) or Patterson map is essentially Eq. 3.19 with the difference being that the amplitude is squared, and the waves are in phase.

$$\rho(u, v, w) = \frac{1}{V}\sum_{hkl} (F_{hkl})^2 e^{-2\pi i(u,v,w)} \quad \text{Eq. 3.20}$$

In principle, this means that if there are an amount of N atoms in the unit-cell there will be a corresponding N^2 number of vectors between these atoms. Therefore, this process, maps the atoms relative to each other and not where they are positioned relative to the unit-cell. Therefore, the peaks are not assigned to electron density but rather the vectors between pairs of atoms. Each peak location (u, v, w) is assigned to two atoms whose coordinates (x, y, z) differ by values u, v, w respectively. The initial estimated structure will predominately contain the position(s) of the heavy atom(s) in the unit-cell, after which the remaining structure can be determined by other techniques [8].

3.3.4 Least squares refinement

When the structure is refined from the approximated structure, the agreement between the amplitudes of the structure factors of the observed (F_o) and calculated (F_c) structures are improved. This is measured by the conventional residual factor (R factor) and is defined by Eq. 3.21 [8].

$$R = \frac{\sum|F_o - F_c|}{\sum|F_o|} \qquad \text{Eq. 3.21}$$

The above equation illustrates that the agreement improves as the R factor decreases. Refinement uses the least squares analysis which adjust the parameters (such as atomic displacement and atom positions) in order to improve the agreement between the two data sets (F_o and F_c). When the least squares analysis is performed, several cycles may be done to improve the convergence of the R factor to assess the progress. A well solved crystal will generally have an $R < 0.07$, but this only indicates the precision and not the accuracy. The residual factor can be improved by incorporating a weighting factor for all the reflections (w) measured in the experiment [8].

$$wR = \left(\frac{\sum|w|F_o - F_c|^2|}{\sum|wF_o^2|}\right)^{1/2} \qquad \text{Eq. 3.21}$$

The weighted residual factor (wR) is generally double that of the R factor.

3.4 Synthesis and spectroscopic characterization of complexes

3.4.1 Chemicals and instrumentation

The reagents used for all the synthesis methods were purchased from Sigma-Aldrich and were of analytical grade and used without further purification, unless stated otherwise. Carbon dioxide (CO_2) was supplied by Air Liquide, with the cylinder containing a dip tube and coupled to a nozzle to obtain solid CO_2. The organic solvents were dried and distilled before being used. The infrared spectra from neat samples were recorded on a Bruker Tensor Standard System spectrophotometer with a laser range of 4000-370 cm^{-1} and reported in cm^{-1}. The solution infrared spectra were collected in a NaCl cell using dry organic solvents and in the same range as the neat samples. The UV/Vis time-resolved spectra were collected either on a Hi-Tech Scientific Stopped SF-61 DX2 unit, which was connected to a Hi-Tech Scientific SU-40-UV/Vis spectrophotometer unit or a Varian Cary 50 Conc or Varian 100 spectrophotometers, with 1.000 ± 0.001 cm path length tandem quartz cells. The SF-61 DX2 unit is equipped with a constant temperature cell (accuracy of ± 0.1 °C) that is also connected to a Julabu MPV thermostated water bath (accuracy of ± 0.1 °C) which was fitted with a circulator. All the metal complexes were characterized by ATR sampling technique. The ^{1}H and ^{13}C NMR spectra for the Rh(I) and the bases were obtained in C_6D_6 and the Pd(II) complexes in $CDCl_3$ solutions on a 600 MHz Bruker spectrometer. All the chemical shifts (δ), reported in ppm, are relative to tetramethylsilane (TMS), using the C_6D_6 (7.14 ppm, 127.7) and $CDCl_3$ (7.28 ppm, 77.0 ppm) peaks for ^{1}H and ^{13}C respectively.

3.4.2 Preliminary solution study of CO_2

The ability of the four bases/ ligands as shown in Fig. 3.1, to coordinate to CO_2 was preliminary assessed using solution infrared spectroscopy. The method entailed obtaining the spectra of the ligand (0.35 mmol) in 15 ml of dichloromethane (DCM) followed by the semi-quantitative addition of CO_2 (~0.35 mmol) to the ligand in DCM. The mass of the CO_2 that was added was approximately 20 mg to account for sublimation thereof before being added to the ligand solution.

Three solvents (DCM, toluene and acetonitrile) were assessed for compatibility in their IR range (3000 – 1300 cm^{-1}) of the ligands and DCM was found to overlap the least.

The frequency of the C=N bond in DBU, DBN, TMG and TBD were 1614 cm^{-1}, 1652 cm^{-1}, 1594 cm^{-1} and 1627 cm^{-1} respectively and $\bar{\nu}$ = 2338 cm^{-1} for the carbonyl peak of carbon dioxide. No shifts were observed in the C=N bond of DBU, DBN and TMG after the addition of CO_2 but a small peak was observed at a slightly high frequency (~50 cm^{-1}) which corresponds to the "coordinated" CO_2 bond (Fig. 3.4). Additionally, the peak size decreased in order of DBU, DBN and TMG while no visible change in the absorbance of CO_2 being observed.

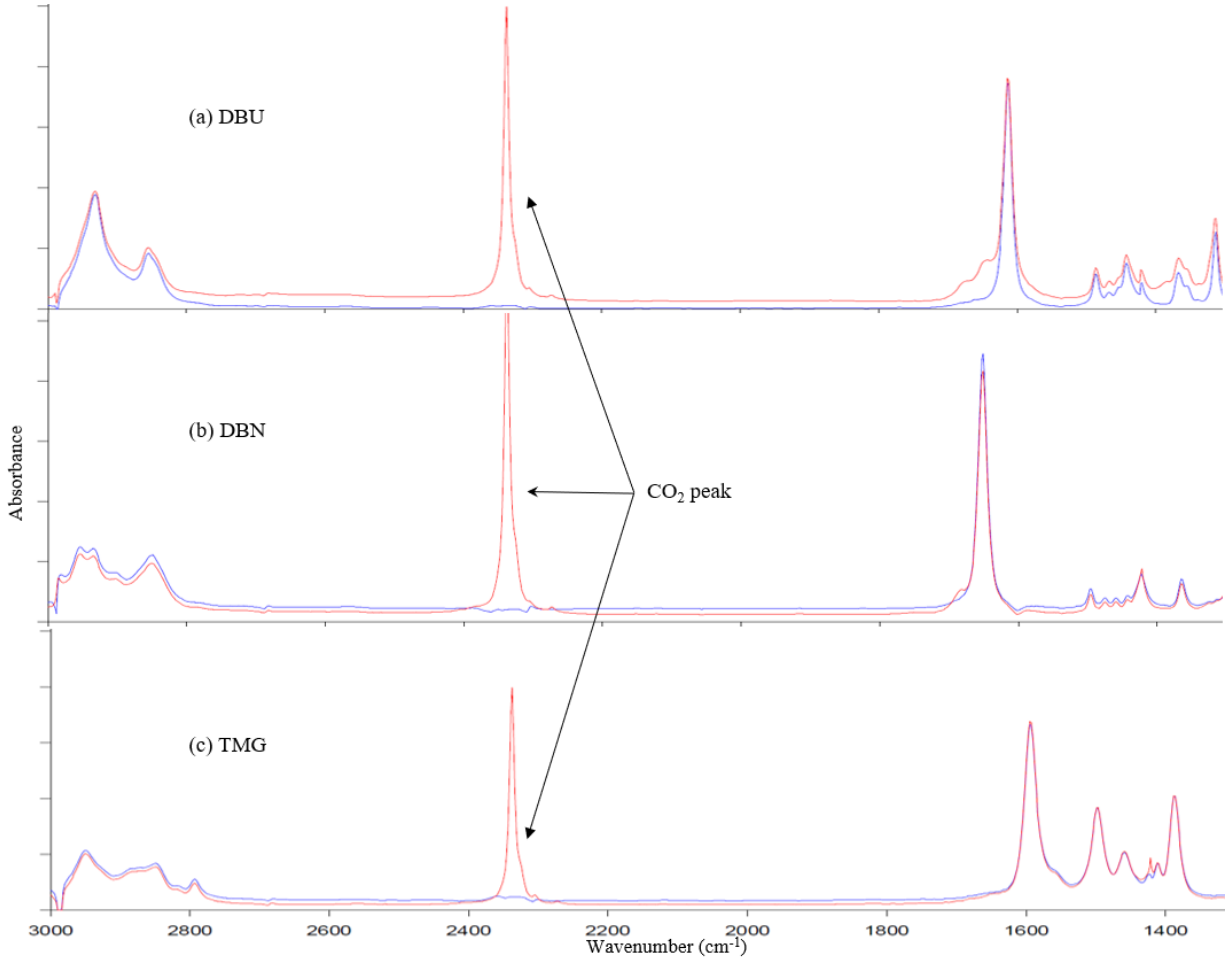

Figure 3.4: The solution IR spectra of; (a) DBU, (b) DBN and (c) TMG. The blue indicates the spectra of only the ligands in DCM and the red shows the spectra after the addition of CO_2 to the ligand solution.

However, TBD behaved differently. Firstly, it was sparingly soluble in DCM even with mild heating but was assessed nonetheless for uniformity due to possible solvent effects of DCM on CO_2. After the addition of CO_2, the IR spectra revealed a significant absorbance reduction in the $\bar{\nu}$ = 2338 cm^{-1} peak of carbon dioxide and four new peaks ($\bar{\nu}$ = 1712 cm^{-1}, 1668 cm^{-1}, 1617 cm^{-1} and 1593 cm^{-1}) in the vicinity of the C=N bond of the pure TBD (Fig. 3.5(a)). An excess of CO_2 was then added, and the spectra showed absorption changes in the aforementioned new peaks (Fig. 3.5(b)).

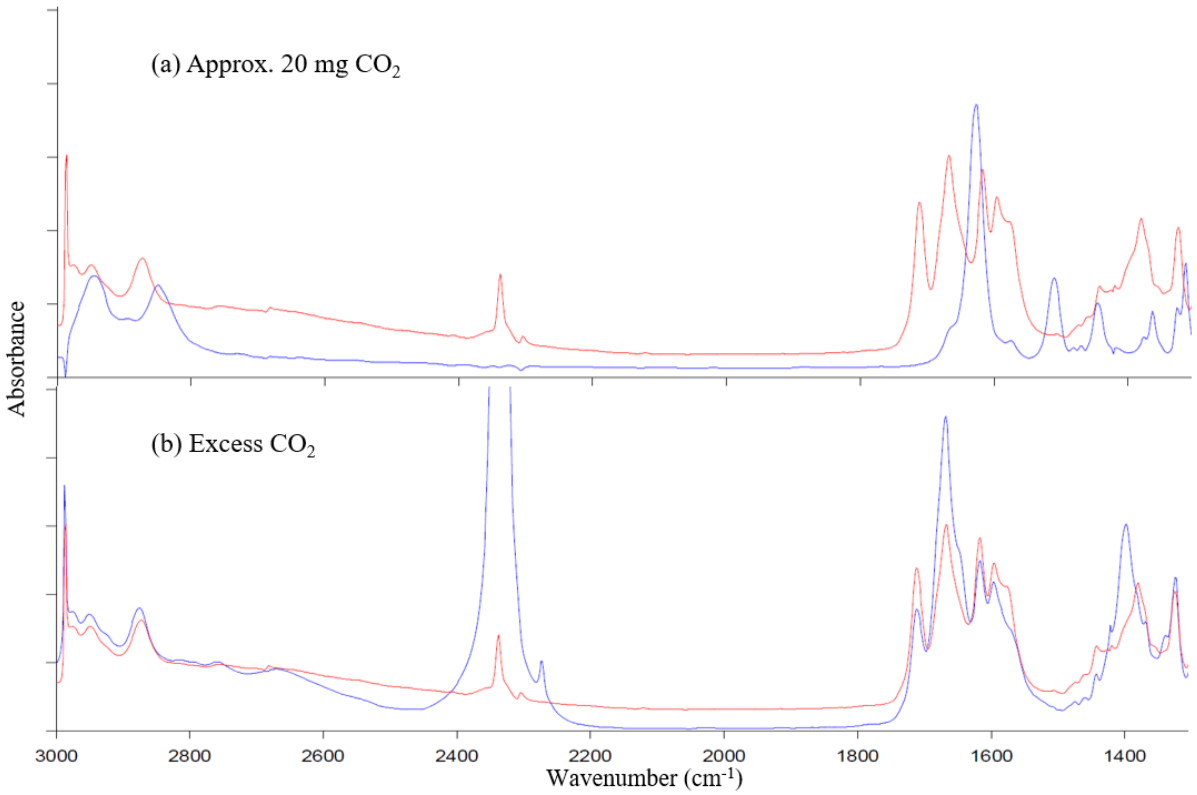

Figure 3.5: The solution IR spectra of TBD with (a) approximately 20 mg of CO_2 and (b) an excess of CO_2. The red indicates the same spectra which is TBD with the addition of the initial amount of CO_2 and the blue indicates the (a) pure TBD in solution and (b) excess addition of CO_2.

The four peaks can be assigned to the TBD-CO_2 and [TBDH][HCO_3] products and correlate with those observed by Villiers *et al.* [10]. The asymmetric stretching frequencies of the C=O and C=N bonds for the former product are $\bar{\nu}$ = 1712 cm^{-1} and 1605 cm^{-1} respectively. In the case of the bicarbonate product, the C=N bond was found at $\bar{\nu}$ = 1660 cm^{-1} and $\bar{\nu}$ = 1600 cm^{-1} for the CO_3 of the bicarbonate ion. The peaks are also of comparative absorbance which may indicate an

equilibrium between the zwitterionic and bicarbonate products, which is illustrated in Fig. 2.14. Furthermore, in Fig. 3.5(b), the excess CO_2 resulted in an absorbance increase in the C=N bond of the bicarbonate product and peak reduction in the other peaks. This may be caused by the additional adventitious water introduced by the excess solid CO_2, resulting in an equilibrium shift towards the bicarbonate formation.

Finally, all the ligands formed an off-white precipitate when an excess of CO_2 was added, which corresponds to the formation of the ligand-bicarbonate product as noted in literature [10–12]. Based on the results that all the ligands could coordinate to CO_2 with various extents, attempts were made to try coordinate them to metal complexes to enable "metal-assisted" carbon dioxide fixation.

3.4.3 ^{1}H and ^{13}C NMR spectra of the amidine and guanidine ligands

For comparison purposes, the values of the ^{1}H and ^{13}C NMR spectra of the four bases (Fig. 3.1) are provided below. The values assisted in assigning the peaks and to note whether they were in fact coordinated and how shielding may have affected the spectra when the bases were coordinated. Direct comparison of the NMR values below with the Rh(I) complexes (Par. 3.4.4) support that the bases are coordinated. However, because the Pd(II) complexes were not soluble in benzene, the values below could not be used for direct comparison with the Pd(II) complexes.

DBU:

^{1}H NMR (C_6D_6, 600 MHz): δ 3.40 (t, 2H), 2.73 (t, 2H), 2.65 (t, 2H), 2.40 (t, 2H), 1.55-1.47 (m, 4H), 1.32-1.23 (m, 2H), 1.19-1.12 (m, 2H)

^{13}C NMR (C_6D_6, 151 MHz): δ 159.3, 52.2, 48.1, 44.5, 37.2, 29.6, 28.6, 26.2, 23.0

DBN:

^{1}H NMR (C_6D_6, 600 MHz): δ 3.43 (t, 2H), 2.70-2.63 (m, 2H), 2.63-2.58 (m, 2H), 2.28 (t, 2H), 1.49-1.43 (m, 2H), 1.37-1.28 (m, 2H)

^{13}C NMR (C_6D_6, 151 MHz): δ 158.6, 50.7, 44.3, 42.9, 31.0, 21.2, 19.5

TMG:

^{1}H NMR (C_6D_6, 600 MHz): δ 2.65-2.25 (br, 12H)

^{13}C NMR (C_6D_6, 151 MHz): δ 166.8, 38.9

TBD:

^{1}H NMR (C_6D_6, 600 MHz): δ 3.12-3.00 (br, 4H), 2.58-2.50 (m, 4H), 1.53-1.44 (m, 4H)

^{13}C NMR (C_6D_6, 151 MHz): δ 150.5, 47.8, 41.6, 23.2

3.4.4 Synthesis of [Rh(COD)(L)Cl] complexes

The different amidine/ guanidine (for structures and names, see Fig. 3.1) rhodium(I) complexes were all prepared using the same procedure, as indicated in Fig. 3.6 [13]. The starting material [$Rh(COD)_2Cl_2$] (approx. 0.200 mmol) was dissolved in dioxane (10 ml) and the appropriate base (2 eq.) was added to the reaction mixture and left to stir overnight at room temperature. Pentane (5 ml) was subsequently added to the yellow solutions from which crystals suitable for SC-XRD analysis were formed.

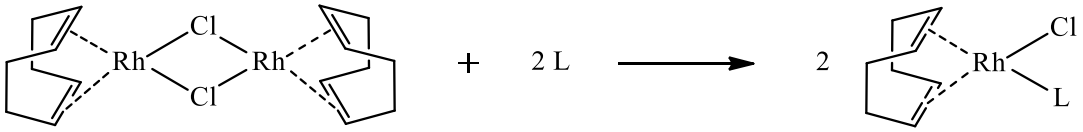

Figure 3.6: The general reaction scheme for the preparation of different [Rh(COD)(L)Cl] complexes (L = DBU, DBN and TMG).

3.4.4.1 [Rh(COD)(DBU)Cl]

The amidine, DBU (62 µl, 0.415 mmol), was added to the specified $[Rh(COD)_2Cl_2]$ solution (101 mg, 0.205 mmol) to yield the product [Rh(COD)(DBU)Cl].

Yield: 148.1 mg, 90.4 %

IR (cm^{-1}): $\bar{\nu}_{(C=N)}$ = 1606

^1H NMR (C_6D_6, 600 MHz): δ 4.98 (s, 1H), 4.89 (s, 1H), 3.64 (s, 1H), 3.57 (s, 1H), 3.51 (s, 1H), 3.43 (s, 1H), 3.11 (s, 1H), 2.96 (s, 1H), 2.48 – 2.22 (m, 8H), 1.94 (s, 1H), 1.67 (s, 2H), 1.59 (s, 2H), 1.53 (s, 1H), 1.46 (s, 1H), 1.27 (s, 1H), 1.27 (s, 1H), 1.15 (s, 2H), 0.95 (s, 1H), 0.92 (s, 1H)

^{13}C NMR (C_6D_6, 151 MHz): δ 163.0, 82.6 (d), 81.6 (d), 73.1 (d), 72.9 (d), 52.5, 46.9, 46.8, 39.0, 31.9, 31.3, 30.7, 30.4, 29.0, 27.3, 25.0, 22.0

3.4.4.2 [Rh(COD)(DBN)Cl]

The amidine, DBN (50 µl, 0.405 mmol), was added to the specified $[Rh(COD)_2Cl_2]$ solution (99 mg, 0.200 mmol) to yield the product [Rh(COD)(DBN)Cl].

Yield: 115.2 mg, 77.6 %

IR (cm^{-1}): $\bar{\nu}_{(C=N)}$ = 1650

^1H NMR (C_6D_6, 600 MHz): δ 4.95 (s, 2H), 3.54 (s, 2H), 3.24 – 3.14 (br, 2H), 3.04 – 2.88 (br, 2H), 2.37 (t, 2H), 2.36 – 2.28 (br, 4H), 2.23 (t, 2H), 1.64 (d, 4H), 1.27 – 1.21 (m, 2H), 1.21 – 1.16 (m, 2H)

^{13}C NMR (C_6D_6, 151 MHz): δ 162.3, 82.7 (d), 72.8 (d), 51.4, 45.7, 41.8, 33.2, 31.7, 30.5, 20.6, 18.9

3.4.4.3 [Rh(COD)(TMG)Cl]

The guanidine, TMG (51 µl, 0.406 mmol), was added to the specified $[Rh(COD)_2Cl_2]$ solution (101 mg, 0.204 mmol) to yield the product [Rh(COD)(TMG)Cl].

Yield: 126.9 mg, 86.0 %

IR (cm^{-1}): $\bar{\nu}_{(C=N)}$ = 1567, 1527

^1H NMR (C_6D_6, 600 MHz): δ 4.87 (s, 2H), 3.60 (s, 2H), 3.14 – 2.66 (br, 6H), 2.38 – 2.29 (br, 4H), 2.25 – 1.80 (br, 6H), 1.63 (d, 4H)

^{13}C NMR (C_6D_6, 151 MHz): δ 170.6, 80.8 (d), 73.4 (d), 40.8 – 39.3, 38.5 – 37.3, 31.5, 30.7

3.4.5 Synthesis of *trans*-$[Pd(L)_2Cl_2]$ complexes

The Pd(II) complexes containing the amidines/ guanidines (for structures and names, see Fig. 3.1), as ligands, were synthesized *via* a two-step process which first involved the synthesis of *trans*-bis(benzonitrile)dichloropalladium(II) (*trans*-$[Pd(PhCN)_2Cl_2]$) from $PdCl_2$ (Fig. 3.7(a)) and is described in Par. 3.4.4.1. In the second step, the different amidine/ guanidine palladium(II) complexes were all synthesized in the same manner as illustrated in Fig. 3.7(b) [14]. The ligand (2 eq.) was added to a solution of *trans*-$[Pd(PhCN)_2Cl_2]$ in toluene (5 ml) and left to stir overnight at room temperature. An orange precipitate formed which was then filtered and washed with toluene and dried. Crystals that were appropriate for SC-XRD analysis were obtained by recrystallization in DMF.

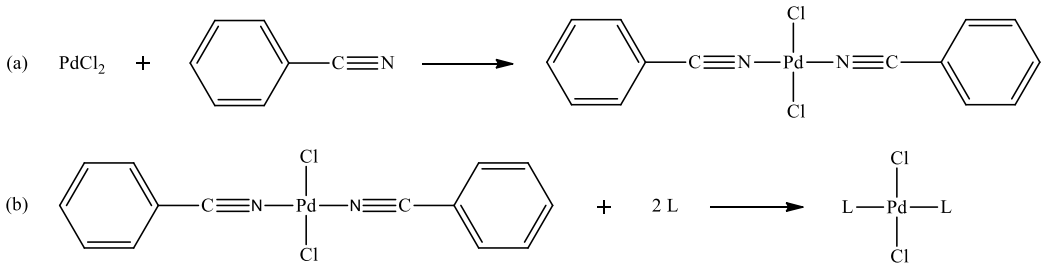

Figure 3.7: The general reaction schemes for the two-step preparation of different *trans*-$[Pd(L)_2Cl_2]$ complexes (L = DBU, DBN, TMG, TBD). (a) Synthesis of the precursor complex, *trans*-$[Pd(PhCN)_2Cl_2]$, from $PdCl_2$. (b) General reaction for the synthesis of the *trans*-$[Pd(L)_2Cl_2]$ complexes.

3.4.5.1 *trans*-[Pd(PhCN)$_2$Cl$_2$]

$PdCl_2$ (200.2 mg, 1.129 mmol) was refluxed at 100 ºC in benzonitrile (6 ml) for 30 minutes, which resulted in a red-brown solution. The hot solution was subsequently filtered, followed by the immediate precipitation of the product after the addition of petroleum ether (35 ml). The yellow product was then filtered and washed with petroleum ether (3 x 15 ml) and dried [15].

Yield: 318.6 mg, 73.6 %

IR (cm^{-1}): $\bar{\nu}_{(C=N)}$ = 2286

^{1}H NMR (C_6D_6, 600 MHz): δ 7.82 – 7.72 (m, 2H), 7.68 (d, 2H), 7.63 (t, 2H), 7.57 (t, 2H), 7.50 (t, 2H)

^{13}C NMR (C_6D_6, 151 MHz): δ 135.3, 133.4, 129.5, 122.2, 109.2

3.4.5.2 *trans*-[Pd(DBU)$_2$Cl$_2$]

The amidine, DBU (39 µl, 0.261 mmol), was added to the specified [Pd(PhCN)$_2$Cl$_2$] solution (50.0 mg, 0.130 mmol) to yield the product [Pd(DBU)$_2$Cl$_2$].

Yield: 44.1 mg, 70.2 %

IR (cm^{-1}): $\bar{\nu}_{(C=N)}$ = 1605

^{1}H NMR ($CDCl_3$, 600 MHz): δ 3.67 – 3.60 (br, 4H), 3.51 (t, 4H), 3.27 – 3.23 (br, 4H), 3.19 (t, 4H), 2.00 – 1.93 (br, 4H), 1.88 – 1.81 (m, 4H), 1.74 – 1.67 (br, 4H), 1.60 – 1.53 (br, 4H)

^{13}C NMR ($CDCl_3$, 151 MHz): δ 163.5 (d), 53.7 (d), 47.7, 38.8, 38.1, 29.3 (d), 27.8, 24.4 (d), 22.3 (d)

3.4.5.3 *trans*-[Pd(DBN)$_2$Cl$_2$]

The amidine, DBN (33 µl, 0.267 mmol), was added to the specified [Pd(PhCN)$_2$Cl$_2$] solution (50.4 mg, 0.131 mmol) to yield the product [Pd(DBN)$_2$Cl$_2$].

Yield: 40.3 mg, 72.0 %

IR (cm^{-1}): $\bar{\nu}_{(C=N)}$ = 1651

^{1}H NMR (CDCl$_3$, 600 MHz): δ 3.42 – 3.28 (m, 12H), 3.14 (t, 4H), 2.07 – 1.99 (m, 4H), 1.87 – 1.78 (m, 4H)

^{13}C NMR (CDCl$_3$, 151 MHz): δ 162.8, 52.7, 46.5, 42.2, 31.2, 21.1, 19.1

3.4.5.4 *trans*-[Pd(TMG)$_2$Cl$_2$]

The guanidine, TMG (33 µl, 0.263 mmol), was added to the specified [Pd(PhCN)$_2$Cl$_2$] solution (49.5 mg, 0.129 mmol) to yield the product [Pd(TMG)$_2$Cl$_2$]

Yield: 35.6 mg, 66.9 %

IR (cm^{-1}): $\bar{\nu}_{(C=N)}$ = 1566, 1536

^{1}H NMR (CDCl$_3$, 600 MHz): δ 3.41 – 3.13 (br, 12H), 2.86 – 2.65 (br, 12H)

^{13}C NMR (CDCl$_3$, 151 MHz): δ 168.8, 41.7 – 39.9, 39.4 – 38.3

3.4.5.5 *trans*-[Pd(TBD)$_2$Cl$_2$]

The guanidine, TBD (36.9 mg, 0.265 mmol), was added to the specified [Pd(PhCN)$_2$Cl$_2$] solution (50.1 mg, 0.131 mmol) to yield the product [Pd(TBD)$_2$Cl$_2$]

Yield: 31.8 mg, 53.4 %

IR (cm^{-1}): $\bar{\nu}_{(C=N)}$ = 1614

^{1}H NMR (CDCl$_3$, 600 MHz): δ 3.41 – 3.37 (br, 8H), 3.35 (t, 8H), 2.07 – 2.02 (m, 8H)

^{13}C NMR (CDCl$_3$, 151 MHz): δ 151.5, 46.9, 38.0, 20.7

3.4.6 Discussion

The preliminary solution study on the ability of the four bases/ ligands to coordinate to CO_2 aided in illustrating their relative coordinating strengths (TBD > DBU > DBN > TMG). Their strengths cannot be explained by only their pK_a and nucleophilicity (N) values (Table 2.3) because DBN has a larger nucleophilicity than DBU yet has a weaker binding ability to CO_2, even though the trend indicates that the larger the pK_a and/or N becomes, so does the coordinating ability improve. This may indicate that the steric influence from DBN is more restricting than DBU because of the smaller size of the cyclic ring in the former leading to a relatively linear structure when compared to the possible chair conformation in the larger cyclic ring of DBU. Also, the unambiguously large binding ability of TBD is further explained by the proton present on the β-nitrogen being able to stabilize the zwitterionic complex TBD-CO_2 as well as lead to the bicarbonate product [TBDH][HCO_3]. This is evident in the various peak formations and shifts noted in Fig. 3.5.

Three of the ligands (L = DBU, DBN and TMG) were successfully coordinated to the [Rh(COD)(L)Cl] complex with the novel synthesis of [Rh(COD)(TMG)Cl]. While the crystals of all three were collected, only the Rh(I) complexes containing DBU and TMG were analysed (SC-XRD) for comparative reasons between the amidines and guanidines and will be presented in Chapter 4. Attempts to synthesis the TBD-containing complex were unsuccessful, with the methods leading to an oil containing a decomposed product. The solvents were varied (dioxane, toluene, benzene) and attempts to precipitate or recrystallize the product (hexane, pentane, DCM, acetone) were unsuccessful. The ^{1}H NMR spectra consisted of multiple peaks that could not be identified where the ^{13}C NMR and IR confirmed the presence of coordinated TBD amongst other peaks. The possible reasons for the unsuccessful synthesis can be attributed to the properties of TBD mentioned in Par. 3.4.2. The high pK_a value of TBD may have resulted in it deprotonating the cyclooctadiene or that the hydrogen on the β-nitrogen may have some steric influence. Another possibility is that TBD coordinates *via* the two nitrogens (bidentate) but steric influence from the chlorido and COD may restrict the bond formation.

All four of the *trans*-[Pd(L)$_2$Cl$_2$] complexes (L = DBU, DBN, TMG, TBD) were successfully synthesized, with the latter three being novel compounds. The complexes were recrystallized in DMF which led to the former three complexes forming crystals and the *trans*-[Pd(TBD)$_2$Cl$_2$] complex decomposing to an oil. The recrystallized products contained both precipitate and small

crystals but only the DBN and TMG-containing complexes had crystals of sufficient size to perform SC-XRD analysis. The small yellow cuboidal crystals of the *trans*-[$Pd(DBN)_2Cl_2$] complex was successfully collected and will be discussed in Chapter 5. The SC-XRD analysis of the small orange needle-like crystals of the *trans*-[$Pd(TMG)_2Cl_2$] complex yielded a strong diffraction pattern but was highly disordered and could not be solved effectively. The NMR and IR spectra confirmed the presence of the complex which meant that it was possibly due to severe disorders in the crystals. The *trans*-[$Pd(TBD)_2Cl_2$] complex showed low yields and contained small impurities. When the product was washed excessively with toluene the yields were reduced even further because the product was sparingly soluble therein and attempts to remove the impurities by recrystallization led to decomposition of the product.

Further comparisons are made on the crystal structures synthesized in Par. 3.4.4.1, 3.4.4.3 and 3.4.5.3 in Chapter 4, followed by a kinetic study between [Rh(COD)(DBU)Cl] and [Rh(COD)(TMG)Cl] with DMAP in Chapter 5.

3.5 References

[1] R. M. Silverstein, F. Webster, & D. J. Kiemle, "Spectrometric Identification of Organic Compounds 7th ed", *John Wiley & Sons, Ltd*, (1963)

[2] K. Nakamoto, "Infrared and Raman Spectra of Inorganic and Coordination Compounds", *in Handbook of Vibrational Spectroscopy* (ed. Griffiths, P. R.) **25,** 233–238 *John Wiley & Sons, Ltd*, (2006)

[3] R. S. Macomber, & G. S. Harbison, "A complete introduction to modern NMR spectroscopy", *John Wiley & Sons, Ltd*, (1998)

[4] G. S. Pavia, D.L., Lampman G.M., Kriz, "Introduction to Spectroscopy", *USA: Thomson Learning Inc.*, (2001)

[5] J. R.B, "Reaction Mechanisms of Inorganic and Organometallic Systems", *Oxford: Oxford University Press, Inc.*, (1991)

[6] J. W. Moore, & R. G. Pearson, "Kinetics and Mechanism", *John Wiley & Sons, Ltd*, (1981)

[7] Q. Q. Pan, P. Guo, J. Duan, Q. Cheng, & H. Li, "Comparative crystal structure determination of griseofulvin: Powder X-ray diffraction versus single-crystal X-ray diffraction", *Chinese Sci. Bull.*, **57,** 3867–3871 (2012).

[8] W. Massa, "Crystal Structure Determination", *Springer Berlin Heidelberg*, (2004)

[9] Y. Waseda, E. Matsubara, & K. Shinoda, "X-Ray Diffraction Crystallography", *Springer Berlin Heidelberg*, (2011)

[10] C. Villiers, J. P. Dognon, R. Pollet, P. Thuéry, & M. Ephritikhine, "An isolated CO2 adduct of a nitrogen base: Crystal and electronic structures", *Angew. Chemie - Int. Ed.*, **49,** 3465–3468 (2010).

[11] R. Nicholls, S. Kaufhold, & B. N. Nguyen, "Observation of guanidine-carbon dioxide complexation in solution and its role in the reaction of carbon dioxide and propargylamines", *Catal. Sci. Technol.*, **4,** 3458–3462 (2014).

[12] D. J. Heldebrant, P. G. Jessop, C. A. Thomas, C. A. Eckert, & C. L. Liotta, "The Reaction of 1,8-Diazabicyclo[5.4.0]undec-7-ene (DBU) with Carbon Dioxide", *J. Org. Chem.*, **70,** 5335–5338 (2005).

[13] U. Flörke, U. Ortmann, & H. -J Haupt, "Rhodium(I)-cyclooctadiene (cod) complexes with the N-donor ligands 1,8-diazabicyclo[5.4.0]undec-7-ene (dbu) and 1,5-diazabicyclo[4.3.0]non-5-ene (dbn)", *Acta Crystallogr. Sect. C*, **48,** 1663–1665 (1992).

[14] V. De La Fuente, C. Godard, E. Zangrando, C. Claver, & S. Castillón, "A phosphine-free Pd catalyst for the selective double carbonylation of aryl iodides", *Chem. Commun.*, **48,** 1695–1697 (2012).

[15] G. K. Anderson, & M. Lin, "Bis(benzonitrile)dichloro Complexes of Palladium and Platinum", *Inorg. Synth.*, **28,** 60–63 (1990).

4 Single crystal X-ray diffraction study of amidine and guanidine containing metal complexes

What to expect

A detailed crystallographic evaluation of three complexes containing the ligands DBN, DBU and TMG, respectively, will be presented in this chapter.

4.1 Introduction

A thorough search of metal complexes containing the amidines and guanidines as a monodentate ligand, discussed in Chapter 2, was conducted on the Cambridge Structural Database (CSD) [1,2]. The number of crystals that were collected on the Database that contained the four bases (DBU, DBN, TMG and TBD) as ligands were a fraction of the complexes that contained similar bases such as DMAP and DABCO. Of the crystal structures found on the Database, no complexes were reported where the effects of the amidines and guanidines, as coordinating ligands, were structurally compared to each other, with respect to the same metal complex.

For this study two applicable crystal systems were identified; *trans*-[$Pd(DBU)_2I_2$] and [Rh(COD)(DBU)Cl], based on their potential application as catalysts for CO_2-fixation and for their varying ligand systems and geometrical orientation about the metal centre. The former complex was the structure collected after the reaction of the starting catalyst model *trans*-[$Pd(DBU)_2Cl_2$] with 1-iodo-*p*-methoxybenzene, which resulted in the substitution of the chlorido ligands. The initial chlorido containing model catalyst could not be crystallized and was subsequently only characterised by ^{1}H and ^{13}C NMR spectroscopy [3].

The latter complex, [Rh(COD)(DBU)Cl], was further chosen due to the presence of the COD ligand, which structurally "mimics" the behaviour of the Venus fly-trap (*Dionaea muscipula*) [4]; specifically relating to the so-called "*jaw*" movement of the ligand structure. Through the observation of the cyclooctadiene in a 3D diagram (Fig. 4.1(a)), it becomes easier to visualize how the COD configuration mimics the leaf structure of the plant. Ironically, in some petrochemical processes, diolefins act as a catalyst trapping agent/ inhibitor [5].

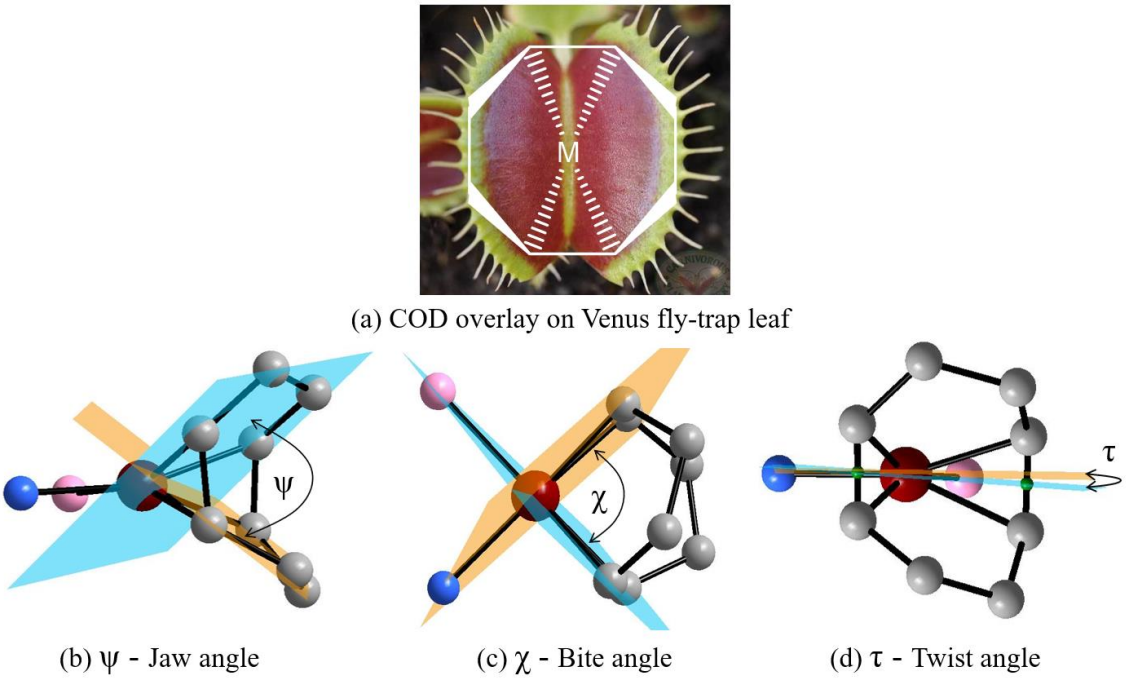

(a) COD overlay on Venus fly-trap leaf

(b) ψ - Jaw angle (c) χ - Bite angle (d) τ - Twist angle

Figure 4.1: (a) The structural overlay of COD, coordinated to a metal centre, onto a Venus fly-trap leaf. The definitions of the three angles that describe the geometry of the cyclooctadiene ligand in relation to the Venus fly-trap conformation: (b) ψ – Jaw: dihedral angle between the two planes through the four alkane carbon fragments, (c) χ – dihedral angle between the two planes through the two alkene moiety-metal atoms, and (d) τ – dihedral angle between the plane through the metal and mid-points (green dummy atoms) of the alkene carbons and the plane through the metal and the two *trans* ligands.

There are three parameters that can be used to describe the behaviour the cyclooctadiene as a model to the leaf of the Venus fly-trap: the so-called *jaw* angle (ψ) (Fig. 4.1(b)), the *bite* angle (χ) (Fig. 4.1 (c)) and the *twist* angle (τ) (Fig. 4.1(d)) – with the definitions noted in the Fig. 4.1 caption. These parameters help to evaluate the influence of the electronic and steric effects that the *trans* ligands have on the structural behaviour of the COD ligand when it is coordinated to a square planar transition metal complex [5,6]. Hill *et al.* (2018), found that when investigating these three

parameters of similar compounds; ψ and τ varied the most (*ca.* 10°), with χ staying relatively constant (*ca.* 1° variation) when the metal complexes of the type [M(COD)(*N*,*O*-Bid)]A (M = Pt^{II}, Pd^{II}) with various bidentate and counterions were structurally analysed [5].

With the above in mind, one of the initial major aims of this project was to crystallographically compare the effect of four superbases (L = DBU, DBN, TMG and TBD) using metal complexes of the type *trans*-[$Pd(L)_2Cl_2$] and [Rh(COD)(L)Cl], which were synthesised as described in Par 3.4.5 and 3.4.4 respectively [3,7]. Moreover, since these superbases in principle can capture/ trap carbon dioxide, the PGM complexes and structures thereof were identified wherein eventually the synergistic effect of the superbases, in combination with an available metal centre, whereupon the carbon dioxide can be activated. Thus, the synthetic protocol mentioned in Chapter 3 was developed to obtain appropriate metal complexes.

However, synthetic endeavour only led to the crystallisation and collection of *trans*-[$Pd(DBN)_2Cl_2$] (Fig. 4.2 (a)), [Rh(COD)(DBU)Cl] (Fig. 4.2 (b)) and [Rh(COD)(TMG)Cl] (Fig. 4.2 (c)), where the first and last complexes are novel crystal structures that have been obtained for the first time, and have been studied structurally. The aforementioned complexes are described in this chapter with a primary focus on crystal packing modes, molecular interactions and Venus Fly-trap parameters (for the latter two complexes), followed by a discussion on the significant aspects of each of the structures.

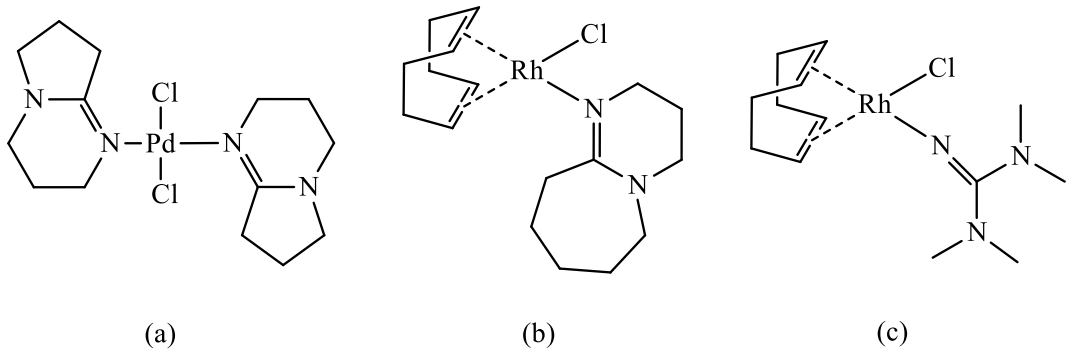

(a) (b) (c)

Figure 4.2: Schematic illustration of the three complexes isolated for single-crystal XRD study; (a) *trans*-[$Pd(DBN)_2Cl_2$], (b) [Rh(COD)(DBU)Cl] and (c) [Rh(COD)(TMG)Cl].

The complete lists of the crystallographic parameters of the structures presented in this chapter are given in the appendix as supplementary data.

4.2 Experimental

The diffraction data for the three complexes; *trans*-[$Pd(DBN)_2Cl_2$], [Rh(COD)(DBU)Cl] and [Rh(COD)(TMG)Cl] were collected at 100 K on a Bruker X8 Apex II 4K diffractometer, using monochromatic Mo Kα radiation with a wavelength of λ = 0.71073 Å. The cell parameters were all refined using the XREP4 and SAINT-Plus [8] programs, while SADABS [9] and multi-scan techniques were used for the absorption corrections. The structures were solved using direct methods in SIR97 [10] or SHELX, and refined (F^2), within SHELX-97 [11,12] and WinGX [13], respectively, using anisotropic displacement parameters for all non-hydrogen atoms. The DIAMOND [14] program was used to illustrate the molecular graphics, while Mercury [15] was used for structural overlays. Methyl, methylene and methine hydrogen atoms were placed in geometrically idealized positions (C-H = 0.95 – 0.98 Å) and constrained to their parent atoms with $U_{iso}(H) = 1.2U_{eq}(C)$ and $U_{iso}(H) = 1.5U_{eq}(C)$ respectively.

A summary of the general crystal data and refinement parameters for all three crystal structures, are shown in Table 4.1. The complete list of the bond distances, bond angles, atomic coordinates, hydrogen coordinates, torsion angles and anisotropic displacement parameters of the complexes are found in the appendix as supplementary data. The most important bond parameters are shown under each subsequent crystal structure. The hydrogen atoms and numbering for certain carbon atoms were omitted for clarity on some molecular structures.

Table 4.1: The general X-ray crystal data and refinement parameters of *trans*-[Pd(DBN)$_2$Cl$_2$], [Rh(COD)(DBU)Cl] and [Rh(COD)(TMG)Cl].

Crystallographic data	*trans*-[Pd(DBN)$_2$Cl$_2$]	[Rh(COD)(DBU)Cl]	[Rh(COD)(TMG)Cl]
Empirical formula	$C_{14}H_{24}Cl_2N_4Pd$	$C_{17}H_{28}ClN_2Rh$	$C_{13}H_{24}ClN_3Rh$
Formula weight (gmol^{-1})	425.67	398.77	360.71
Temperature (K)	100(2)	100(2)	100(2)
Crystal system	Monoclinic	Monoclinic	Orthorhombic
Space group	$P2_1/c$	$P2_1/c$	*Pbca*
Unit cell dimensions			
a (Å)	7.2350(3)	13.144(4)	13.3640(9)
b (Å)	9.2490(4)	11.056(4)	10.8000(11)
c (Å)	13.1880(5)	20.496(4)	21.6730(19)
α (°)	90	90	90
β (°)	99.9200(10)	35.712(10)	90
γ (°)	90	90	90
Volume (Å^3)	869.30(6)	1738.6(9)	3128.1(5)
Z	2	4	8
Density (g cm^{-3})	1.626	1.523	1.532
Crystal colour	Yellow	Yellow	Yellow
Crystal morphology	Cuboid	Cuboid	Cuboid
Crystal size (mm^3)	0.200 x 0.130 x 0.063	0.370 x 0.176 x 0.104	0.280 x 0.189 x 0.087
μ (mm^{-1})	1.374	1.132	1.251
F(000)	432	824	1480
θ range (°)	3.61 – 28.00	3.72 – 28.00	4.05 – 28.00
Index ranges	$-9 \le h \le 9$ $-7 \le k \le 12$ $-17 \le l \le 17$	$-17 \le h \le 15$ $-14 \le k \le 14$ $-27 \le l \le 27$	$-16 \le h \le 17$ $-11 \le k \le 14$ $-28 \le l \le 28$
Reflections collected	13532	30961	48900
Unique reflections	2098	4186	3766
R_{int}	0.0277	0.0266	0.0571
Completeness to theta (°, %)	25.24, 99.5	25.24, 99.7	25.24, 99.6
Data / restraints / parameters	2098 / 185 / 115	4186 / 0 / 190	3766 / 48 / 167
Goodness-of-fit on F^2	1.074	1.088	1.038
R [$I > 2\sigma(I)$]	$R_1 = 0.0512$ $wR_2 = 0.1390$	$R_1 = 0.0235$ $wR_2 = 0.0585$	$R_1 = 0.0471$ $wR_2 = 0.1062$
R (all data)	$R_1 = 0.0681$ $wR_2 = 0.1613$	$R_1 = 0.0282$ $wR_2 = 0.0623$	$R_1 = 0.0747$ $wR_2 = 0.1251$
ρ_{max}, ρ_{min} (e.Å^{-3})	1.076, -0.891	0.575, -0.504	0.875, -1.038

4.3 *trans*-[Pd(DBN)$_2$Cl$_2$]

The title compound, *trans*-[Pd(DBN)$_2$Cl$_2$], was synthesized as described in Par. 3.4.5.3, with the complex crystallizing in the monoclinic crystal system, in the space $P2_1/c$ group, with two formula units in the unit-cell (Z = 2), with no significant hydrogen bonding interactions. The molecular structure of the complex (Fig. 4.3) shows the atomic numbering and hydrogens. Selected bond lengths and angles are shown in Table 4.2, and Table 4.3 contains the torsion and dihedral angles. The crystal structure of trans-[Pd(DBN)$_2$Cl$_2$] has two *trans* neutral DBN ligands, with an envelope conformation, and two *trans* anionic chlorido ligands coordinated to the palladium (II) centre. The Pd(II) centre sits on a special position (0, 0, 0) located on an inversion centre which requires the molecule to be centrosymmetric. The structure displays a positional disorder on the N_1/N_{01} and C_1/C_{01} atoms with an occupancy of 85/15% and 75/25% respectively, due to the flipping of the DBN ligands (indicated by the dashed lines of N_{01} and C_{01}). The rest of the DBN ligand was restricted with the appropriate SHELX compatible restraints (RIGU, SIMU and DELU), leading to the large number of restraints reported in Table 4.1. The high electron peak density is located 0.03 Å from C_{01} and may be attributed to the flipping of the ligand.

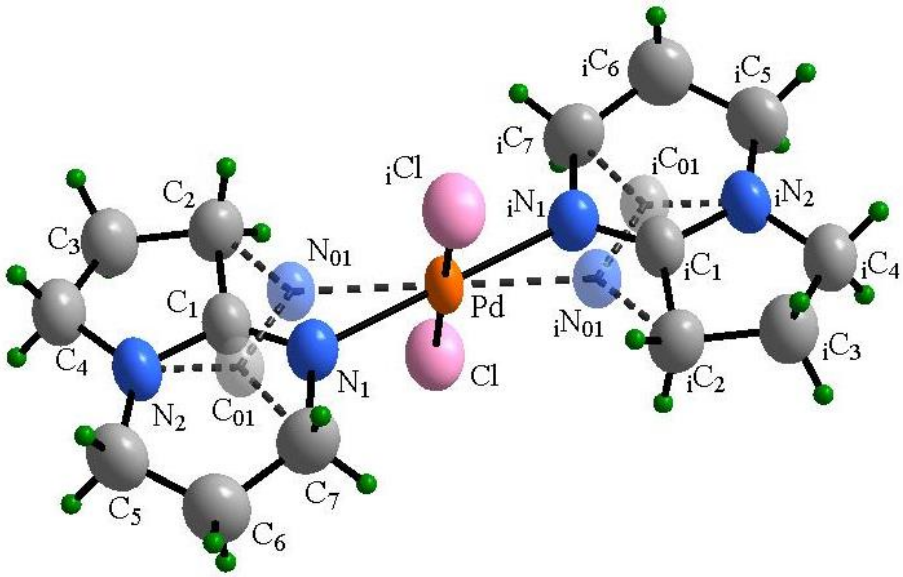

Figure 4.3: Molecular representation of the disordered *trans*-[Pd(DBN)$_2$Cl$_2$] complex, with the hydrogens (green atoms). The displacement ellipsoids are all drawn at 50% probability level, with the hydrogen atom sizes being reduced for clarity. The positional disorder on the N_1/N_{01} and C_1/C_{01} atoms (with an occupancy of 85/15% and 75/25% respectively) are indicated with a zero before the atom number, their bonds are depicted with dashed lines and the symmetry generated atoms are indicated by a subscript *i* in front of the atom symbol. The Pd(II) is located on an inversion centre, with the equivalent atoms generated using the symmetry transformation: -x, -y, -z.

Table 4.2: Selected bond lengths and bond angles for the principal fraction of the title complex, *trans*-[Pd(DBN)$_2$Cl$_2$].

Atoms	Bond length (Å)	Atoms	Bond angle (°)
C_1-N_1	1.26(1)	N_1-C_1-N_2	125.5(8)
C_1-N_2	1.346(8)	N_2-C_1-C_2	113.7(6)
C_1-C_2	1.55(1)	N_1-C_1-C_2	120.7(7)
C_7-N_1	1.484(9)	C_1-N_1-Pd	124.1(6)
Pd-N_1	2.021(7)	N_1-Pd-Cl	93.0(2)
Pd-Cl	2.301(2)	N_1-Pd-$_i$Cl	87.0(2)

Symmetry transformations used to generate equivalent atoms: -x,-y,-z. (see appendix)

Table 4.3: Selected torsion and dihedral angles for the principal fraction of the title complex, *trans*-[Pd(DBN)$_2$Cl$_2$].

Atoms	Torsion[a] /Dihedral[b] angle (°)	Atoms	Dihedral angle (°)
Pd-N_1-C_1-N_2	176.2(6)[a]	$\mathbf{P}_{C2}$-$\mathbf{P}_{N1}$	29.2(8)
Cl-Pd-N_1-C_1	-72.5(7)[a]	$\mathbf{P}_{C2}$-$\mathbf{P}_{N2}$	31.5(8)
$\mathbf{P}_{C1}$-$\mathbf{P}_{N1}$	83.5(3)[b]	$\mathbf{P}_{C2}$-$\mathbf{P}_{N3}$	27.1(8)
$\mathbf{P}_{C1}$-$\mathbf{P}_{N2}$	84.7(3)[b]	$\mathbf{P}_{N2}$-$\mathbf{P}_{N3}$	6.1(3)
$\mathbf{P}_{C1}$-$\mathbf{P}_{N3}$	81.5(3)[b]		

Symmetry transformations used to generate equivalent atoms: -x,-y,-z (see appendix)

Planes indicated with the "**P**" symbol: $\mathbf{P}_{C1}$(Cl-Pd-$_i$Cl), $\mathbf{P}_{C2}$(N_1-Pd-$_i$$N_1$), $\mathbf{P}_{N1}$(DBN), $\mathbf{P}_{N2}$(6-membered DBN ring), $\mathbf{P}_{N3}$(5-membered DBN ring)

The selected bond lengths and angles, from Table 4.2, of the title complex were compared to that found in literature for [Pd(DBU)$_2$I$_2$], first synthesized by De La Fuente *et al.* [3]. It was noted that both have the same crystal system, space group and inversion centre, which were located on the position of the metal centre. Additionally, the literature complex [Pd(DBU)$_2$I$_2$], was collected at 293(2) K and not at 100(2) K as the reported structure was. Interestingly, no positional disorder was noted in the literature complex, that may account for the flipping of the DBU ligands. The Pd-N_1 and Pd-I bond lengths in [Pd(DBU)$_2$I$_2$] were 2.004(9) and 2.607(1) Å respectively, which showed that the DBU is more strongly coordinated than the title complex (even though it is less nucleophilic than DBN), with the larger steric hindrance of the DBU being subdued by the longer anionic bond length. Yet this observation may be discounted because of the complexes' data were collected at different temperatures. The corresponding C_1-$N_{1/2}$ and N_1-C_7 bond lengths are all shorter (0.0052, 0.0028 and 0.0024 Å respectively) in the title complex, while the N_1-Pd-I bond

angle = (90.7°(3)) is 2.3° smaller than in the title complex, possibly due to the short Pd-Cl bond length and subsequent steric interference, which leads to *trans*-[Pd(DBN)$_2$Cl$_2$] being less planar. The degree of planarity of the complex and of the two rings (5 and 6 membered) of the coordinated DBN ligand is shown in Fig. 4.4, with the dihedral angles between them noted in Table 4.3. The values show that the complex is not planar with respect to the DBN ligand but distorted by *ca.* -7.5° and 29° for the $\mathbf{P}_{C1}$ (Cl-Pd-$_i$Cl) plane and $\mathbf{P}_{C2}$ (N$_1$-Pd-$_i$N$_1$) plane with respect to the $\mathbf{P}_{N1}$ (average DBN) plane, respectively, with the bent conformation of the DBN about N$_1$ accounting for the values. Whereas the planes through the two DBN rings (6 membered-ring ($\mathbf{P}_{N2}$) and 5 membered-ring ($\mathbf{P}_{N3}$)) have a dihedral angle of 6.1(3)°, which shows the two rings are bent with respect to each other.

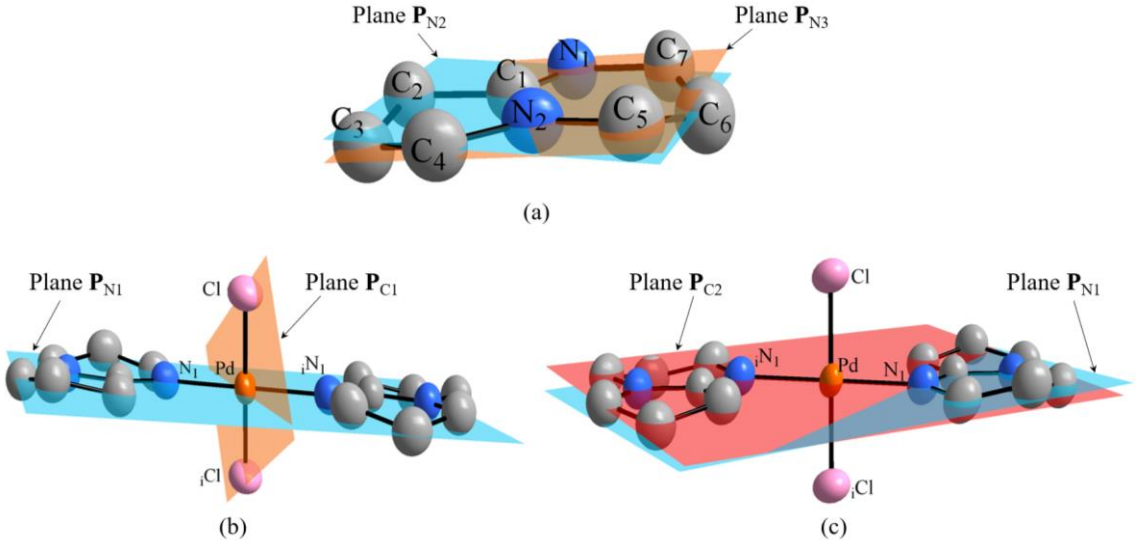

Figure 4.4: Illustration of the planes in *trans*-[Pd(DBN)$_2$Cl$_2$]. (a) Two planes of the DBN molecule; the 6 membered-ring ($\mathbf{P}_{N2}$, blue) and 5 membered-rings ($\mathbf{P}_{N3}$, orange). (b) Two perpendicular planes within the complex; the average DBN ($\mathbf{P}_{N1}$, blue) and Cl-Pd-$_i$Cl ($\mathbf{P}_{C1}$, orange). (c) Two parallel planes; the average DBN ($\mathbf{P}_{N1}$, blue) and N-Pd-$_i$N ($\mathbf{P}_{C2}$, red). Hydrogen atoms and certain atom names are omitted for clarity.

The packing of the title complex in the unit cell is illustrated in Fig. 4.5. The moieties are located at the corners and in the centre of two of the six unit-cell faces in an overarching head-to-tail packing mode.

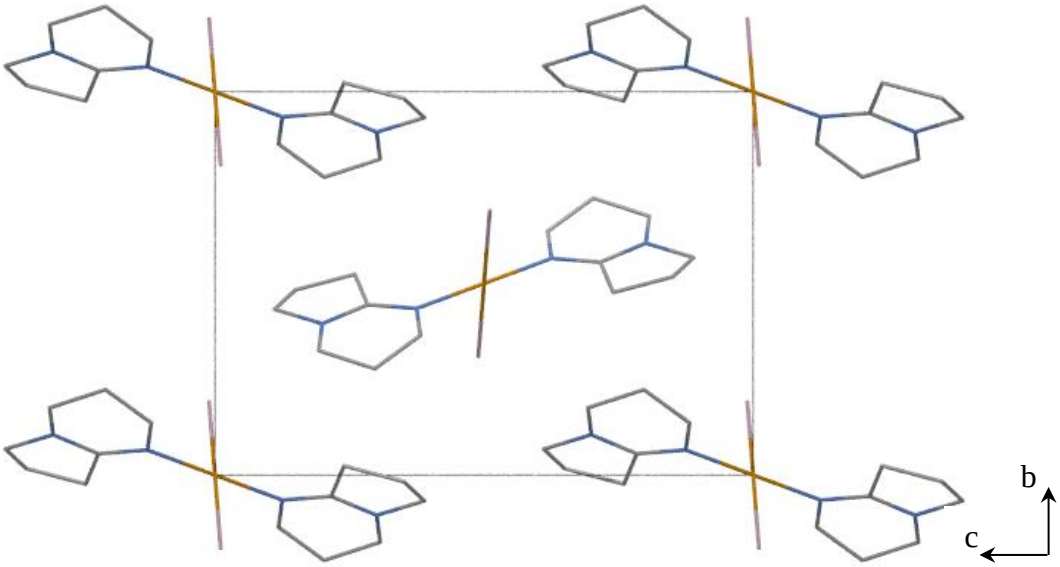

(a) Viewed along the *a*- axis.

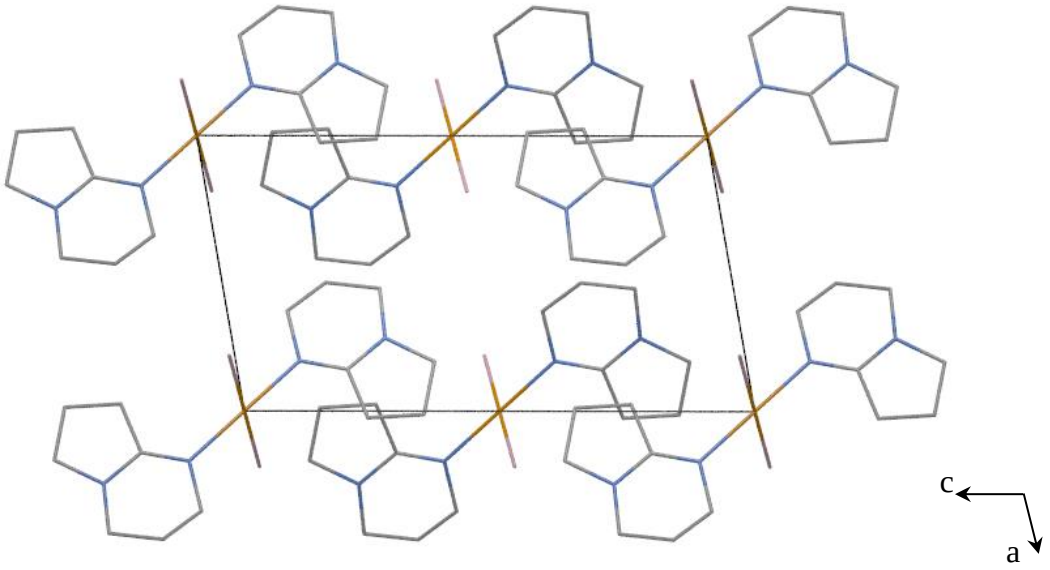

(b) Viewed along the *b*- axis.

Figure 4.5: Crystal packing of the $[Pd(DBN)_2Cl_2]$complex in the unit cell; (a) viewed along the *a*- axis and (b) viewed along the *b*- axis.

4.4 [Rh(COD)(DBU)Cl]

The [Rh(COD)(DBU)Cl] complex was synthesized as described in Par. 3.4.4.1. The complex crystallizes in the monoclinic crystal system in the $P2_1/c$ space group, and has four formula units in the unit cell (Z = 4), with no significant hydrogen bonding interactions. The molecular structure of the complex is illustrated in Fig. 4.6, with atomic numbering and hydrogen atoms included. Selected bond lengths and angles are displayed in Table 4.4 and Table 4.5 containing relevant torsion and dihedral angles.

The crystal structure, [Rh(COD)(DBU)Cl], has two neutral ligands (DBU and COD) and one chlorido ligand coordinated to the rhodium(I) metal centre, with the DBU and chlorido *trans* to the cyclooctadiene – which coordinates through its olefinic bonds. The DBU ligand shows two types of conformations, chair (7-membered ring) and envelope (6-membered ring) on the cyclic rings, where the COD displays a boat conformation, see Fig. 4.6. The structure showed no statistical disorders and required no restraints.

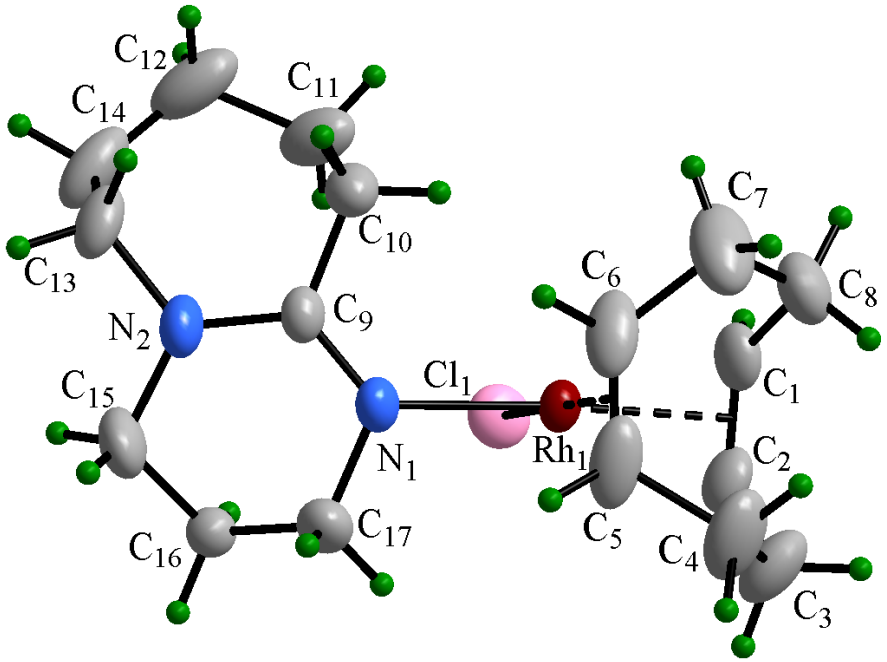

Figure 4.6: Molecular representation of the [Rh(COD)(DBU)Cl] complex, with hydrogens (green atoms). The displacement ellipsoids are all drawn at 50% probability level, with the hydrogen atom sizes reduced for clarity. The dashed lines indicate the olefinic bonding interaction to the Rh(I) metal centre.

Table 4.4: Selected bond lengths and bond angles for the title complex, [Rh(COD)(DBU)Cl].

Atoms	Bond length (Å)	Atoms	Bond angle (°)
Rh-X_1	2.015(6)	X_1-Rh-Cl	91.74(2)
Rh-C_1	2.136(2)	X_1-Rh-N_1	176.47(5)
Rh-C_2	2.126(2)	X_1-Rh-X_2	88.31(2)
Rh-X_2	1.978(5)	X_2-Rh-Cl	179.66(3)
Rh-C_5	2.099(2)	X_2-Rh-N_1	91.52(6)
Rh-C_6	2.096(2)	N_1-C_9-N_2	123.8(2)
C_9-N_1	1.296(2)	N_1-C_9-C_{10}	119.1(2)
C_9-N_2	1.354(2)	N_2-C_9-C_{10}	117.2(2)
C_9-C_{10}	1.501(3)	C_9-N_1-Rh	128.3(1)
C_{17}-N_1	1.464(3)	N_1-Rh-Cl	88.40(5)
Rh-Cl	2.3776(7)		
Rh-N_1	2.107(2)		

X_1 (C_1-C_2 midpoint), X_2 (C_5-C_6 midpoint)

Table 4.5: Selected torsion and dihedral angles for the title complex, [Rh(COD)(DBU)Cl].

Atoms	Torsion angle (°)	Atoms	Dihedral angle (°)
C_8-C_1-C_2-C_3	3.3(3)	$\mathbf{P}_{X1}$-$\mathbf{P}_{D1}$	21.8(2)
C_4-C_5-C_6-C_7	4.1(4)	$\mathbf{P}_{X1}$-$\mathbf{P}_{D2}$	17.7(1)
C_2-C_3-C_4-C_5	27.3(4)	$\mathbf{P}_{X1}$-$\mathbf{P}_{D3}$	37.9(2)
C_6-C_7-C_8-C_1	28.0(4)	$\mathbf{P}_{X2}$-$\mathbf{P}_{D1}$	74.6(1)
Rh-N_1-C_9-N_2	167.2(2)	$\mathbf{P}_{X2}$-$\mathbf{P}_{D2}$	70.8(1)
Cl-Rh-N_1-C_9	80.5(2)	$\mathbf{P}_{X2}$-$\mathbf{P}_{D3}$	79.0(2)
		$\mathbf{P}_{D2}$-$\mathbf{P}_{D3}$	40.3(1)
		Bite angle (χ)[a]	87.9(2)
		Jaw angle (ψ)[a]	75.3(3)
		Twist angle (τ)[a]	3.5(5)

Planes: $\mathbf{P}_{X1}$(C_1-C_2-Rh-Cl), $\mathbf{P}_{X2}$(C_5-C_6-Rh-N_1), $\mathbf{P}_{D1}$(DBU), $\mathbf{P}_{D2}$(6-membered DBU ring), $\mathbf{P}_{D3}$(7-membered DBU ring).
a) See Fig. 4.1 for definitions and depictions.

The title complex was originally reported by Florke *et al.* (1992) but was collected at room temperature (296(1) K) and crystallized in the monoclinic $P2_1$ space group [7]. This is in contrast to the reported structure, which was collected at 100(2) K in the monoclinic $P2_1/c$ space group. The comparison of the reported and literature structures is provided in Table 4.6. The distance between the midpoints of the olefinic atoms ($X_1 = C_1$-C_2 and $X_2 = C_5$-C_6) and the Rh(I) centre of the title complex were seen to be shorter than those reported in 1992, while the bond length of the DBU to the metal centre equally longer (all the bond lengths varied by *ca.* 0.01 Å) but only by *ca.* 0.005 Å for the Rh-Cl bond. Consequently, the angles about the Rh(I) varied as well, with most of them fluctuating by less than approximately 0.7° with the noticeable exception being the angle between the *trans* ligands, which increased by *ca*. 1.2° and 1.8°, affording a near planar conformation. The recollected crystal structure as reported herein, 26 years later, afforded insight into the temperature influence on the molecular geometry, unreported bonds, angles, Venus fly-trap parameters, standard space group conformation and equipment capabilities.

The literature article [7] did not evaluate the Venus fly-trap parameters of the COD (this definition was only introduced within the last decade) [16], after which the file was obtained and the parameter values were determined (Table 4.6). Of these values, the *jaw* angle most notably increased by 6.9(3) ° with respect to the reported complex. The reason for this increase could not be given with certainty but the possibilities may be that the different space group symmetries may have an influence on the restriction of the cyclooctadiene or that the complex is affected by temperature.

Hill (2011) also characterized similar rhodium complexes with the structure [Rh(COD)(L)], L = bidentate ligands such as acetylacetone and tropolone [16]. Of the complexes synthesized by Hill, the tropolone containing complex [Rh(COD)(Trop)] had the smallest ψ angle of 73.7(1)° and χ angle of 88.02(7)°. Comparing these values to the title complex, they correlate well with the *bite* angle, but a larger *jaw* angle 75.3(3)° being noted. The torsion angles about the olefinic carbons are small with values of 3.3(3)° and 4.1(4)° but increase across the four carbon alkane fragments to values of 27.3(4)° and 28.0(4)°. The breach of planarity of the DBU ligand with respect to the $\mathbf{P}_{X1}$ (Fig. 4.7(b)) and $\mathbf{P}_{X2}$ (Fig. 4.7(c)) planes are 21.8(2)° and 74.6(1)° respectively, which shows that the DBU is orientated at an angle towards the chlorido ligand. The dihedral angle between the planes of the 6 ($\mathbf{P}_{D2}$) and 7 ($\mathbf{P}_{D3}$)-membered rings of the DBU ligand (Fig. 4.7(a)) is 40.3(1)°, with the 7-membered ring in a chair conformation towards the chlorido ligand.

Table 4.6: Comparison of the selected X-ray crystal data, refinement parameters, bond lengths and bond angles of [Rh(COD)(DBU)Cl] reported and from literature.[7]

	Reported	Literature	
Temperature (K)	100(2)	296(1)	
Crystal system	Monoclinic	Monoclinic	
Space group	$P2_1/c$	$P2_1$	
Volume (Å^3)	1738.6(9)	870.7	
Unit cell dimensions			
a (Å)	13.144(4)	7.398(1)	
b (Å)	11.056(4)	11.439(2)	
c (Å)	20.496(4)	10.727(2)	
α (°)	90	90	
β (°)	35.71(1)	106.42(1)	
γ (°)	90	90	
	wR_2 = 0.0585	wR_2 = 0.029	
ρ_{max}, ρ_{min} (e.Å^{-3})	0.575, -0.504	0.38, -0.43	
Atoms	Bond length (Å)		Difference
Rh-X1	2.015(6)	2.026(5)	-0.011(8)
Rh-X2	1.978(5)	1.989(5)	-0.011(7)
Rh-Cl	2.3776(7)	2.371(12)	0.0066(14)
Rh-N1	2.107(2)	2.097(3)	0.010(4)
Atoms	Bond angle (°)		Difference
X_1-Rh-Cl	91.74(2)	91.9(2)	-0.16(20)
X_1-Rh-N_1	176.47(5)	175.3(2)	1.17(20)
X_1-Rh-X_2	88.31(2)	88.2(2)	0.11(20)
X_2-Rh-Cl	179.66(3)	177.9(2)	1.76(20)
X_2-Rh-N_1	91.52(6)	92.2(2)	-0.68(20)
N_1-Rh-Cl	88.40(5)	87.9(1)	0.50(11)
	Dihedral angle (°)		
Bite angle (χ)[b]	87.9(2)	87.8(3)	0.1(4)
Jaw angle (ψ)[b]	75.3(3)	82.2(3)	-6.9(3)
Twist angle (τ)[b]	3.5(5)	5.3(8)	-1.8(9)

a) [I > 4σ(I)] for literature values
b) See Fig. 4.1 for definitions and depictions.

A fraction of the packing of the title complex in the unit cell is illustrated in Fig. 4.8, from which it can be seen that the [Rh(COD)(DBU)Cl] complex packs head-to-tail about the faces along the *c*-axis.

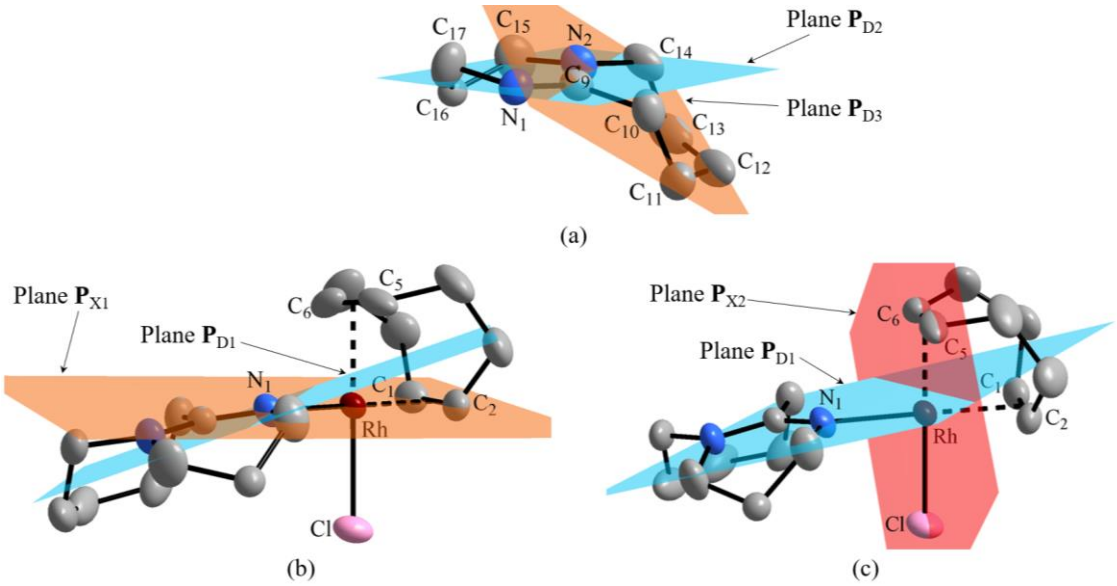

Figure 4.7: Illustration of the planes in [Rh(COD)(DBU)Cl]; (a) Two planes of the DBU molecule; the 6 membered-ring ($\mathbf{P}_{D2}$, blue) and 7 membered-ring ($\mathbf{P}_{D3}$, orange). (b) Two parallel planes within the complex; the average DBU ($\mathbf{P}_{D1}$, blue) and C_1-C_2-Rh-N_1 ($\mathbf{P}_{X1}$, orange). (c) Two perpendicular planes; the average DBU ($\mathbf{P}_{D1}$, blue) C_5-C_6-Rh-Cl ($\mathbf{P}_{X2}$, red). Hydrogen atoms and certain atom names are omitted for clarity.

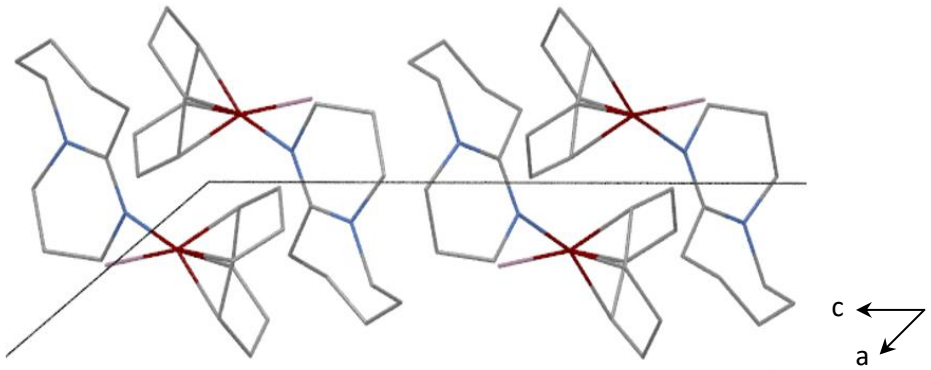

Figure 4.8: A fraction of the crystal packing of the [Rh(COD)(DBU)Cl] complex in the unit cell, viewed along the *b*-axis.

4.5 [Rh(COD)(TMG)Cl]

The [Rh(COD)(TMG)Cl] complex was synthesized as described in Par. 3.4.4.3. The complex crystallizes in the orthorhombic crystal system in the *Pbca* spacegroup, and has eight formula units in the unit cell (Z = 8) with two formal intramolecular hydrogen bond interactions. The molecular structure of the complex is illustrated in Fig. 4.9, with atomic numbering and hydrogen atoms included. Selected interatomic bond lengths and angles are listed in Table 4.7, while Table 4.8 gives selected torsion and dihedral angles.

The molecular structure of [Rh(COD)(TMG)Cl] has two neutral ligands (TMG and COD) and one chlorido ligand coordinated to the Rh(I), with the TMG and chlorido *trans* to the cyclooctadiene. The latter coordinates to the metal centre through the olefinic bonds (where the COD ligand was found to be in the usual boat conformation). The crystal structure displayed a statistical disorder on the COD ligand which was resolved with the relevant SHELX compatible restraints (RIGU), resulting in the number of restraints reported in Table 4.1. A low electron peak density (-1.038 e.Å^{-3}) was located 0.26 Å from the C_8 atom.

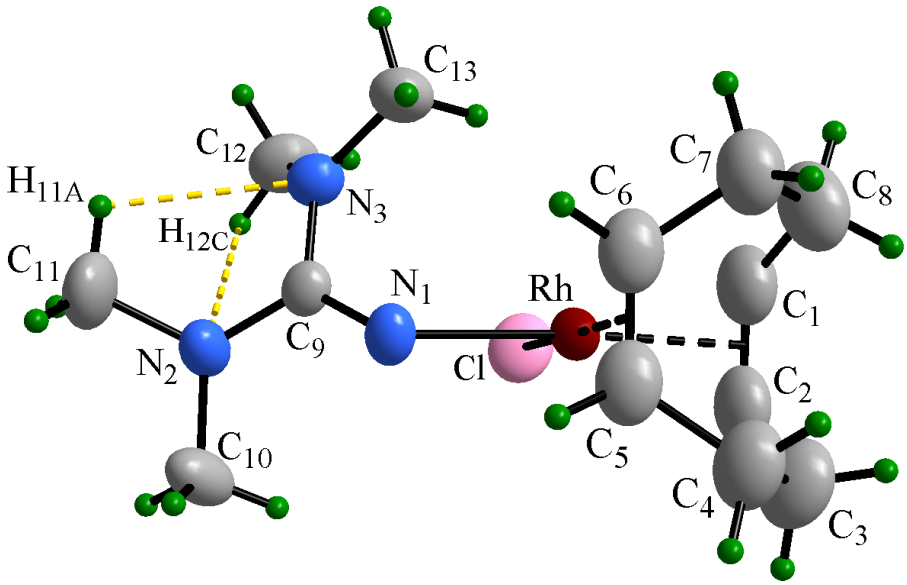

Figure 4.9: Molecular representation of the [Rh(COD)(TMG)Cl] complex, with hydrogens (green atoms). The displacement ellipsoids are all drawn at 50% probability level, with the hydrogen atom sizes being reduced for clarity. The black dashed lines indicate the olefinic bonding to the Rh(I) centre and the yellow dashed lines indicate the intramolecular bonding.

Table 4.7: Selected bond lengths and bond angles for the title complex, [Rh(COD)(TMG)Cl].

Atoms	Bond length (Å)	Atoms	Bond angle (°)
Rh-Y_1	1.992(5)	Y_1-Rh-Cl	91.6(4)
Rh-C_1	2.104(6)	Y_1-Rh-N_1	176.2(1)
Rh-C_2	2.110(6)	Y_1-Rh-Y_2	87.8(1)
Rh-Y_2	1.986(4)	Y_2-Rh-Cl	178.7(4)
Rh-C_5	2.100(6)	Y_2-Rh-N_1	92.5(1)
Rh-C_6	2.104(6)	N_1-C_9-N_2	122.4(5)
C_9-N_1	1.298(6)	N_1-C_9-N_3	122.3(4)
C_9-N_3	1.362(6)	N_3-C_9-N_2	115.3(4)
C_9-N_2	1.370(6)	C_9-N_1-Rh	128.4(3)
Rh-Cl	2.377(1)	N_1-Rh-Cl	88.2(1)
Rh-N_1	2.097(4)		

Y_1 (C_1-C_2 midpoint), Y_2 (C_5-C_6 midpoint)

Table 4.8: Selected torsion and dihedral angles for the title complex, [Rh(COD)(TMG)Cl].

Atoms	Torsion angle (°)	Atoms	Dihedral angle (°)
C_8-C_1-C_2-C_3	3(1)	$\mathbf{P}_{Y1}$-$\mathbf{P}_{T1}$	44.0(3)
C_4-C_5-C_6-C_7	3(1)	$\mathbf{P}_{Y1}$-$\mathbf{P}_{T2}$	17.2(2)
C_2-C_3-C_4-C_5	12(1)	$\mathbf{P}_{Y1}$-$\mathbf{P}_{T3}$	70.0(3)
C_6-C_7-C_8-C_1	14(1)	$\mathbf{P}_{Y2}$-$\mathbf{P}_{T1}$	50.6(2)
Rh-N_1-C_9-N_2	134.8(4)	$\mathbf{P}_{Y2}$-$\mathbf{P}_{T2}$	72.0(2)
Rh-N_1-C_9-N_3	-45.8(7)	$\mathbf{P}_{Y2}$-$\mathbf{P}_{T3}$	26.5(3)
Cl-Rh-N_1-C_9	34.8(4)	$\mathbf{P}_{T2}$-$\mathbf{P}_{T3}$	57.0(2)
		Bite angle (χ)[a]	87.7(2)
		Jaw angle (ψ)[a]	64.7(4)
		Twist angle (τ)[a]	4.0(9)

Planes: $\mathbf{P}_{Y1}$ (C_1-C_2-Rh-Cl), $\mathbf{P}_{Y2}$ (C_5-C_6-Rh-N_1), $\mathbf{P}_{T1}$ (TMG), $\mathbf{P}_{T2}$ (C_9-N_2-C_{10}-C_{11}), $\mathbf{P}_{T3}$ (C_9-N_3-C_{12}-C_{13})
a) See Fig. 4.1 for definitions

To stabilize the solid-state structure of [Rh(COD)(TMG)Cl], two intramolecular hydrogen bonds were observed on the TMG ligand (Table 4.9), one from each of the methyl groups by the hydrogen atom nearest to the nitrogen on the opposite imine appendage.

Table 4.9: Intramolecular hydrogen bonds observed on the [Rh(COD)(TMG)Cl] complex.

D-H···A	D-H (Å)	H···A (Å)	D···A (Å)	D-H···A (°)
C(11)-H(11A)···N(3)	0.96	2.47	2.855(8)	103.9
C(12)-H(12C) ···N(2)	0.96	2.45	2.855(7)	104.9

Symmetry transformation used to generate equivalent atoms: x, y, z.

The distance between both the midpoints of the olefinic bonds (Y_1 = C_1-C_2 and Y_2 = C_5-C_6) and the Rh(I) centre of the title complex were found to be similar (1.992(5) Å and 1.986(4) Å respectively), while the bond lengths of the Rh-Cl and Rh-N_1 to the metal centre were 2.3776(7) and 2.107(2) Å, respectively. The Venus fly-trap parameters of the COD were determined, with the ψ angle 64.7(4)° and the χ angle 87.7(2)°. The bite angle was comparable to the rhodium complexes (χ = 88.8(2)° – 88.0(2)°) that were synthesized by Hill (2011), which indicated minimal change with respect to the *trans* ligands. However, the jaw angle for [Rh(COD)(TMG)Cl] was significantly smaller than any of the jaw values (ψ = 76.4(3)° – 73.7(1)°) reported by Hill (2011) [16].

The torsion angles about the olefinic carbons were small with values of 3(1)° and 3(1)° but increase across the four carbon alkane fragments to values of 14(1)° and 12(1)° respectively. The large errors on these values were attributed to the restraints applied to the cyclooctadiene. The breach of structural planarity of the TMG ligand ($\mathbf{P}_{T1}$) with respect to the $\mathbf{P}_{Y1}$ (Fig. 4.10(b)) and $\mathbf{P}_{Y2}$ (Fig. 4.10(c)) planes was noted to be 44.0(3)° and 50.6(2)°, which showed that the TMG is orientated at an angle towards the chlorido ligand. The dihedral angle between the planes of the two appendages about C_9 of the TMG ligand (Fig. 4.10(a)) was 57.0(2)° with the one appendage orientated away ($\mathbf{P}_{T2}$) from the chlorido and the other towards ($\mathbf{P}_{T3}$).

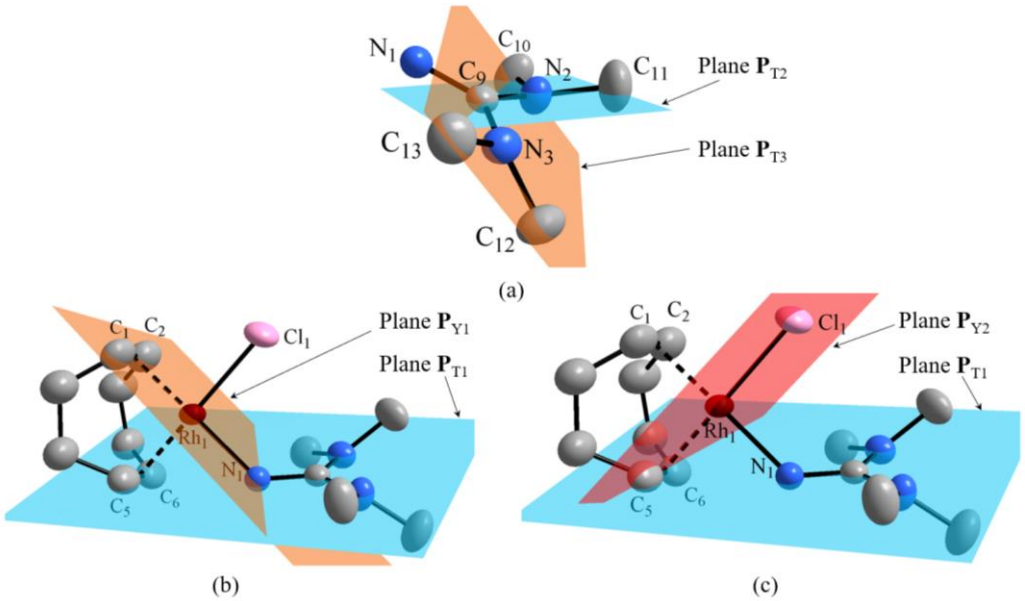

Figure 4.10: Illustration of the planes in [Rh(COD)(TMG)Cl]; (a) Two planes of the TMG molecule; the planes through C_9-N_2-C_{10}-C_{11} ($\mathbf{P}_{T2}$, blue) and C_9-N_3-C_{12}-C_{13} ($\mathbf{P}_{T3}$, orange). (b) Two parallel planes within the complex; the average TMG ($\mathbf{P}_{T1}$, blue) and C_1-C_2-Rh-N_1 ($\mathbf{P}_{Y1}$, orange). (c) Two perpendicular planes; the average DBU ($\mathbf{P}_{T1}$, blue) C_5-C_6-Rh-Cl ($\mathbf{P}_{Y2}$, red). Hydrogen atoms and certain atom names are omitted for clarity.

The packing of the title complex in the unit-cell is illustrated in Fig. 4.11, from which it is clear that the [Rh(COD)(TMG)Cl] complex packs head-to-head, tail-to-tail along the *a*-axis within the crystal lattice.

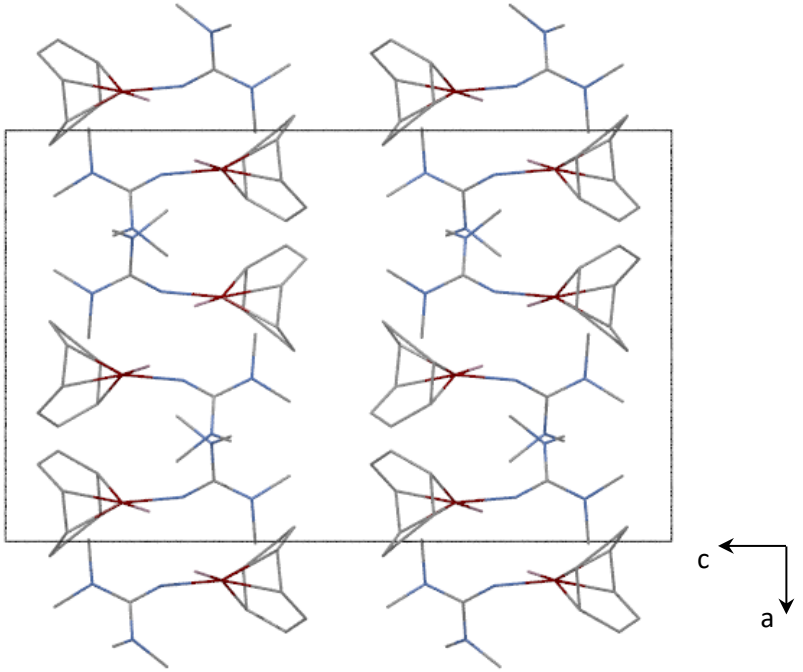

Figure 4.11: Crystal packing of [Rh(COD)(TMG)Cl] in the unit cell, viewed along the *b*-axis.

4.6 Discussion

The solid-state structures of two novel complexes (*trans*-[Pd(DBN)$_2$Cl$_2$] and [Rh(COD)(TMG)Cl]) as well as the recollected [Rh(COD)(DBU)Cl] complex were analysed, and the data compared by means of a single crystal X-ray diffraction study. From this investigation it was found that the latter two structures have the same basic chemical architecture, [Rh(COD)(X)Cl] with X = DBU and TMG, and only differing in the neutral ligand that is coordinated to the metal centre. Both DBU and TMG have the same core functional groups (amine and imine) but with TMG having an amine in place of a carbon about the C_9 atom (Fig. 4.12). The latter is also not as structurally rigid and sterically bulky as DBU and also has an additional resonance pathway about C_9, with a lone electron pair on N_1 – all of which can help elucidate the effects thereof on the bonding interactions. While *trans*-[Pd(DBN)$_2$Cl$_2$] may not be structurally similar to the two aforementioned complexes, the DBN ligand provides further insight into bonding interactions and coordination capabilities of these amidines in metal complexes.

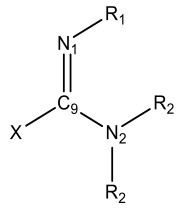

Figure 4.12: The general core structure of the overlay between DBU and TMG. Where N_1 is the coordinating nitrogen atom and X is a carbon atom in DBU and a nitrogen atom in TMG.

Table 4.10 highlights the comparable parameters of each of the complexes, with certain notations standardized to that of [Rh(COD)(DBU)Cl] for simplicity. The changes were; $C_1 \rightarrow C_9$ and $C_2 \rightarrow C_{10}$ for *trans*-[Pd(DBN)$_2$Cl$_2$] and $Y_{1/2} \rightarrow X_{1/2}$ for [Rh(COD)(TMG)Cl], while the various planes were done similarly ($\mathbf{P}_{C/Y} \rightarrow \mathbf{P}_X$ and $\mathbf{P}_{N/T} \rightarrow \mathbf{P}_D$ for the DBN and TMG containing complexes respectively). Note: $\mathbf{P}_{X(n)}$ (n = 1 is the plane parallel to the base, n = 2 is the plane perpendicular to the base) and $\mathbf{P}_{D(n)}$ (n = 1 is the average plane through the base, n = 2/ 3 is the plane through the different rings or appendages; see further explanations in Tables 4.3, 4.5 and 4.8 above).

The *trans*-[Pd(DBN)$_2$Cl$_2$] complex exhibits a unique centrosymmetry, with the Pd(II) centre located on the (0, 0, 0) position and an inversion centre with equivalent atoms generated using the symmetry transformation: -x, -y, -z. The positional disorder on the N_1 and C_1 atoms, the space around each molecule and the centrosymmetry supports the notion that the DBN ligands are flipping about the $\mathbf{P}_{C2}$ plane (N_1-Pd-$_i$$N_1$). When compared to the *trans*-[Pd(DBU)$_2$I$_2$] complex from literature, the difficulty in isolating the crystal structure of the chlorido containing complex may be ascribed to the steric influence this anionic ligand applies on the amidine ligand by the observation of a shorter bond relative to that noted for the iodido analogue [3]. This is also supported by the stronger coordination of the DBU in the literature structure compared to the *trans*-[Pd(DBN)$_2$Cl$_2$] complex isolated in this study, regardless of the collection at a higher temperature, increased steric nature and reduced nucleophilicity compared to DBN. This may be further confirmed by varying only the anion (group 17 halides) relative to the same nucleophilic ligand may indicate that reducing the electronegativity of the anion results in a reduced bond length for the amidine. The title complex planarity is distorted with DBN angled away from the chlorido ligand.

Table 4.10: Selected bond distances and angles for [Rh(COD)(DBU)Cl] and [Rh(COD)(TMG)Cl], *trans*-[Pd(DBN)$_2$Cl$_2$], illustrating the similarities between them.

Atoms	[Rh(COD)(DBU)Cl]	[Rh(COD)(TMG)Cl]	*trans*-[Pd(DBN)$_2$Cl$_2$]
	Bond length (Å)		
Rh-X_1	2.015(6)	1.992(5)	
Rh-X_2	1.978(5)	1.986(4)	
C_9-N_1	1.296(2)	1.298(6)	1.259(10)
C_9-N_2	1.354(2)	1.370(6)	1.346(8)
Rh/Pd-Cl	2.3776(7)	2.377(1)	2.301(2)
Rh/Pd-N_1	2.107(2)	2.097(4)	2.021(7)
	Bond, torsion and dihedral angles (°)		
N_1-C_9-N_2	123.8(2)	122.4(5)	125.5(8)
N_1-C_9-C_{10}/N_3	119.1(2)	122.3(4)	113.7(6)
N_2-C_9-C_{10}/N_3	117.2(2)	115.3(4)	120.7(7)
N_1-Rh/Pd-Cl	88.40(5)	88.2(1)	93.0(2)
X_1-Rh-N_1	176.47(5)	176.2(1)	
X_2-Rh-N_1	91.52(6)	92.5(1)	
C_8-C_1-C_2-C_3	3.3(3)	2.9(10)	
C_4-C_5-C_6-C_7	4.1(4)	2.6(10)	
C_2-C_3-C_4-C_5	27.3(4)	12(1)	
C_6-C_7-C_8-C_1	28.0(4)	14(1)	
Rh/Pd-N_1-C_9-N_2	167.2(2)	134.8(4)	176.2(6)
Cl-Rh/Pd-N_1-C_9	80.5(2)	34.8(4)	-72.5(7)
Bite angle (χ)[a]	87.9(2)	87.7(2)	
Jaw angle (ψ)[a]	75.3(3)	64.7(4)	
Twist angle (τ)[a]	3.5(5)	4.0(9)	
$\mathbf{P}_{X1}$-$\mathbf{P}_{D1}$	21.8(2)	44.0(3)	29.2(8)
$\mathbf{P}_{X2}$-$\mathbf{P}_{D1}$	74.6(1)	50.6(2)	83.5(3)
$\mathbf{P}_{D2}$-$\mathbf{P}_{D3}$	40.3(1)	57.0(2)	6.1(3)

Planes: $\mathbf{P}_{X1}$(Vertical through chlorido), $\mathbf{P}_{X2}$(Horizontal plane through N_1), $\mathbf{P}_{D1}$(Plane through nucleophilic ligand)
Dihedral angle: $\mathbf{P}_{D2}$ - $\mathbf{P}_{D3}$ (Angle between rings/appendages of the nucleophiles).
a) See Fig. 4.1 for definitions and depictions.

The structure of the [Rh(COD)(DBU)Cl] complex reported here was in agreement with the structure in literature, varying slightly due to the data collection being done at a higher temperature [7]. This may be illustrated by the overlaying of the two structures (Fig. 4.13), from which it can be seen that the olefinic bond lengths are slightly longer in the literature complex, and that the chair conformation is also angled towards the COD. The [Rh(COD)(TMG)Cl] complex, in contrast, is stabilized by intramolecular hydrogen bonding between the hydrogen atom, on the methyl group, to the nitrogen on the opposing appendage, which aided in stabilizing the complex.

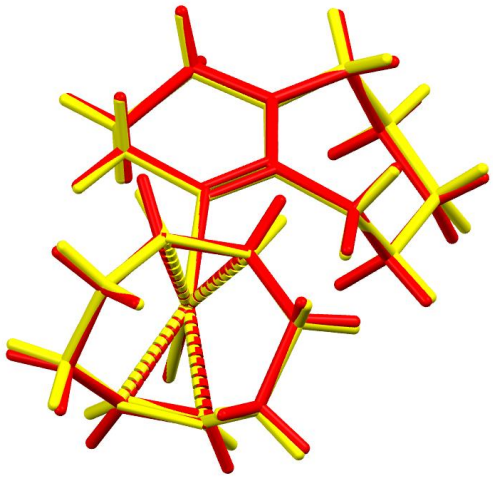

Figure 4.13: Graphical illustration of the overlay of the reported structure (red) and literature structure of [Rh(COD)(DBU)Cl], RMS = 0.0761

When comparing the rhodium complexes to the palladium complex, no significant hydrogen interactions were found, with the exception of the intramolecular hydrogen bonding noted for [Rh(COD)(TMG)Cl]. Moreover, the angles (Table 4.10) around the carbon atom, between the nitrogen atoms, all adopted a distorted trigonal hybridized (sp^2) geometry with the largest observed for the DBN ligand. The bond angle between the base and the chlorido (N_1-Rh/Pd-Cl) was smaller for the Rh(I) complexes than for the Pd(II), assumed to be partly because of less steric hindrance afforded to the absence of the cyclooctadiene in the DBN complex. The torsion angles about the metal-N_1 bond were the largest in both the cyclic bases, with the larger DBU having the greatest torsion, while the least restricted TMG being the smallest. None of the ligands were planar, with respect to the complexes, due to the conformations adopted by the cyclic bases and the angled geometry of the TMG.

By comparing the two rhodium structures collected, the TMG seemingly coordinates stronger than DBU to the metal centre (supported by the shortened bond length to Rh(I)) even though TMG is less nucleophilic than DBU (pK_a 13.0 *vs* 13.5; Chapter 2, Table 2.3). The net COD-bonds *trans* to the nitrogen-nucleophile is stronger (shorter) for TMG than for DBU but weaker (longer) for the bond *trans* to the chlorido. This observation can be attributed to the antibonding lone-pair on the coordinating nitrogen of the TMG which enhances electron donation to the electrophilic metal centre through π-donation and in turn increases π back-donation to the COD, resulting in a shorter bond length for Rh-N_1, and the *trans* olefinic bond (Rh-Y_1) but a marginally larger *cis* olefinic bond (Rh-Y_2) length because of the *trans*-effect of the chlorido. Yet, the stronger Rh-Y_1 bond can also be associated with the weaker σ-bond formed by Rh-N_1 which lowers its *trans* influence on the COD [17]. Furthermore, the *bite* angle (χ) varied slightly between the two, with [Rh(COD)(DBU)Cl] = 87.9 (2)° being the larger value, the *jaw* angle (ψ) showed a significant difference between the two complexes (ψ = 75.3(3)° and 64.7(4)° for the DBU and TMG complexes respectively). The smaller value for [Rh(COD)(TMG)Cl] could be the result of the excess electron density in the π antibonding orbitals causing steric hindrance towards the back-bones of the COD. The reduced torsion on the back-bone also supports this notion, in relation to [Rh(COD)(DBU)Cl]. The *twist* angle (τ) illustrated the rotation of the COD with respect to the *trans* ligands which indicated that the angle sizes were comparable and contributed to the distorted square planar geometry.

It has to be noted that the structural characteristics obtained from this study introduce definite (new) geometric information on these bases and metal complexes which will be valuable in planning future experiments and pursuing entities and systems which may enable improved "metal-assisted-carbon dioxide fixation" as envisaged in Chapter 1.

Along these lines, Chapter 5 aims to gather more reactivity data to support the strengths of the bonds found by the reported structural work, and further compare [Rh(COD)(DBU)Cl] and [Rh(COD)(TMG)Cl] through a kinetic study involving substitution by another strong base, DMAP as entering ligand. Based on the results of this chapter, the Rh(I) complex containing TMG should show increased reactivity because of the two electron donating pathways (σ and π donation) to the metal centre aiding π back-donation to the diolefin. As stated before, this results in the cyclooctadiene becoming less steric, which reduces its hindrance over the coordination sites.

4.7 References

[1] F. H. Allen, "The Cambridge Structural Database: a quarter of a million crystal structures and rising", *Cambridge Crystallogr. Data Cent.*, 380–388 (2002).

[2] *ConQuest*, version 1.21, CCDC ©, Cambridge, United Kingdom, (2018)

[3] V. De La Fuente, C. Godard, E. Zangrando, C. Claver, & S. Castillón, "A phosphine-free Pd catalyst for the selective double carbonylation of aryl iodides", *Chem. Commun.*, **48,** 1695–1697 (2012).

[4] M. Shahinpoor, & M. S. Thompson, "The Venus Flytrap as a model for a biomimetic material with built-in sensors and actuators", *Mater. Sci. Eng. C*, **2,** 229–233 (1995).

[5] T. N. Hill, & A. Roodt, "Solid-state and Computational Study of "Venus fly-trap" Geometric Parameters for 1,5-Cyclooctadiene in Pd ^{II} and Pt ^{II} β-Enaminonato Complexes", *Zeitschrift für Anorg. und Allg. Chemie*, **644,** 763–774 (2018).

[6] T. N. Hill, A. Roodt, & G. Steyl, "Probing the 'Venus fly-trap' parameters of cyclo-octadiene in selected β-diketonato complexes of platinum(II) and the nickel-triad from a spectroscopic, X-ray crystallographic and DFT study", *Polyhedron*, **50,** 82–89 (2013).

[7] U. Flörke, U. Ortmann, & H. -J Haupt, "Rhodium(I)-cyclooctadiene (cod) complexes with the N-donor ligands 1,8-diazabicyclo[5.4.0]undec-7-ene (dbu) and 1,5-diazabicyclo[4.3.0]non-5-ene (dbn)", *Acta Crystallogr. Sect. C*, **48,** 1663–1665 (1992).

[8] *SAINT-Plus*, version 6.02 (including XPREP); Bruker AXA, Inc.: Madison, WI, USA, (1999).

[9] *SADABS*, version 2004/1; Bruker AXS, Inc.: Madison, WI, USA, (2004).

[10] Altomare, A., Burla, M.C., Camalli, M., Cascarano, G.L., Giacovazzo, C., Guagliardi, A., Moliterni, A.G.G., Polidori, G., Spagna,R., *J. Appl. Cryst*., **32**, 837-838, (1999).

[11] Sheldrick, G. M., SHELXL97; University of Göttingen: Göttingen, Germany, (1997).

[12] Sheldrick, G. M., *Acta Crystallogr*., **A64**, 112-122, (2008).

[13] Farrugia, L. J., *J. Appl. Crystallogr*. **32**, 837-838, (1999).

[14] Brandenburg, K., Putz, H., DIAMOND, release 3.1b; Crystal Impact GbR: Bonn, Germany, (2005).

[15] Macrae, C. F., Bruno, I. J., Chisholm, J. A., Edgington, P. R., McCabe, P., Pidcock, E., Rodriguez-Monge, L., Taylor, R., van de Streek, J., Wood, P. A., *J. Appl. Cryst*., **41**, 466-470, (2008).

[16] T. N. Hill, "Diolefin complexes of transition metals as 'Venus fly-trap' templates", *University of the Free State, PhD*, (2011)

[17] B. Pinter, V. Van Speybroeck, M. Waroquier, P. Geerlings, & F. De Proft, "trans effect and

trans influence: importance of metal mediated ligand–ligand repulsion", *Phys. Chem. Chem. Phys.*, **15,** 17354 (2013).

5 Kinetics of the DBU and TMG (=L) substitution from [Rh(COD)(L)Cl] complexes by DMAP

What to expect

A kinetic and mechanistic investigation of the substitution reactions of DBU and TMG (=L) in [Rh(COD)(L)Cl] by DMAP, followed by a discussion relating the results to the crystal structures.

5.1 Introduction

The use of kinetic investigations provides an indication of the rate of the chemical reactions taking place. This allows for the changes in the reaction rate to be observed by varying certain variables such as; temperature, concentration and pressure. These observations can lead to the possibility of specifying the intimate mechanism of the reaction being evaluated. Chemical kinetics can thus assist in the elucidation of the mechanistic pathways of catalysts and ligands, which may lead to the optimization of the variables (catalyst, ligands, solvents, products, etc.) [1,2].

The literature of the complexes introduced in Section 2.4.3 had no discussions pertaining to the reaction kinetics, especially those containing the amidines or guanidines. As a result, the mechanistic pathway of the reactions based on the kinetic results could not be assessed. This illustrated the need to determine the kinetics and mechanisms of the bases (see Fig. 1.1) and for improved evaluation of the bases, a comparison between the amidines and guanidines on a model complex were investigated. Thus, the aim of this kinetic study involves proposing the mechanism for the substitution of the DBU and TMG coordinated ligands, from the metal complexes (Fig. 5.1); (a) [Rh(COD)(DBU)Cl] and (b) [Rh(COD)(TMG)Cl], with the neutral DMAP ligand. The investigation was performed under *pseudo* first-order conditions at various temperatures.

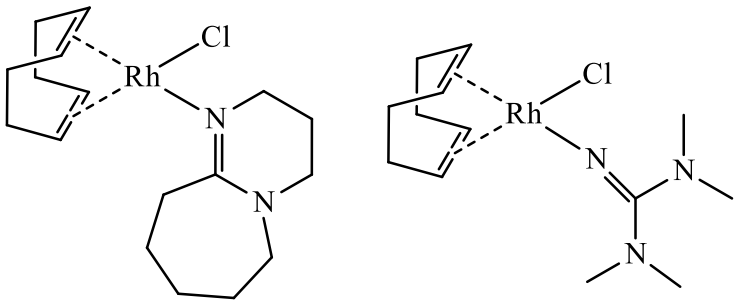

(a) (b)

Figure 5.1: A schematic illustration of the two complexes; (a) [Rh(COD)(DBU)Cl] and (b) [Rh(COD)(TMG)Cl], used in the substitution of the DBU and TMG coordinated ligands.

5.2 Chemicals and instrumentation

The substitution reactions of DBU and TMG from [Rh(COD)(DBU)Cl] and [Rh(COD)(TMG)Cl] complexes by DMAP, as the entering ligand, were studied in this kinetic study. Due to the fast nature of the processes observed from preliminary kinetic reactions, stopped-flow experiments were required – the solvent used for these systems was changed to benzene, in place of DCM, due to equipment limitations on the instrument.

The experiments were all carried out under aerobic conditions with the chemicals, purchased from the Sigma-Aldrich Chemical Company or Merck, being of analytical grade or better and used without further purification. The complexes were synthesized as described in Chapter 3 and all kinetic runs were done under pseudo first-order conditions, with [DMAP]>> [Metal complex].

The UV/Vis spectral and absorbance changes for the preliminary kinetic reactions were measured on a Varian Cary 50 Conc and Varian 100 spectrophotometers, with 1.000 ± 0.001 cm path length tandem quartz cells. The spectrophotometers were all equipped with constant temperature cell holders (accuracy of ± 0.1 °C) and Julabu MPV thermostated water baths (accuracy of ± 0.1 °C) that were fitted with circulators. The fast reactions were studied on a Hi-Tech Scientific Stopped SF-61 DX2 unit, which was connected to a Hi-Tech Scientific SU-40-UV/Vis spectrophotometer unit. The Stopped-Flow could be operated in either the diode-array or the monochromator mode.

The protocol to collect the spectra in both modes are the same with difference being that the time intervals between scans are on the two-millisecond scale for the monochromator mode and as low as ten milliseconds on the diode-array mode. The SF-61 DX2 unit is equipped with a constant temperature cell (accuracy of ± 0.1 °C) that is also connected to a Julabu MPV thermostated water bath (accuracy of ± 0.1 °C) which was fitted with a circulator. The data was processed using Scientist [3] to yield the least-squares analyses of the absorption *vs.* time data from the kinetic runs and the spectral changes, respectively.

5.3 General rate and equilibrium equations

The reaction rate, for a given chemical reaction, is the speed at which the products are formed from the reactants. The more formal definition is the measured change in the concentration of the products or reactants per unit time [4]. For a simple reaction (Eq. 5.1) with two reactants (A as ligand and B as metal complex) and one product (C), such as:

$$aA + bB \rightleftharpoons cC \qquad \text{Eq. 5.1}$$

Here *a*, *b* and *c* are the coefficients of the reactants and product. The observed pseudo first-order rate constant in square-planar substitution reactions {following integration with [A]>>[B]} under non-equilibrium conditions can be expressed as given in Eq. 5.2.

$$k_{obs} = k_1[A] + k_{-1} \qquad \text{Eq. 5.2}$$

The values k_1 and k_{-1} are the forward and reverse rate constants respectively, which relates the rate of change to the reagent concentrations. The rate constants can thus be determined by plotting the observed rate constants (k_{obs}) at various concentrations of [A], where k_1 is the gradient of the graph and k_{-1} is the intercept. If the intercept, k_{-1}, is positive and thus not through the origin, it may indicate the presence of parallel reaction or an equilibrium (reverse reaction). In the case of the latter, the equilibrium constant, K_1, (Eq. 5.3) is defined by

$$K_1 = \frac{k_1}{k_{-1}} \qquad \text{Eq. 5.3}$$

To obtain the k_{obs} values from the kinetic runs at various concentration of entering ligand from the absorbance *vs.* time graphs, a modified Beer-Lambert law leads to the exponential form for the pseudo first-order rate constant in term of time-resolved absorbance data as

$$A_t = A_\infty - (A_\infty - A_0)e^{k_{obs}t} \qquad \text{Eq. 5.4}$$

Here A_t and A_∞ are the absorbances after time *t* and infinite time, respectively. The latter term defines the time at which the reaction is complete, for all practical purposes. Thus, using Eq. 5.4, a plot of the least-squares fit of the absorbance *vs.* time data, from the kinetic reactions, yields the pseudo first-order rate constant, k_{obs}.

To further analyse the reaction mechanism (interchange, associative or dissociative), the Eyring equation (Eq. 5.5) and its linear form (Eq. 5.6), along with the Gibbs free energy equation (Eq. 5.7) were used to determine the activation parameters [5].

$$k_1 = \frac{k_B \cdot T}{h} e^{\frac{-\Delta H^{\neq}}{RT}} e^{\frac{\Delta S^{\neq}}{R}} \quad \text{Eq. 5.5}$$

$$\ln\left(\frac{k_1}{T}\right) = -\left(\frac{\Delta H^{\neq}}{R}\right)\frac{1}{T} + ln\left(\frac{k_B}{h}\right) + \left(\frac{\Delta S^{\neq}}{R}\right) \quad \text{Eq. 5.6}$$

$$\Delta G^{\neq} = \Delta H^{\neq} - T\Delta S^{\neq} \quad \text{Eq. 5.7}$$

Here k_B is the Boltzmann constant, R is the universal gas constant, *h* is Planck's constant, T is temperature in Kelvin, $\Delta H^{\neq}$ is the standard enthalpy change of activation, $\Delta S^{\neq}$ is the standard entropy of activation and $\Delta G^{\neq}$ is the Gibbs free energy of activation. Therefore, a graph of $\ln(k_1/T)$ versus 1/T will have a gradient of $(\Delta H^{\neq}/R)$ and an intercept of $[(\Delta S^{\neq}/R) + \ln(k_B/h)]$, from which the activation parameters can be determined. In addition, providing the system allows constantly reproducible kinetic data to be obtained and accurate temperature measurement, a global fit to determine the activation parameters using all the k_{obs} values and the exponential form of the Eyring equation (Eq. 5.5) in a single fit, may be done. The data obtained from the stopped-flow measurements as reported herein, indeed allowed global fitting.

5.4 Kinetic study of the DBU substitution from the [Rh(COD)(DBU)Cl] complex by DMAP

The preliminary kinetics on the Varian spectrophotometer indicated that the reaction had completed by the time the first reading was taken, after mixing, thus within some 5 s. This required the use of stopped-flow techniques. Due to DCM degrading the plastic tubing of the equipment, the solvent had to be changed to benzene, which also has a small polarity [6] and coordinating ability, thus potentially eliminating a solvent pathway. The measurements (100 scans in 1s) were repeated with approximately 10 (3.52 mM) equivalents of DMAP with respect to the [Rh(COD)(DBU)Cl] complex (0.359 mM) at 25.1 °C. Fig 5.2 illustrates the reaction (9 scans in 260 ms), along with the corresponding absorbance *vs*. time graph, at λ = 320 nm, using the monochromator mode (solid line is least-squares fit to Eq. 5.4). This was done to minimize errors in the very fast absorbance changes of the reaction.

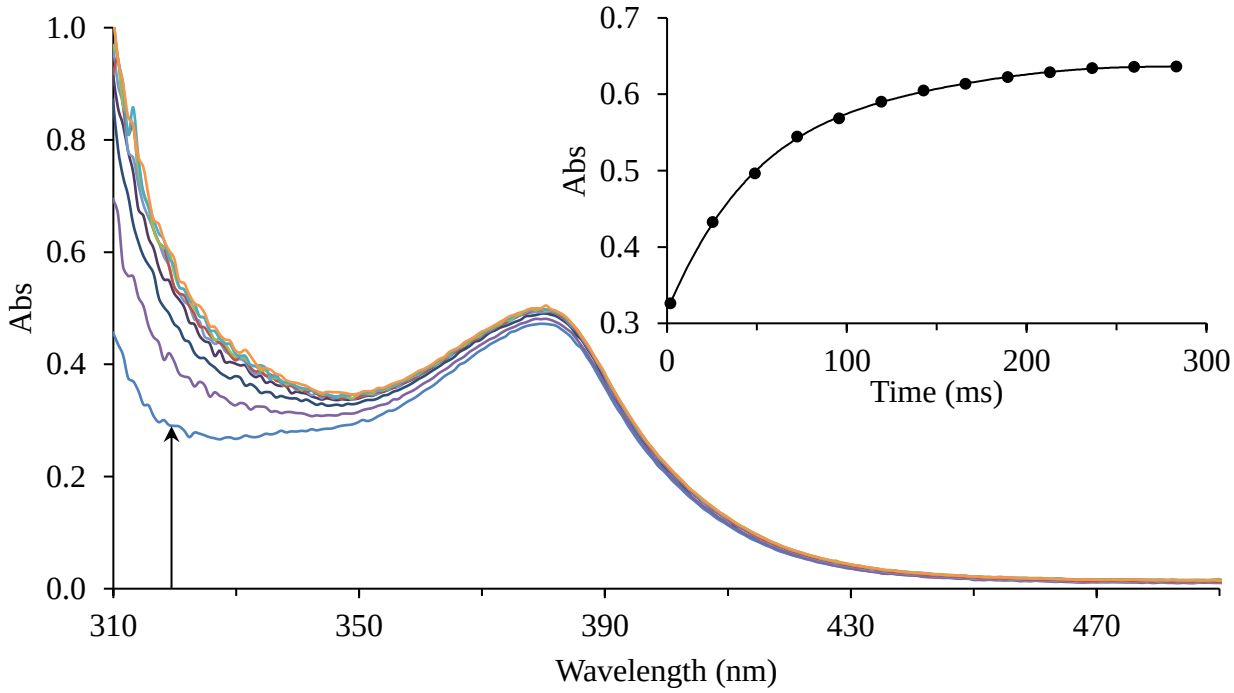

Figure 5.2: Stopped-Flow UV/Vis spectral change for the substitution reaction of [Rh(COD)(DBU)Cl] with DMAP; [Rh] = 0.359 mM, [DMAP] = 3.52 mM, t_{total} = 0.260 ms, Δt = 30 ms, 9 scans, at 25.1 °C in benzene, with spectral change measured at λ = 320 nm. Inset graph illustrated the same reaction conditions, in monochromator mode (λ = 320 nm), with the reaction complete in 283 ms, Δt = 24 ms.

The data and fits in Fig. 5.2 above illustrate the fast nature of the reaction (being complete in t = 300 ms), with a peak maximum at λ_{max} = 380 nm. However, the absorbance change at this wavelength was not used to obtain the k_{obs} values, rather a wavelength of λ = 320 nm was selected because the change in absorbance at the former wavelength was too small to observe a smooth change in absorbance. The k_{obs} data at three different temperatures (15.1 °C, 25.1 °C and 34.9 °C) with DMAP concentrations between 3.52 mM and 35.2 mM was then obtained by fitting the absorbance *vs.* time data to Eq. 5.4, with the results shown in Table 5.1.

Table 5.1: The k_{obs} values for the DMAP substitution reaction with [Rh(COD)(DBU)Cl] at different temperatures. [Rh] = 0.359 mM, [DMAP] = 3.52 – 35.20 mM, λ = 320 nm.

DMAP (mM)	15.1 °C	25.1 °C	34.9 °C
3.52	13.8 ± 0.1	15.3 ± 0.1	30.3 ± 0.9
7.04	20.5 ± 0.1	26.2 ± 0.1	33.5 ± 0.2
14.08	32.7 ± 0.1	43.9 ± 0.3	58.4 ± 0.7
21.28	44.8 ± 0.2	55.9 ± 0.3	75.5 ± 0.7
28.24	55.4 ± 0.2	71.8 ± 0.2	99 ± 1
35.20	64.4 ± 0.3	84.9 ± 0.2	111 ± 1

The values from Table 5.1 were then used to plot k_{obs} *vs.* [DMAP] at the different temperatures (Fig. 5.3). The rate constants k_1, k_{-1} and K_1 were then obtained from Fig. 5.3 using Eq.5.2 and tabulated (Table 5.2). Similarly, the data in Table 5.1 was globally fitted using the three parameters (k_{obs}, temperature and concentration) to interrelate the temperature effects on the observed rate constants at different concentrations to give Fig. 5.4. The results from the graph provided the global fit values for $\Delta H^{\neq}$ and $\Delta S^{\neq}$, which are given in Table 5.2.

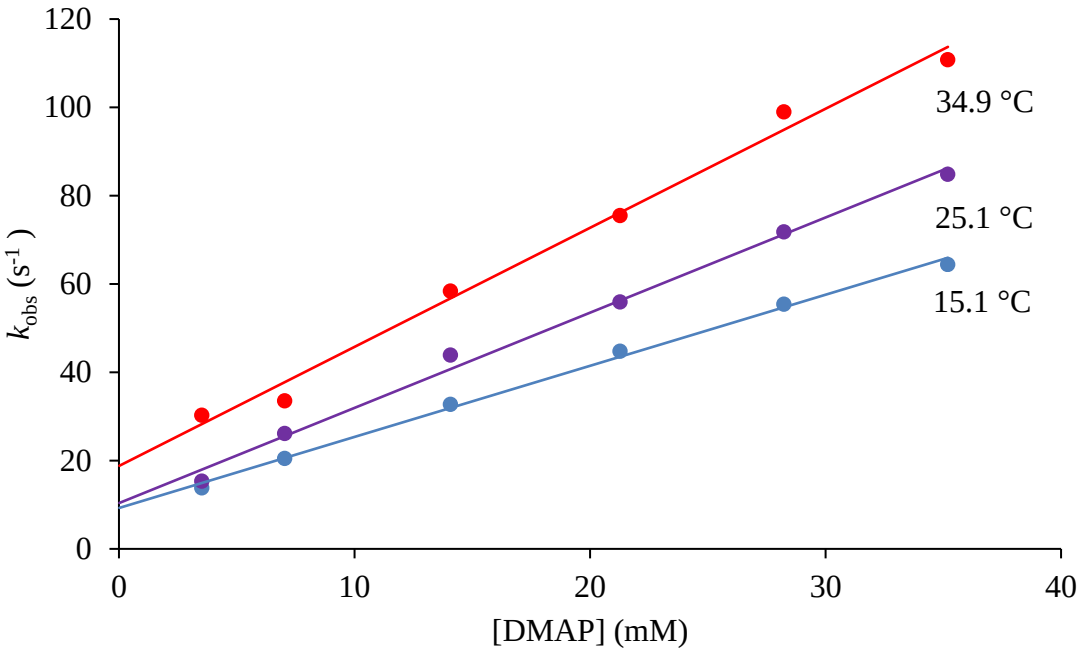

Figure 5.3: Pseudo first-order rate constant (k_{obs}) *vs.* [DMAP] for the substitution reaction in the [Rh(COD)(DBU)Cl] complex at 15.1°C, 25.1°C and 34.9°C, [Rh] = 0.359 mM, [DMAP] = 3.52 – 35.20 mM, λ = 320 nm.

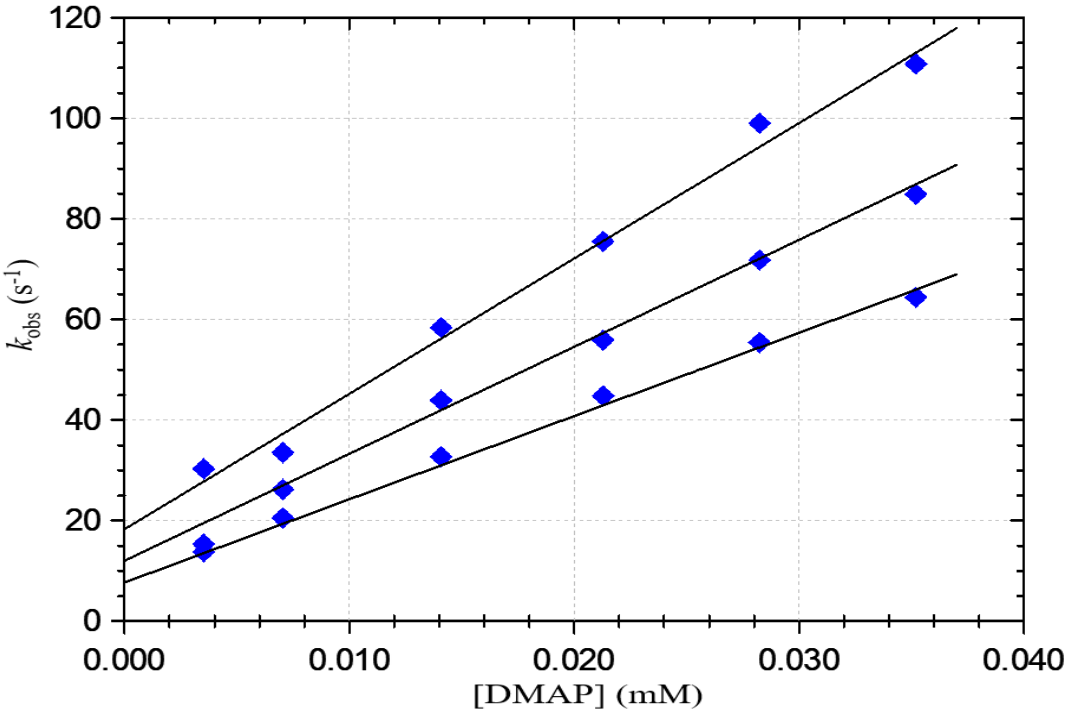

Figure 5.4: Global fit graph of the pseudo first-order rate constant (k_{obs}) *vs.* [DMAP] for the substitution reaction in the [Rh(COD)(DBU)Cl] complex at 15.1°C, 25.1°C and 34.9°C, [Rh] = 0.359 mM, [DMAP] = 3.52 – 35.20 mM, λ = 320 nm.

The values in Table 5.2 was further used to plot the classic Eyring graph (Fig. 5.5) using Eq. 5.6, from which the activation parameters of the overall reaction between the [Rh(COD)(DBU)Cl] complex and DMAP as entering ligand were determined, resulting in a $\Delta H^{\neq} = 17 \pm 1$ kJ mol^{-1} and $\Delta S^{\neq} = -125 \pm 3$ J K^{-1} mol^{-1} and were also added to Table 5.2.

Table 5.2: The kinetic data of the rate constants and activation parameters (at 25.1 °C) between [Rh(COD)(DBU)Cl] and DMAP in benzene.

Constant	15.1 °C	25.1 °C	34.9 °C
k_1 (10^3 M^{-1} s^{-1})	1.61 ± 0.1	2.16 ± 0.08	2.7 ± 0.1
k_{-1} (s^{-1})	9 ± 1	10 ± 2	19 ± 3
K_1 (M^{-1})	174 ± 19	208 ± 36	144 ± 22
Activation Parameters	Experimental	Global fit	
$\Delta H^{\neq}_{k1}$ (kJ mol^{-1})	17 ± 1	16 ± 2[a]	
$\Delta S^{\neq}_{k1}$ (J K^{-1} mol^{-1})	-125 ± 3	-130 ± 8[a]	
$\Delta G^{\neq}_{k1}$ (kJ mol^{-1})	54 ± 1		
$\Delta H^{\neq}_{k-1}$ (kJ mol^{-1})	24 ± 11	30 ± 9[a]	
$\Delta S^{\neq}_{k-1}$ (J K^{-1} mol^{-1})	-145 ± 37	-125 ± 31[a]	

[a] Obtained from the global fit of the data reported in Fig. 5.4

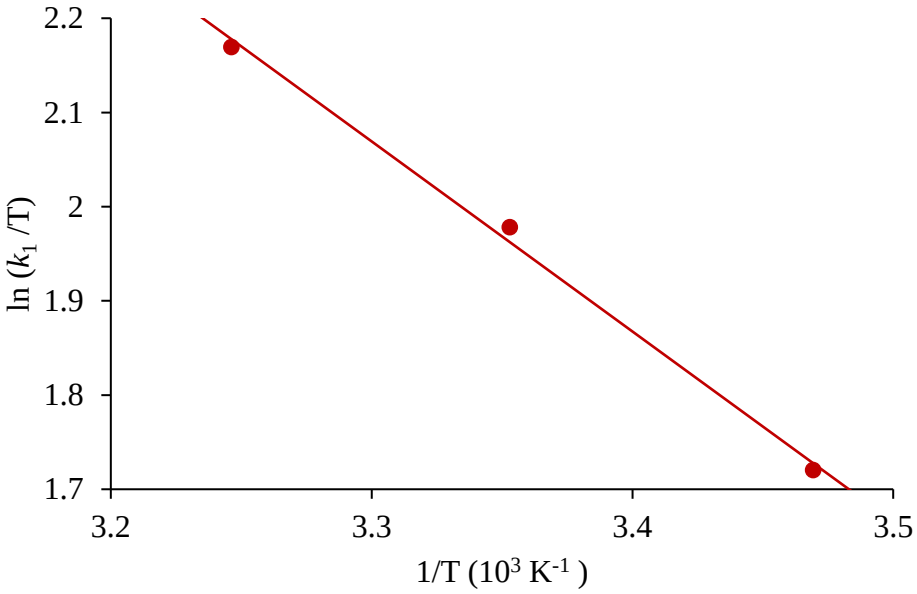

Figure 5.5: Plot of ln (k_1/T) *vs*. 1/T for the reaction between [Rh(COD)(DBU)Cl] and DMAP, for a temperature range of 15.1 – 34.9 °C.

The activation parameters from the global fit of the kinetic data were in excellent agreement with the values for the forward rate constant k_1 but similar for k_{-1}, as seen in Table 5.2. The Gibbs free energy of activation at 25.1 °C was then determined using Eq. 5.7 and found to be $\Delta G^{\neq} = 54 \pm 1$ kJ mol^{-1}. Thus, the percentage of $\Delta H^{\neq}$ and $\Delta S^{\neq}$, in relation to $\Delta G^{\neq}$, was 31 % and 69 %, respectively, indicating a primary entropy driven, associative reaction mechanism.

5.5 Kinetic study of the TMG substitution from the [Rh(COD)(TMG)Cl] complex by DMAP

A similar process was followed with the [Rh(COD)(TMG)Cl] complex on the stopped-flow instrument as in the previous section for the [Rh(COD)(DBU)Cl] complex, with the only change being a reduction in the total reaction time being halved to t_{total} = 0.5 s. The reaction of the metal complex (0.370 mM) with DMAP (3.93mM), at 25.2 °C, was followed - with the absorbance *vs.* wavelength graph shown in Fig. 5.6. The wavelengths were the same as for the [Rh(COD)(DBU)Cl] complex (λ_{max} = 380 nm, with λ = 320 nm being used for the kinetic measurements).

The plot of the absorbance *vs.* time, as seen in Fig. 5.6, reveals that the substitution reaction for the [Rh(COD)(TMG)Cl] complex appears to be ten times faster than the [Rh(COD)(DBU)Cl] complex, being completed in t_{total} = 32 ms and 3 scans. Since the shortest time between scans for the broad-spectrum scan is 10 ms, the monochromator mode was used to give the inset graph with a time between scans of Δt = 3 ms. The k_{obs} data at three different temperatures (15.1°C, 25.2°C and 35°C) was then obtained by fitting the absorbance *vs.* time data to Eq. 5.4, with the results seen in Table 5.3. The values from Table 5.3 were then used to plot k_{obs} *vs.* [DMAP] at the different temperatures (Fig. 5.7). The data in Table 5.3 was used to plot the global fit and determined the global fit values for $\Delta H^{\neq}$ and $\Delta S^{\neq}$ (Table 5.4).

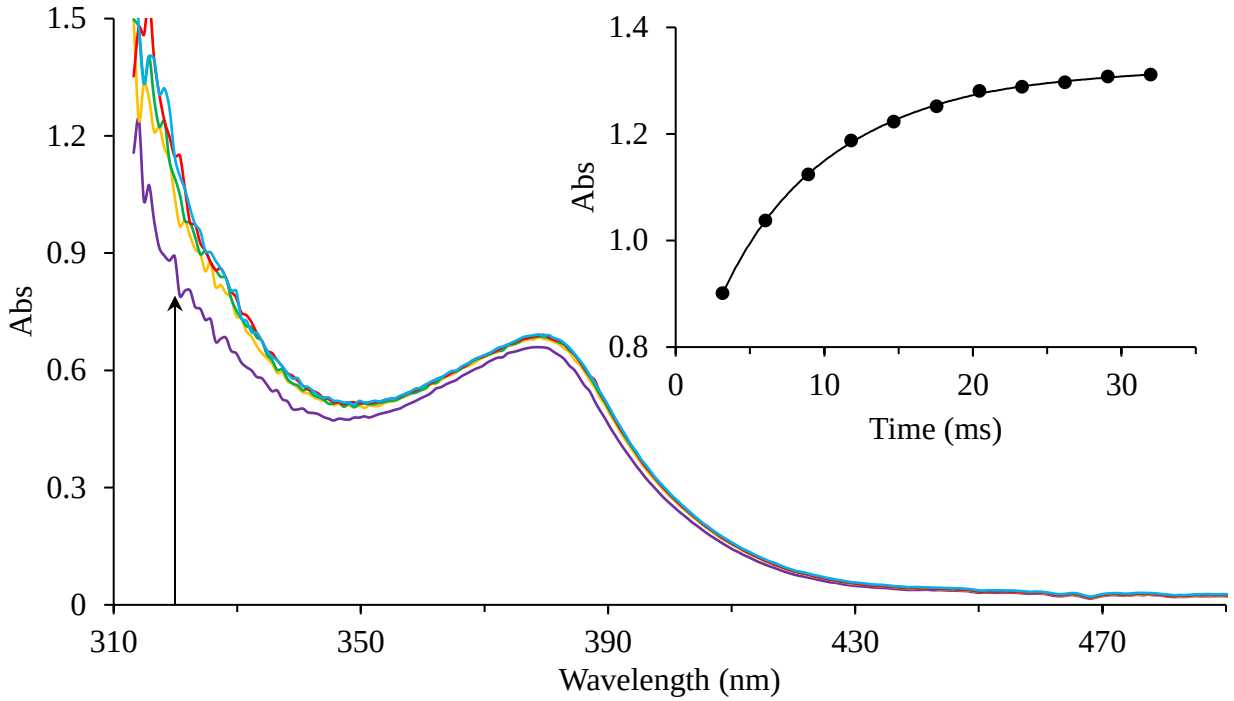

Figure 5.6: UV/Vis spectral change for the substitution reaction of [Rh(COD)(TMG)Cl] with DMAP; [Rh] = 0.370 mM, [DMAP] = 3.93 mM, t_{total} = 50 ms, Δt = 10 ms, 5 scans, at 25.2°C in benzene, with spectral change at λ = 320 nm. Inset graph illustrated the same reaction conditions, in monochromator mode (λ = 320 nm), with the reaction complete in 32 ms, Δt = 3 ms.

Table 5.3: The k_{obs} values for the DMAP substitution reaction with [Rh(COD)(TMG)Cl] at different temperatures. The value in brackets shows the error on the last digit. [Rh] = 0.370 mM, [DMAP] = 3.93 – 38.72 mM, λ = 320 nm.

DMAP (mM)	15.1 °C	25.2 °C	35.0 °C
3.93	95.3 ± 0.3	131.4 ± 0.6	160.2 ± 0.8
7.78	163.5 ± 0.6	228 ± 1	308 ± 2
15.55	307 ± 1	438 ± 4	528 ± 6
23.25	446 ± 4	585 ± 7	775 ± 17
31.02	566 ± 5	762 ± 13	918 ± 23
38.72	733 ± 13	908 ± 15	1149 ± 33

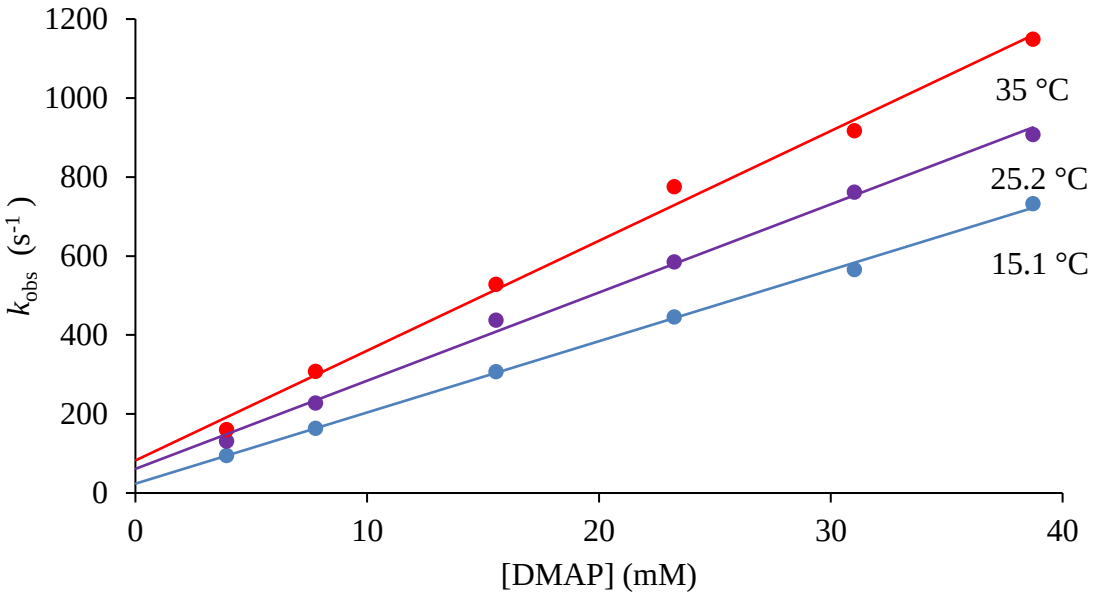

Figure 5.7: Pseudo first-order rate constant (k_{obs}) *vs.* [DMAP] for the substitution reaction in the [Rh(COD)(TMG)Cl] complex at 15.1°C, 25.2°C and 35°C, [Rh] = 0.370mM, [DMAP] = 3.93 – 38.72 mM, λ = 320 nm.

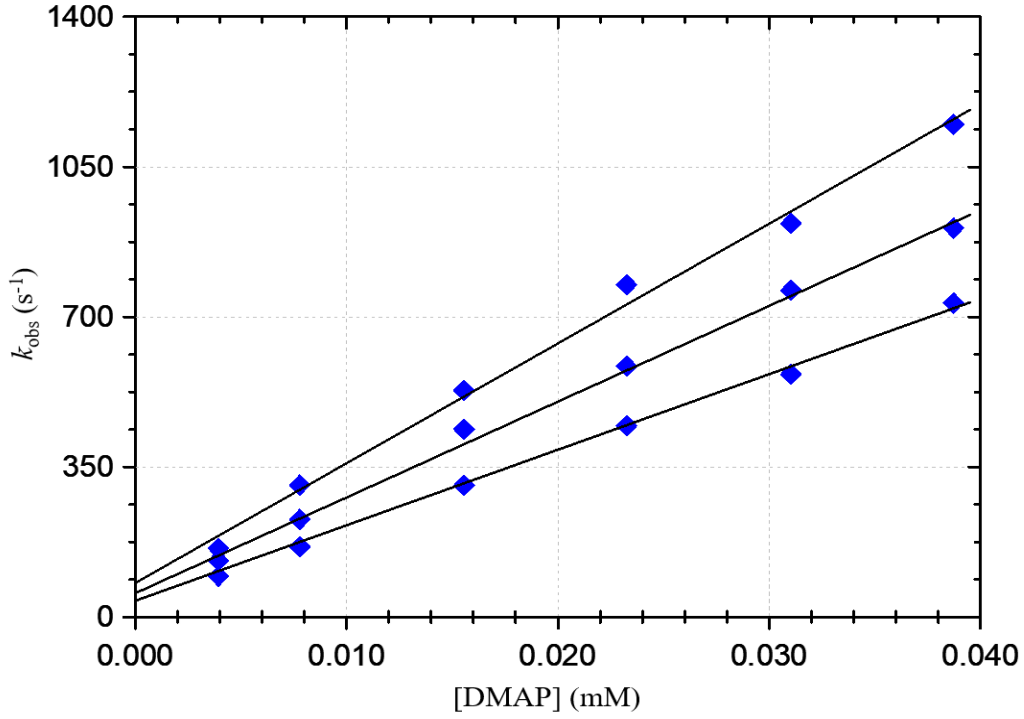

Figure 5.8: Global fit graph of the pseudo first-order rate constant (k_{obs}) *vs.* [DMAP] for the substitution reaction in the [Rh(COD)(TMG)Cl] complex at 15.1°C, 25.2°C and 35°C, [Rh] = 0.370mM, [DMAP] = 3.93 – 38.72 mM, λ = 320 nm.

The line equation from Eq. 5.2 was used to obtain k_1, k_{-1} and K_1 from Fig. 5.6 and tabulated (Table 5.4). The values in Table 5.4 were further used to plot the Eyring graph (Fig. 5.7) using Eq. 5.6, from which the activation parameters of the overall reaction between the [Rh(COD)(TMG)Cl] complex and DMAP as entering ligand were determined, resulting in a $\Delta H^{\neq} = 13.6 \pm 0.6$ kJ mol^{-1} and $\Delta S^{\neq} = -116 \pm 2$ J K^{-1} mol^{-1} and are also shown in Table 5.4.

Table 5.4: The kinetic data of the rate constants and activation parameters (25.2 °C) between [Rh(COD)(TMG)Cl] and DMAP in benzene.

Constant	15.1 °C	25.2 °C	35.0 °C
k_1 (10^3 M^{-1} s^{-1})	18.0 ± 0.3	22.3 ± 0.7	28 ± 1
k_{-1} (s^{-1})	24 ± 8	61 ± 16	82 ± 25
K_1 (M^{-1})	766 ± 264	366 ± 95	338 ± 105
Activation Parameters	Experimental	Global fit	
$\Delta H^{\neq}_{k1}$ (kJ mol^{-1})	13.6 ± 0.6	15 ± 2[a]	
$\Delta S^{\neq}_{k1}$ (J K^{-1} mol^{-1})	-116 ± 2	-113 ± 6[a]	
$\Delta G^{\neq}_{k1}$ (kJ mol^{-1})	48.2 ± 0.6		
$\Delta H^{\neq}_{k-1}$ (kJ mol^{-1})	44 ± 13	25 ± 17[a]	
$\Delta S^{\neq}_{k-1}$ (J K^{-1} mol^{-1})	-64 ± 43	-128 ± 57[a]	

[a] Obtained from the global fit of the data reported in Fig. 5.6

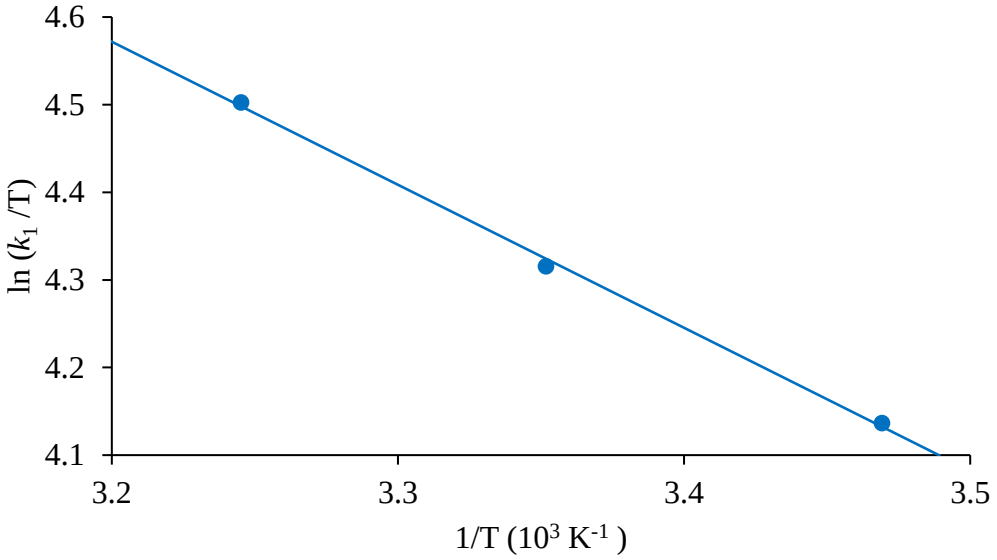

Figure 5.7: Plot of ln (k_1/T) *vs.* 1/T for the reaction [Rh(COD)(TMG)Cl] between and DMAP, for a temperature range of 15.1 – 35.0 °C.

The activation parameters from the global fit of the kinetic data were in excellent agreement with the values for the forward rate constant k_1 but similar for k_{-1}, as seen in Table 5.4. The Gibbs free energy of activation at 25.2 °C was then determined using Eq. 5.7 and found to be $\Delta G^{\neq} = 48.2 \pm 0.6$ kJ mol^{-1}. Thus, the percentage of $\Delta H^{\neq}$ and $\Delta S^{\neq}$, in relation to $\Delta G^{\neq}$, was 28 % and 72 %, respectively, indicating as in the case of the DBU complex above, a primary entropy driven, associative reaction mechanism.

5.6 Discussion

The two neutral Rh(I) complexes that were chosen in this study contained either DBU or TMG coordinated *trans* to the 1,5-cyclooctadiene (COD) ligand. The kinetic study focused primarily on the influence of the leaving group (DBU and TMG) on the rate of the DMAP substitution. The leaving groups determine the electron density on the metal centre, and thus the rate of attack by the DMAP as entering nucleophile in a typical and classic associative mechanism. The experimental results support this notion due to the negative $\Delta S^{\neq}$ value in both complexes.

The electron-withdrawing capability of the COD ligand in the two metal complexes, [Rh(COD)(DBU)Cl] and [Rh(COD)(TMG)Cl], reduced the electron density on the rhodium centre, rendering them both electrophilic. Since the TMG has a smaller pK_a value than DBU (pK_a 13.0 *vs* 13.5; Chapter 2, Table 2.3), it is a weaker electron donor than DBU which results in a more electron-poor metal centre. Accordingly, an entering nucleophile such as DMAP will via an associative activation enter the coordination sphere of the [Rh(COD)(TMG)Cl] much faster than the DBU containing complex.

The forward rate constant k_1 is ten times faster for the TMG-complex than for the DBU-complex, with neither experiencing a strong solvation/reverse pathway. The substitution in both complexes are entropy controlled, with [Rh(COD)(TMG)Cl] being *ca.* 3 % more entropy driven than the DBU-complex. This further supports the influence of the pK_a value on enhancing the electrophilicity of the metal centre.

Thus, the substitution reaction of DBU and TMG from [Rh(COD)(DBU)Cl] and [Rh(COD)(TMG)Cl] by DMAP is clearly indicative of an associative activated mechanism, wherein the transition state, being more stabilized in the case of the TMG, resulting in a lowering of the activation energy and yielding a corresponding faster reaction.

As further noted in Chapter 2, the CO_2 molecule contains two nucleophilic oxygen atoms and one *electrophilic* carbon but due to the linear geometry of the complex, the molecule is relatively inert and nonpolar, like the relatively nonpolar benzene solvent. However, both DBU and TMG have shown to activate CO_2 through coordination to the electrophilic carbon, distorting the geometry and allowing for the oxygens to act as nucleophiles. Thus, the substitution kinetics of CO_2 with the two rhodium complexes may follow similar rates but will have a rate limiting step of being first 'activated' by the DBU or TMG before proceeding with the substitution. Additionally, if performed under supercritical CO_2, the large solvent pathway may add to the reaction rate.

Table 5.5: The comparison of the rate constants and activation parameters of the DMAP substitution reaction for the [Rh(COD)(DBU)Cl] and [Rh(COD)(TMG)Cl] complexes under similar conditions.

Complex	k_1 (10^3 M^{-1} s^{-1})	k_{-1} (s^{-1})	K_1 (M^{-1})	$\Delta H^{\neq}_{k1}$ (kJ mol^{-1})	$\Delta S^{\neq}_{k1}$ (J K^{-1} mol^{-1})	$\Delta G^{\neq}_{k1}$ (kJ mol^{-1})
[Rh(COD)(DBU)Cl]	2.16 ± 0.08	10 ± 2	208 ± 36	17 ± 1	-125 ± 3	54 ± 1
				16 ± 2[a]	-130 ± 8[a]	
[Rh(COD)(TMG)Cl]	22.3 ± 0.7	61 ± 16	366 ± 95	13.6 ± 0.6	-116 ± 2	48.2 ± 6
				15 ± 2[b]	-113 ± 6[b]	

[a] Obtained from the global fit of the data reported in Fig. 5.3, [b] Obtained from the global fit of the data reported in Fig. 5.6

Finally, it may be noted that these reactions investigated within this MSc study are extremely fast, the combination of the nucleophiles with metal centres may surely be explored further to provide potentially even a "one-pot" reaction wherein the carbon dioxide is captured, but then further functionalised *intra*molecularly via appropriate substituents available on the metal. This will be pursued further in future.

5.7 References

[1] C. Capellos, & B. H. J. Bielski, "Kinetic Systems", *Wiley-Interscience*, (1972)

[2] A. F. Frost, & R. G. Pearson, "Kinetics and Mechanism", *John Wiley & Sons, Ltd*, (1953)

[3] MicroMath Scientist for Windows, Version 2.01, Copyright © 1986-1995, MicorMath, Inc.

[4] R. B. Jordan, "Reaction Mechanisms of Inorganic and Organometallic Systems", *Oxford: Oxford University Press, Inc.*, (1991)

[5] C. H. McAteer, & P. Moore, "Rates and activation parameters for dimethyl sulphoxide exchange with hexakis(dimethyl sulphoxide)-nickel(II), -cobalt(II), and -iron(III) ions", *J. Chem. Soc. Dalt. Trans.*, 353–357 (1983).

[6] C. Reichardt, "Solvents and Solvent Effects in Organic Chemistry", *Solvents and Solvent Effects in Organic Chemistry Wiley-VCH Verlag GmbH & Co. KGaA*, (2002)

6 Study evaluation

What to expect

A summary of the results obtained in this M.Sc study and its scientific relevance, as well as a discussion on future research possibilities.

6.1 Results and scientific relevance of the study

The main motivation for this M.Sc study was to investigate aspects relevant to the fixation and activation pathways of CO_2. The research into the utilization of carbon dioxide as a C_1-feedstock has gained significant impetus over the past two decades as a method to potentially reduce its influence on global warming. Since nature performs the task of CO_2-utilization effectively, different systems were analysed to approach it biomimetically to attempt resolving the high energy barrier needed for anthropogenic fixation. This resulted in the identification of two classes of "superbases", namely the amidines and guanidines. Moreover, it led to the focus of the study to be on the activation abilities that they have on CO_2 by assessing the bases in organic and organometallic systems with respect to fixation, to eventually also investigate and evaluate "metal assisted" affects thereof.

A solution study of carbon dioxide with the amidines (1,8-diazabicyclo[5.4.0]undec-7-ene (**DBU**) and 1,5-diazabicyclo[4.3.0]non-5-ene (**DBN**)) and guanidines (1,5,7-triazabicyclo[4.4.0]dec-5-ene (**TBD**), 1,1,3,3-tetramethylguanidine (**TMG**)) illustrated that TBD showed the strongest coordinating ability towards CO_2, while the others exhibited a fractional ability to fix CO_2. The results indicated that various factors could influence the fixation ability of nucleophiles, such as a higher pK_a increasing coordination, steric influence obstructing the bent conformation of the activated CO_2 and the presence of a β-hydrogen to stabilize the coordinated CO_2. This knowledge was then applied to known organometallic systems which contained the bases as ligands. This further led to the selection of two model complexes which were used to synthesis complexes of

the general formulae *trans*-[Pd(L)$_2$Cl$_2$] and [Rh(COD)(L)Cl] (L = (DBU, DBN, TMG, TBD)). All of the complexes were successfully synthesized, with the exception of [Rh(COD)(TBD)Cl], and characterized by infrared and nuclear magnetic resonance spectroscopy. The IR spectra indicated a general increase in electron density on the metal centres but DBN showed a slight decrease due to the minimal increase in the C=N frequency. Also, TMG was noted to have two C=N frequencies which were likely due to resonance within the ligand and was also confirmed by ^{1}H and ^{13}C NMR due to the broad peaks observed in both. Of the complexes synthesized, three (of which two were novel) were crystallographically characterized to verify the formation of the complexes and determine the coordination modes of the ligands. The bond distances and angles were compared to those in literature and related well based on the different temperature collections.

Kinetic investigations into the substitution of DBU and TMG (=L) from the [Rh(COD)(L)Cl] complexes by DMAP yielded extremely fast results. The substitution reactions were indicative of an associative activated mechanism where the latter complex was significantly faster than the DBU-complex. This was accounted for by the transition state being stabilized by TMG which resulted in a lower activation energy and further supported by its crystallographic data because of the two electron donating pathways (σ and π donation) to the metal centre aiding π back-donation to the diolefin. This in turn resulted in the cyclooctadiene seemingly becoming less steric, which reduced its hindrance over the coordination sites and increased the reaction rate.

The results in this M.Sc study illustrated some fundamentals and the potential of these complexes to be used in “one-pot” reactions wherein CO_2 can be used as a C_1-feedstock by capturing and functionalized *intra*molecularly via “metal assisted” pathways based on the use of appropriate substituents on the metal centre.

6.2 Future research

Based on the results obtained from this study, the current knowledge on carbon dioxide fixation in these systems and activation therein can be expanded through further investigation of the coordination modes and kinetic behaviour of the systems wherein the amidines and guanidines are present. This includes:

- Isolation of single crystals of the complexes that were not crystallographically analysed in this study and incorporating other olefinic and π-backbonding ligands.
- Kinetic investigation of both the Rh(I) and Pd(II) complexes with various neutral ligands.
- Synthesise Rh(I) and Pd(II) complexes where the chlorido ligands are replaced with less electronegative atoms.
- Expand the metals analysed to include platinum complexes and compare them relative to the rhodium and palladium complexes.
- Re-synthesise Rh-TBD complex to better compare the effect of the complexes with respect to the coordinated bases.
- Evaluate the reaction mechanism of CO_2 fixation in more depth.
- Evaluate the catalytic ability of the metal complexes in CO_2-fixation and consecutive conversion possibilities.
- Theoretical computational calculations to assist in understanding the kinetic and coordination behaviour of the bases to the metal centres and towards CO_2.

Appendix A

i. *trans*-[Pd(DBN)$_2$Cl$_2$]

Table A.1: Atomic coordinates (x 10^4) and equivalent isotropic displacement parameters (Å^2 x 10^3) for *trans*-[Pd(DBN)$_2$Cl$_2$]. U(eq) is defined as one third of the trace of the orthogonalized U_{ij} tensor.

	x	y	z	U(eq)
C(1)	-1518(11)	-556(10)	-2162(6)	64(1)
C(2)	245(11)	237(8)	-2399(6)	74(1)
C(3)	121(12)	-172(8)	-3508(7)	82(1)
C(4)	-1799(10)	-675(9)	-3891(5)	78(1)
C(5)	-4456(10)	-1754(9)	-3069(6)	83(1)
C(6)	-4667(11)	-2227(10)	-2031(6)	91(1)
C(7)	-3636(9)	-1360(9)	-1182(6)	80(1)
N(1)	-1822(9)	-653(9)	-1253(5)	64(1)
N(2)	-2656(7)	-1051(6)	-3006(4)	67(1)
Cl(1)	2009(3)	-1901(2)	-107(1)	79(1)
Pd(1)	0	0	0	49(1)
N(0AA)	-760(30)	-180(20)	-1546(18)	60(2)
C(0AA)	-2330(60)	-890(50)	-1970(30)	61(2)

Table A.2: Bond distances (Å) and angles (°) for *trans*-[Pd(DBN)$_2$Cl$_2$].

Atoms	Bond distances (Å)	Atoms	Angles (°)
C(1)-C(0AA)	0.75(4)	C(0AA)-C(1)-N(0AA)	103(4)
C(1)-N(0AA)	0.96(2)	C(0AA)-C(1)-N(1)	51(3)
C(1)-N(1)	1.259(10)	N(0AA)-C(1)-N(1)	52.6(14)
C(1)-N(2)	1.346(8)	C(0AA)-C(1)-N(2)	75(3)
C(1)-C(2)	1.549(11)	N(0AA)-C(1)-N(2)	177.0(17)
C(2)-N(0AA)	1.49(2)	N(1)-C(1)-N(2)	125.5(8)
C(2)-C(3)	1.497(11)	C(0AA)-C(1)-C(2)	171(3)
C(2)-H(2A)	0.97	N(0AA)-C(1)-C(2)	68.2(15)
C(2)-H(2B)	0.97	N(1)-C(1)-C(2)	120.7(7)
C(3)-C(4)	1.469(10)	N(2)-C(1)-C(2)	113.7(6)
C(3)-H(3A)	0.97	N(0AA)-C(2)-C(3)	135.8(10)
C(3)-H(3B)	0.97	N(0AA)-C(2)-C(1)	37.0(9)

C(4)-N(2)	1.455(8)	C(3)-C(2)-C(1)	99.5(6)
C(4)-H(4A)	0.97	C(3)-C(2)-H(2A)	111.9
C(4)-H(4B)	0.97	C(1)-C(2)-H(2A)	111.9
C(5)-N(2)	1.446(8)	C(3)-C(2)-H(2B)	111.9
C(5)-C(6)	1.470(10)	C(1)-C(2)-H(2B)	111.9
C(5)-H(5A)	0.97	H(2A)-C(2)-H(2B)	109.6
C(5)-H(5B)	0.97	C(4)-C(3)-C(2)	108.1(7)
C(6)-C(7)	1.471(10)	C(4)-C(3)-H(3A)	110.1
C(6)-H(6A)	0.97	C(2)-C(3)-H(3A)	110.1
C(6)-H(6B)	0.97	C(4)-C(3)-H(3B)	110.1
C(7)-N(1)	1.484(9)	C(2)-C(3)-H(3B)	110.1
C(7)-C(0AA)	1.58(4)	H(3A)-C(3)-H(3B)	108.4
C(7)-H(7A)	0.97	N(2)-C(4)-C(3)	107.9(6)
C(7)-H(7B)	0.97	N(2)-C(4)-H(4A)	110.1
N(1)-C(0AA)	0.97(4)	C(3)-C(4)-H(4A)	110.1
N(1)-N(0AA)	1.02(2)	N(2)-C(4)-H(4B)	110.1
N(1)-Pd(1)	2.021(7)	C(3)-C(4)-H(4B)	110.1
N(2)-C(0AA)	1.36(4)	H(4A)-C(4)-H(4B)	108.4
Cl(1)-Pd(1)	2.3011(17)	N(2)-C(5)-C(6)	108.5(6)
Pd(1)-N(1)#1	2.021(7)	N(2)-C(5)-H(5A)	110
Pd(1)-N(0AA)	2.03(2)	C(6)-C(5)-H(5A)	110
Pd(1)-N(0AA)#1	2.03(2)	N(2)-C(5)-H(5B)	110
Pd(1)-Cl(1)#1	2.3011(17)	C(6)-C(5)-H(5B)	110
N(0AA)-C(0AA)	1.35(5)	H(5A)-C(5)-H(5B)	108.4
		C(5)-C(6)-C(7)	115.2(6)
		C(5)-C(6)-H(6A)	108.5
		C(7)-C(6)-H(6A)	108.5
		C(5)-C(6)-H(6B)	108.5
		C(7)-C(6)-H(6B)	108.5
		H(6A)-C(6)-H(6B)	107.5
		C(6)-C(7)-N(1)	122.0(6)
		C(6)-C(7)-C(0AA)	86.2(16)
		N(1)-C(7)-C(0AA)	36.9(14)
		C(6)-C(7)-H(7A)	106.8
		N(1)-C(7)-H(7A)	106.8
		C(6)-C(7)-H(7B)	106.8
		N(1)-C(7)-H(7B)	106.8
		H(7A)-C(7)-H(7B)	106.7
		C(0AA)-N(1)-N(0AA)	85(3)
		C(0AA)-N(1)-C(1)	36(3)
		N(0AA)-N(1)-C(1)	48.7(13)

C(0AA)-N(1)-C(7)	77(3)
N(0AA)-N(1)-C(7)	161.6(15)
C(1)-N(1)-C(7)	113.2(7)
C(0AA)-N(1)-Pd(1)	160(3)
N(0AA)-N(1)-Pd(1)	75.7(13)
C(1)-N(1)-Pd(1)	124.1(6)
C(7)-N(1)-Pd(1)	122.7(5)
C(1)-N(2)-C(0AA)	32.0(17)
C(1)-N(2)-C(5)	128.1(6)
C(0AA)-N(2)-C(5)	96.1(19)
C(1)-N(2)-C(4)	107.3(6)
C(0AA)-N(2)-C(4)	139.4(19)
C(5)-N(2)-C(4)	124.5(5)
N(1)#1-Pd(1)-N(1)	180
N(1)#1-Pd(1)-N(0AA)	150.8(6)
N(1)-Pd(1)-N(0AA)	29.2(6)
N(1)#1-Pd(1)-N(0AA)#1	29.2(6)
N(1)-Pd(1)-N(0AA)#1	150.8(6)
N(0AA)-Pd(1)-N(0AA)#1	180
N(1)#1-Pd(1)-Cl(1)	87.1(2)
N(1)-Pd(1)-Cl(1)	93.0(2)
N(0AA)-Pd(1)-Cl(1)	86.6(6)
N(0AA)#1-Pd(1)-Cl(1)	93.4(6)
N(1)#1-Pd(1)-Cl(1)#1	92.9(2)
N(1)-Pd(1)-Cl(1)#1	87.0(2)
N(0AA)-Pd(1)-Cl(1)#1	93.4(6)
N(0AA)#1-Pd(1)-Cl(1)#1	86.6(6)
Cl(1)-Pd(1)-Cl(1)#1	180
C(1)-N(0AA)-N(1)	78.7(18)
C(1)-N(0AA)-C(0AA)	32.7(19)
N(1)-N(0AA)-C(0AA)	46(2)
C(1)-N(0AA)-C(2)	74.9(16)
N(1)-N(0AA)-C(2)	154(2)
C(0AA)-N(0AA)-C(2)	108(2)
C(1)-N(0AA)-Pd(1)	153(2)
N(1)-N(0AA)-Pd(1)	75.2(14)
C(0AA)-N(0AA)-Pd(1)	121(2)
C(2)-N(0AA)-Pd(1)	131.1(14)
C(1)-C(0AA)-N(1)	93(4)
C(1)-C(0AA)-N(0AA)	44(3)
N(1)-C(0AA)-N(0AA)	49(2)

C(1)-C(0AA)-N(2)	73(3)
N(1)-C(0AA)-N(2)	166(5)
N(0AA)-C(0AA)-N(2)	117(3)
C(1)-C(0AA)-C(7)	159(5)
N(1)-C(0AA)-C(7)	66(3)
N(0AA)-C(0AA)-C(7)	115(3)
N(2)-C(0AA)-C(7)	128(3)

Symmetry transformations used to generate equivalent atoms: -x,-y,-z .

Table A.3: Anisotropic displacement parameters ($Å^2$ x 10^3) for *trans*-[$Pd(DBN)_2Cl_2$]. The Anisotropic displacement factor exponent takes the form: $-2\pi^2(h^2a^*2U_{11} + \ldots + 2hka^*b^*U_{12})$.

	U_{11}	U_{22}	U_{33}	U_{23}	U_{13}	U_{12}
C(1)	61(2)	79(2)	47(2)	-2(2)	1(2)	-7(2)
C(2)	70(2)	93(3)	58(2)	4(2)	11(2)	-14(2)
C(3)	80(3)	102(3)	64(2)	-3(2)	13(2)	-10(2)
C(4)	83(3)	95(3)	55(2)	-3(2)	7(2)	-8(2)
C(5)	71(2)	99(3)	75(2)	-4(2)	-2(2)	-15(2)
C(6)	76(3)	111(3)	85(3)	-2(2)	12(2)	-19(2)
C(7)	62(2)	105(3)	73(2)	10(2)	10(2)	-17(2)
N(1)	57(2)	85(3)	50(2)	2(2)	5(2)	-9(2)
N(2)	68(2)	82(2)	48(2)	-7(2)	-2(2)	-7(2)
Cl(1)	76(1)	87(1)	72(1)	-2(1)	4(1)	22(1)
Pd(1)	43(1)	68(1)	31(1)	-3(1)	-2(1)	-2(1)
N(0AA)	55(3)	78(3)	45(3)	0(3)	3(2)	-10(3)
C(0AA)	55(3)	78(3)	46(3)	-1(3)	3(3)	-8(3)

Table A.4: Hydrogen coordinates (x 10^4) and isotropic displacement parameters ($Å^2$ x 10^3) for *trans*-[$Pd(DBN)_2Cl_2$].

	x	y	z	U(eq)
H(2A)	159	1275	-2312	89
H(2B)	1386	-121	-1980	89
H(3A)	411	656	-3903	98
H(3B)	1013	-934	-3574	98
H(4A)	-2516	82	-4289	94
H(4B)	-1773	-1512	-4331	94
H(5A)	-4528	-2581	-3527	100
H(5B)	-5455	-1088	-3340	100
H(6A)	-4248	-3222	-1940	109

H(6B)	-5989	-2208	-1983	109
H(7A)	-3414	-1982	-581	96
H(7B)	-4481	-604	-1036	96

Table A.5: Torsion angles (°) for *trans*-[$Pd(DBN)_2Cl_2$].

Atoms	Torsion angles (°)
N(1)-C(1)-C(2)-N(0AA)	-0.2(15)
N(2)-C(1)-C(2)-N(0AA)	177.5(18)
N(0AA)-C(1)-C(2)-C(3)	170.8(16)
N(1)-C(1)-C(2)-C(3)	170.6(8)
N(2)-C(1)-C(2)-C(3)	-11.7(9)
N(0AA)-C(2)-C(3)-C(4)	25.6(17)
C(1)-C(2)-C(3)-C(4)	17.7(8)
C(2)-C(3)-C(4)-N(2)	-18.9(9)
N(2)-C(5)-C(6)-C(7)	27.9(10)
C(5)-C(6)-C(7)-N(1)	-32.0(12)
C(5)-C(6)-C(7)-C(0AA)	-22.5(18)
N(0AA)-C(1)-N(1)-C(0AA)	178(5)
N(2)-C(1)-N(1)-C(0AA)	1(5)
C(2)-C(1)-N(1)-C(0AA)	178(5)
C(0AA)-C(1)-N(1)-N(0AA)	-178(5)
N(2)-C(1)-N(1)-N(0AA)	-177(2)
C(2)-C(1)-N(1)-N(0AA)	0.2(18)
C(0AA)-C(1)-N(1)-C(7)	-2(5)
N(0AA)-C(1)-N(1)-C(7)	175.9(19)
N(2)-C(1)-N(1)-C(7)	-1.3(13)
C(2)-C(1)-N(1)-C(7)	176.1(7)
C(0AA)-C(1)-N(1)-Pd(1)	176(5)
N(0AA)-C(1)-N(1)-Pd(1)	-6.7(18)
N(2)-C(1)-N(1)-Pd(1)	176.2(6)
C(2)-C(1)-N(1)-Pd(1)	-6.4(12)
C(6)-C(7)-N(1)-C(0AA)	16(3)
C(6)-C(7)-N(1)-N(0AA)	27(5)
C(0AA)-C(7)-N(1)-N(0AA)	11(5)
C(6)-C(7)-N(1)-C(1)	17.0(12)
C(0AA)-C(7)-N(1)-C(1)	1(3)
C(6)-C(7)-N(1)-Pd(1)	-160.5(6)
C(0AA)-C(7)-N(1)-Pd(1)	-176(3)
N(1)-C(1)-N(2)-C(0AA)	-1(4)

C(2)-C(1)-N(2)-C(0AA)	-178(4)
C(0AA)-C(1)-N(2)-C(5)	2(4)
N(1)-C(1)-N(2)-C(5)	1.6(14)
C(2)-C(1)-N(2)-C(5)	-175.9(7)
C(0AA)-C(1)-N(2)-C(4)	179(4)
N(1)-C(1)-N(2)-C(4)	178.3(9)
C(2)-C(1)-N(2)-C(4)	0.8(9)
C(6)-C(5)-N(2)-C(1)	-15.6(11)
C(6)-C(5)-N(2)-C(0AA)	-14(2)
C(6)-C(5)-N(2)-C(4)	168.2(7)
C(3)-C(4)-N(2)-C(1)	11.1(9)
C(3)-C(4)-N(2)-C(0AA)	12(3)
C(3)-C(4)-N(2)-C(5)	-172.1(7)
C(0AA)-C(1)-N(0AA)-N(1)	2(4)
C(2)-C(1)-N(0AA)-N(1)	-179.8(16)
N(1)-C(1)-N(0AA)-C(0AA)	-2(4)
C(2)-C(1)-N(0AA)-C(0AA)	179(4)
C(0AA)-C(1)-N(0AA)-C(2)	-179(4)
N(1)-C(1)-N(0AA)-C(2)	179.8(16)
C(0AA)-C(1)-N(0AA)-Pd(1)	14(6)
N(1)-C(1)-N(0AA)-Pd(1)	12(3)
C(2)-C(1)-N(0AA)-Pd(1)	-167(5)
C(0AA)-N(1)-N(0AA)-C(1)	-1(3)
C(7)-N(1)-N(0AA)-C(1)	-12(5)
Pd(1)-N(1)-N(0AA)-C(1)	174.3(15)
C(1)-N(1)-N(0AA)-C(0AA)	1(3)
C(7)-N(1)-N(0AA)-C(0AA)	-11(5)
Pd(1)-N(1)-N(0AA)-C(0AA)	176(3)
C(0AA)-N(1)-N(0AA)-C(2)	-2(5)
C(1)-N(1)-N(0AA)-C(2)	0(4)
C(7)-N(1)-N(0AA)-C(2)	-13(9)
Pd(1)-N(1)-N(0AA)-C(2)	174(5)
C(0AA)-N(1)-N(0AA)-Pd(1)	-176(3)
C(1)-N(1)-N(0AA)-Pd(1)	-174.3(15)
C(7)-N(1)-N(0AA)-Pd(1)	174(4)
C(3)-C(2)-N(0AA)-C(1)	-13(2)
C(3)-C(2)-N(0AA)-N(1)	-13(6)
C(1)-C(2)-N(0AA)-N(1)	1(4)
C(3)-C(2)-N(0AA)-C(0AA)	-14(3)
C(1)-C(2)-N(0AA)-C(0AA)	-1(2)
C(3)-C(2)-N(0AA)-Pd(1)	159.6(10)

C(1)-C(2)-N(0AA)-Pd(1)	173(3)
N(0AA)-C(1)-C(0AA)-N(1)	-2(4)
N(2)-C(1)-C(0AA)-N(1)	-179(4)
N(1)-C(1)-C(0AA)-N(0AA)	2(4)
N(2)-C(1)-C(0AA)-N(0AA)	-177.7(16)
N(0AA)-C(1)-C(0AA)-N(2)	177.7(16)
N(1)-C(1)-C(0AA)-N(2)	179(4)
N(0AA)-C(1)-C(0AA)-C(7)	3(16)
N(1)-C(1)-C(0AA)-C(7)	5(12)
N(2)-C(1)-C(0AA)-C(7)	-175(15)
N(0AA)-N(1)-C(0AA)-C(1)	2(4)
C(7)-N(1)-C(0AA)-C(1)	178(4)
Pd(1)-N(1)-C(0AA)-C(1)	-11(12)
C(1)-N(1)-C(0AA)-N(0AA)	-2(4)
C(7)-N(1)-C(0AA)-N(0AA)	176.5(17)
Pd(1)-N(1)-C(0AA)-N(0AA)	-13(8)
N(0AA)-N(1)-C(0AA)-N(2)	-1(19)
C(1)-N(1)-C(0AA)-N(2)	-2(15)
C(7)-N(1)-C(0AA)-N(2)	176(20)
Pd(1)-N(1)-C(0AA)-N(2)	-13(27)
N(0AA)-N(1)-C(0AA)-C(7)	-176.5(17)
C(1)-N(1)-C(0AA)-C(7)	-178(4)
Pd(1)-N(1)-C(0AA)-C(7)	171(7)
N(1)-N(0AA)-C(0AA)-C(1)	-178(6)
C(2)-N(0AA)-C(0AA)-C(1)	2(4)
Pd(1)-N(0AA)-C(0AA)-C(1)	-173(3)
C(1)-N(0AA)-C(0AA)-N(1)	178(6)
C(2)-N(0AA)-C(0AA)-N(1)	179(2)
Pd(1)-N(0AA)-C(0AA)-N(1)	5(3)
C(1)-N(0AA)-C(0AA)-N(2)	-2.5(18)
N(1)-N(0AA)-C(0AA)-N(2)	180(5)
C(2)-N(0AA)-C(0AA)-N(2)	-1(4)
Pd(1)-N(0AA)-C(0AA)-N(2)	-175(2)
C(1)-N(0AA)-C(0AA)-C(7)	-179(6)
N(1)-N(0AA)-C(0AA)-C(7)	3.5(17)
C(2)-N(0AA)-C(0AA)-C(7)	-177(2)
Pd(1)-N(0AA)-C(0AA)-C(7)	8(4)
C(5)-N(2)-C(0AA)-C(1)	-178(3)
C(4)-N(2)-C(0AA)-C(1)	-2(6)
C(1)-N(2)-C(0AA)-N(1)	2(16)
C(5)-N(2)-C(0AA)-N(1)	-176(19)

C(4)-N(2)-C(0AA)-N(1)	1(22)
C(1)-N(2)-C(0AA)-N(0AA)	1.8(13)
C(5)-N(2)-C(0AA)-N(0AA)	-176(3)
C(4)-N(2)-C(0AA)-N(0AA)	0(6)
C(1)-N(2)-C(0AA)-C(7)	178(7)
C(5)-N(2)-C(0AA)-C(7)	-1(4)
C(4)-N(2)-C(0AA)-C(7)	175.9(16)
C(6)-C(7)-C(0AA)-C(1)	-172(15)
N(1)-C(7)-C(0AA)-C(1)	-5(13)
C(6)-C(7)-C(0AA)-N(1)	-167(2)
C(6)-C(7)-C(0AA)-N(0AA)	-169(3)
N(1)-C(7)-C(0AA)-N(0AA)	-2.9(14)
C(6)-C(7)-C(0AA)-N(2)	15(4)
N(1)-C(7)-C(0AA)-N(2)	-179(6)

Symmetry transformations used to generate equivalent atoms: -x,-y,-z .

ii. [Rh(COD)(DBU)Cl]

Table A.6: Atomic coordinates (x 10^4) and equivalent isotropic displacement parameters ($Å^2$ x 10^3) for [Rh(COD)(DBU)Cl]. U(eq) is defined as one third of the trace of the orthogonalized U_{ij} tensor.

	x	y	z	U(eq)
C(1)	7765(3)	922(2)	1469(2)	45(1)
C(2)	6143(3)	1376(2)	2142(2)	45(1)
C(3)	5086(4)	2258(3)	3093(2)	67(1)
C(4)	6106(4)	3352(3)	2784(2)	73(1)
C(5)	7602(4)	3662(2)	1550(2)	60(1)
C(6)	9282(4)	3201(3)	760(2)	59(1)
C(7)	9837(5)	2289(3)	986(3)	85(1)
C(8)	8661(4)	1207(2)	1643(2)	60(1)
C(9)	10672(2)	3644(2)	-1655(2)	35(1)
C(10)	12061(3)	2836(2)	-2103(2)	48(1)
C(11)	12670(3)	1850(2)	-2893(2)	63(1)
C(12)	13990(4)	2261(3)	-4087(2)	76(1)
C(13)	13395(4)	3271(3)	-4217(2)	71(1)
C(14)	12902(3)	4398(2)	-3591(2)	53(1)

C(15)	9805(3)	4919(3)	-2132(2)	64(1)
C(16)	8037(3)	4390(3)	-1071(2)	66(1)
C(17)	7787(3)	4362(2)	-214(2)	55(1)
Cl(1)	7641(1)	997(1)	-71(1)	51(1)
N(1)	9117(2)	3601(2)	-599(1)	38(1)
N(2)	11122(2)	4360(2)	-2398(1)	44(1)
Rh(1)	8085(1)	2323(1)	595(1)	31(1)

Table A.7: Bond distances (Å) and angles (°) for [Rh(COD)(DBU)Cl].

Atoms	Bond distances (Å)	Atoms	Angles (°)
C(1)-C(2)	1.388(3)	C(2)-C(1)-C(8)	123.5(2)
C(1)-C(8)	1.513(3)	C(2)-C(1)-Rh(1)	70.63(12)
C(1)-Rh(1)	2.136(2)	C(8)-C(1)-Rh(1)	112.61(15)
C(1)-H(1)	0.98	C(2)-C(1)-H(1)	114.2
C(2)-C(3)	1.511(3)	C(8)-C(1)-H(1)	114.2
C(2)-Rh(1)	2.126(2)	Rh(1)-C(1)-H(1)	114.2
C(2)-H(2)	0.98	C(1)-C(2)-C(3)	125.2(2)
C(3)-C(4)	1.512(4)	C(1)-C(2)-Rh(1)	71.37(12)
C(3)-H(3A)	0.97	C(3)-C(2)-Rh(1)	109.81(16)
C(3)-H(3B)	0.97	C(1)-C(2)-H(2)	114.1
C(4)-C(5)	1.518(3)	C(3)-C(2)-H(2)	114.1
C(4)-H(4A)	0.97	Rh(1)-C(2)-H(2)	114.1
C(4)-H(4B)	0.97	C(2)-C(3)-C(4)	113.7(2)
C(5)-C(6)	1.397(4)	C(2)-C(3)-H(3A)	108.8
C(5)-Rh(1)	2.099(2)	C(4)-C(3)-H(3A)	108.8
C(5)-H(5)	0.98	C(2)-C(3)-H(3B)	108.8
C(6)-C(7)	1.520(4)	C(4)-C(3)-H(3B)	108.8
C(6)-Rh(1)	2.096(2)	H(3A)-C(3)-H(3B)	107.7
C(6)-H(6)	0.98	C(3)-C(4)-C(5)	112.7(2)
C(7)-C(8)	1.501(4)	C(3)-C(4)-H(4A)	109
C(7)-H(7A)	0.97	C(5)-C(4)-H(4A)	109
C(7)-H(7B)	0.97	C(3)-C(4)-H(4B)	109
C(8)-H(8A)	0.97	C(5)-C(4)-H(4B)	109
C(8)-H(8B)	0.97	H(4A)-C(4)-H(4B)	107.8
C(9)-N(1)	1.296(2)	C(6)-C(5)-C(4)	122.6(3)
C(9)-N(2)	1.354(2)	C(6)-C(5)-Rh(1)	70.44(14)
C(9)-C(10)	1.501(3)	C(4)-C(5)-Rh(1)	113.37(17)
C(10)-C(11)	1.532(4)	C(6)-C(5)-H(5)	114.3

C(10)-H(10A)	0.97
C(10)-H(10B)	0.97
C(11)-C(12)	1.520(4)
C(11)-H(11A)	0.97
C(11)-H(11B)	0.97
C(12)-C(13)	1.506(5)
C(12)-H(12A)	0.97
C(12)-H(12B)	0.97
C(13)-C(14)	1.506(4)
C(13)-H(13A)	0.97
C(13)-H(13B)	0.97
C(14)-N(2)	1.471(3)
C(14)-H(14A)	0.97
C(14)-H(14B)	0.97
C(15)-N(2)	1.465(3)
C(15)-C(16)	1.505(3)
C(15)-H(15A)	0.97
C(15)-H(15B)	0.97
C(16)-C(17)	1.503(3)
C(16)-H(16A)	0.97
C(16)-H(16B)	0.97
C(17)-N(1)	1.464(3)
C(17)-H(17A)	0.97
C(17)-H(17B)	0.97
Cl(1)-Rh(1)	2.3776(7)
N(1)-Rh(1)	2.1072(17)

C(4)-C(5)-H(5)	114.3
Rh(1)-C(5)-H(5)	114.3
C(5)-C(6)-C(7)	125.9(2)
C(5)-C(6)-Rh(1)	70.65(13)
C(7)-C(6)-Rh(1)	110.47(18)
C(5)-C(6)-H(6)	113.8
C(7)-C(6)-H(6)	113.8
Rh(1)-C(6)-H(6)	113.8
C(8)-C(7)-C(6)	113.7(2)
C(8)-C(7)-H(7A)	108.8
C(6)-C(7)-H(7A)	108.8
C(8)-C(7)-H(7B)	108.8
C(6)-C(7)-H(7B)	108.8
H(7A)-C(7)-H(7B)	107.7
C(7)-C(8)-C(1)	112.7(2)
C(7)-C(8)-H(8A)	109
C(1)-C(8)-H(8A)	109
C(7)-C(8)-H(8B)	109
C(1)-C(8)-H(8B)	109
H(8A)-C(8)-H(8B)	107.8
N(1)-C(9)-N(2)	123.76(18)
N(1)-C(9)-C(10)	119.07(17)
N(2)-C(9)-C(10)	117.15(17)
C(9)-C(10)-C(11)	113.7(2)
C(9)-C(10)-H(10A)	108.8
C(11)-C(10)-H(10A)	108.8
C(9)-C(10)-H(10B)	108.8
C(11)-C(10)-H(10B)	108.8
H(10A)-C(10)-H(10B)	107.7
C(12)-C(11)-C(10)	115.0(2)
C(12)-C(11)-H(11A)	108.5
C(10)-C(11)-H(11A)	108.5
C(12)-C(11)-H(11B)	108.5
C(10)-C(11)-H(11B)	108.5
H(11A)-C(11)-H(11B)	107.5
C(13)-C(12)-C(11)	115.4(2)
C(13)-C(12)-H(12A)	108.4
C(11)-C(12)-H(12A)	108.4
C(13)-C(12)-H(12B)	108.4
C(11)-C(12)-H(12B)	108.4
H(12A)-C(12)-H(12B)	107.5

C(12)-C(13)-C(14)	112.9(2)
C(12)-C(13)-H(13A)	109
C(14)-C(13)-H(13A)	109
C(12)-C(13)-H(13B)	109
C(14)-C(13)-H(13B)	109
H(13A)-C(13)-H(13B)	107.8
N(2)-C(14)-C(13)	113.31(18)
N(2)-C(14)-H(14A)	108.9
C(13)-C(14)-H(14A)	108.9
N(2)-C(14)-H(14B)	108.9
C(13)-C(14)-H(14B)	108.9
H(14A)-C(14)-H(14B)	107.7
N(2)-C(15)-C(16)	110.17(19)
N(2)-C(15)-H(15A)	109.6
C(16)-C(15)-H(15A)	109.6
N(2)-C(15)-H(15B)	109.6
C(16)-C(15)-H(15B)	109.6
H(15A)-C(15)-H(15B)	108.1
C(17)-C(16)-C(15)	108.2(2)
C(17)-C(16)-H(16A)	110.1
C(15)-C(16)-H(16A)	110.1
C(17)-C(16)-H(16B)	110.1
C(15)-C(16)-H(16B)	110.1
H(16A)-C(16)-H(16B)	108.4
N(1)-C(17)-C(16)	110.35(19)
N(1)-C(17)-H(17A)	109.6
C(16)-C(17)-H(17A)	109.6
N(1)-C(17)-H(17B)	109.6
C(16)-C(17)-H(17B)	109.6
H(17A)-C(17)-H(17B)	108.1
C(9)-N(1)-C(17)	116.97(17)
C(9)-N(1)-Rh(1)	128.25(14)
C(17)-N(1)-Rh(1)	113.48(13)
C(9)-N(2)-C(15)	121.56(17)
C(9)-N(2)-C(14)	122.62(18)
C(15)-N(2)-C(14)	114.24(17)
C(6)-Rh(1)-C(5)	38.91(11)
C(6)-Rh(1)-N(1)	91.03(8)
C(5)-Rh(1)-N(1)	91.88(8)
C(6)-Rh(1)-C(2)	97.91(9)
C(5)-Rh(1)-C(2)	82.48(9)

N(1)-Rh(1)-C(2)	157.45(8)
C(6)-Rh(1)-C(1)	82.15(9)
C(5)-Rh(1)-C(1)	91.45(10)
N(1)-Rh(1)-C(1)	164.54(8)
C(2)-Rh(1)-C(1)	38.00(9)
C(6)-Rh(1)-Cl(1)	160.86(9)
C(5)-Rh(1)-Cl(1)	160.23(9)
N(1)-Rh(1)-Cl(1)	88.40(5)
C(2)-Rh(1)-Cl(1)	89.73(7)
C(1)-Rh(1)-Cl(1)	93.53(7)

Table A.8: Anisotropic displacement parameters ($Å^2$ x 10^3) for [Rh(COD)(DBU)Cl]. The Anisotropic displacement factor exponent takes the form: $-2\pi^2(h^2a^*2U_{11} + \ldots + 2hka^*b^*U_{12})$.

	U_{11}	U_{22}	U_{33}	U_{23}	U_{13}	U_{12}
C(1)	61(1)	35(1)	48(1)	10(1)	-46(1)	-7(1)
C(2)	45(1)	47(1)	34(1)	11(1)	-30(1)	-16(1)
C(3)	52(1)	81(2)	32(1)	-2(1)	-26(1)	-8(1)
C(4)	94(2)	63(2)	44(1)	-6(1)	-52(2)	-2(2)
C(5)	97(2)	39(1)	52(1)	8(1)	-62(2)	-19(1)
C(6)	76(2)	67(2)	62(1)	29(1)	-62(2)	-38(1)
C(7)	91(2)	114(3)	100(2)	44(2)	-88(2)	-41(2)
C(8)	74(2)	65(2)	66(2)	9(1)	-62(2)	0(1)
C(9)	40(1)	38(1)	33(1)	5(1)	-31(1)	-5(1)
C(10)	38(1)	60(1)	42(1)	10(1)	-32(1)	-3(1)
C(11)	41(1)	50(1)	56(1)	0(1)	-30(1)	-2(1)
C(12)	44(1)	78(2)	44(1)	-11(1)	-23(1)	-14(1)
C(13)	58(1)	98(2)	33(1)	8(1)	-31(1)	-29(2)
C(14)	51(1)	66(2)	39(1)	23(1)	-36(1)	-27(1)
C(15)	67(2)	78(2)	62(2)	23(1)	-56(1)	-7(1)
C(16)	54(1)	89(2)	64(2)	17(1)	-50(1)	3(1)
C(17)	48(1)	58(1)	44(1)	0(1)	-34(1)	14(1)
Cl(1)	63(1)	52(1)	55(1)	-12(1)	-52(1)	5(1)
N(1)	41(1)	43(1)	31(1)	2(1)	-30(1)	2(1)
N(2)	47(1)	54(1)	37(1)	13(1)	-35(1)	-9(1)
Rh(1)	35(1)	34(1)	27(1)	2(1)	-25(1)	-2(1)

Table A.9: Hydrogen coordinates (x 10^4) and isotropic displacement parameters ($Å^2$ x 10^3) for [Rh(COD)(DBU)Cl].

	x	y	z	U(eq)
H(1)	8000	107	1181	55
H(2)	5439	822	2244	54
H(3A)	4634	1841	3709	80
H(3B)	4098	2527	3351	80
H(4A)	6567	3201	2977	88
H(4B)	5326	4040	3219	88
H(5)	7564	4487	1396	72
H(6)	10208	3763	149	70
H(7A)	11010	2016	277	101
H(7B)	9868	2688	1391	101
H(8A)	7783	1354	2431	72
H(8B)	9340	511	1424	72
H(10A)	11620	2455	-1480	58
H(10B)	13056	3328	-2499	58
H(11A)	13179	1196	-2907	76
H(11B)	11659	1528	-2592	76
H(12A)	15038	2521	-4408	91
H(12B)	14298	1572	-4517	91
H(13A)	12397	2998	-3948	86
H(13B)	14321	3463	-5004	86
H(14A)	13719	4512	-3660	63
H(14B)	13004	5089	-3933	63
H(15A)	10103	4783	-2741	77
H(15B)	9781	5785	-2044	77
H(16A)	7137	4879	-804	80
H(16B)	7962	3577	-1208	80
H(17A)	7865	5178	-82	66
H(17B)	6639	4048	486	66

Table A.10: Torsion angles (°) for [Rh(COD)(DBU)Cl].

Atoms	Torsion angles (°)
C(8)-C(1)-C(2)-C(3)	3.3(3)
Rh(1)-C(1)-C(2)-C(3)	-101.5(2)
C(8)-C(1)-C(2)-Rh(1)	104.8(2)
C(1)-C(2)-C(3)-C(4)	49.7(4)
Rh(1)-C(2)-C(3)-C(4)	-31.0(3)
C(2)-C(3)-C(4)-C(5)	27.3(4)
C(3)-C(4)-C(5)-C(6)	-91.1(3)
C(3)-C(4)-C(5)-Rh(1)	-10.1(4)
C(4)-C(5)-C(6)-C(7)	4.1(4)
Rh(1)-C(5)-C(6)-C(7)	-101.7(3)
C(4)-C(5)-C(6)-Rh(1)	105.8(2)
C(5)-C(6)-C(7)-C(8)	48.3(4)
Rh(1)-C(6)-C(7)-C(8)	-32.1(4)
C(6)-C(7)-C(8)-C(1)	28.0(4)
C(2)-C(1)-C(8)-C(7)	-91.7(3)
Rh(1)-C(1)-C(8)-C(7)	-10.6(3)
N(1)-C(9)-C(10)-C(11)	112.4(2)
N(2)-C(9)-C(10)-C(11)	-65.9(3)
C(9)-C(10)-C(11)-C(12)	80.8(3)
C(10)-C(11)-C(12)-C(13)	-58.9(3)
C(11)-C(12)-C(13)-C(14)	58.9(3)
C(12)-C(13)-C(14)-N(2)	-82.2(3)
N(2)-C(15)-C(16)-C(17)	46.7(3)
C(15)-C(16)-C(17)-N(1)	-61.1(3)
N(2)-C(9)-N(1)-C(17)	1.1(3)
C(10)-C(9)-N(1)-C(17)	-177.1(2)
N(2)-C(9)-N(1)-Rh(1)	167.15(15)
C(10)-C(9)-N(1)-Rh(1)	-11.0(3)
C(16)-C(17)-N(1)-C(9)	37.7(3)
C(16)-C(17)-N(1)-Rh(1)	-130.39(19)
N(1)-C(9)-N(2)-C(15)	-15.6(3)
C(10)-C(9)-N(2)-C(15)	162.6(2)
N(1)-C(9)-N(2)-C(14)	179.57(19)
C(10)-C(9)-N(2)-C(14)	-2.3(3)
C(16)-C(15)-N(2)-C(9)	-10.8(3)
C(16)-C(15)-N(2)-C(14)	155.2(2)
C(13)-C(14)-N(2)-C(9)	71.5(3)
C(13)-C(14)-N(2)-C(15)	-94.4(3)

iii. [Rh(COD)(TMG)Cl]

Table A.11: Atomic coordinates (x 10^4) and equivalent isotropic displacement parameters ($Å^2$ x 10^3) for [Rh(COD)(TMG)Cl]. U(eq) is defined as one third of the trace of the orthogonalized U_{ij} tensor.

	x	y	z	U(eq)
C(1)	3772(6)	118(7)	858(3)	70(1)
C(2)	4783(6)	311(6)	922(3)	66(1)
C(3)	5351(7)	1386(7)	668(4)	82(2)
C(4)	5050(6)	2609(7)	884(3)	73(1)
C(5)	4355(5)	2600(6)	1430(3)	61(1)
C(6)	3345(5)	2377(6)	1381(3)	60(1)
C(7)	2801(6)	2062(7)	788(3)	71(1)
C(8)	3125(7)	970(7)	490(3)	83(2)
C(9)	3519(4)	883(4)	3130(2)	35(1)
C(10)	5041(4)	1066(6)	3751(3)	61(2)
C(11)	3408(6)	1047(7)	4260(3)	73(2)
C(12)	2445(5)	-892(5)	3377(3)	60(2)
C(13)	1954(4)	578(6)	2577(3)	56(2)
Cl(1)	4266(1)	-1229(1)	2150(1)	58(1)
N(1)	3923(3)	1438(4)	2661(2)	40(1)
N(2)	3968(3)	845(4)	3698(2)	45(1)
N(3)	2615(3)	306(4)	3093(2)	43(1)
Rh(1)	4054(1)	804(1)	1750(1)	33(1)

Table A.12: Bond distances (Å) and angles (°) for [Rh(COD)(TMG)Cl].

Atoms	Bond distances (Å)	Atoms	Angles (°)
C(1)-C(2)	1.374(10)	C(2)-C(1)-C(8)	121.9(7)
C(1)-C(8)	1.493(10)	C(2)-C(1)-Rh(1)	71.2(4)
C(1)-Rh(1)	2.104(6)	C(8)-C(1)-Rh(1)	112.2(5)
C(1)-H(1)	0.98	C(2)-C(1)-H(1)	114.7
C(2)-C(3)	1.492(10)	C(8)-C(1)-H(1)	114.7
C(2)-Rh(1)	2.110(6)	Rh(1)-C(1)-H(1)	114.7
C(2)-H(2)	0.98	C(1)-C(2)-C(3)	125.5(7)
C(3)-C(4)	1.458(9)	C(1)-C(2)-Rh(1)	70.7(4)
C(3)-H(3A)	0.97	C(3)-C(2)-Rh(1)	110.6(4)
C(3)-H(3B)	0.97	C(1)-C(2)-H(2)	113.9

C(4)-C(5)	1.504(9)	C(3)-C(2)-H(2)	113.9
C(4)-H(4A)	0.97	Rh(1)-C(2)-H(2)	113.9
C(4)-H(4B)	0.97	C(4)-C(3)-C(2)	116.5(6)
C(5)-C(6)	1.375(9)	C(4)-C(3)-H(3A)	108.2
C(5)-Rh(1)	2.100(6)	C(2)-C(3)-H(3A)	108.2
C(5)-H(5)	0.98	C(4)-C(3)-H(3B)	108.2
C(6)-C(7)	1.514(9)	C(2)-C(3)-H(3B)	108.2
C(6)-Rh(1)	2.104(6)	H(3A)-C(3)-H(3B)	107.3
C(6)-H(6)	0.98	C(3)-C(4)-C(5)	114.6(6)
C(7)-C(8)	1.413(9)	C(3)-C(4)-H(4A)	108.6
C(7)-H(7A)	0.97	C(5)-C(4)-H(4A)	108.6
C(7)-H(7B)	0.97	C(3)-C(4)-H(4B)	108.6
C(8)-H(8A)	0.97	C(5)-C(4)-H(4B)	108.6
C(8)-H(8B)	0.97	H(4A)-C(4)-H(4B)	107.6
C(9)-N(1)	1.298(6)	C(6)-C(5)-C(4)	123.1(6)
C(9)-N(3)	1.362(6)	C(6)-C(5)-Rh(1)	71.1(4)
C(9)-N(2)	1.370(6)	C(4)-C(5)-Rh(1)	112.6(4)
C(10)-N(2)	1.459(7)	C(6)-C(5)-H(5)	114.2
C(10)-H(10A)	0.96	C(4)-C(5)-H(5)	114.2
C(10)-H(10B)	0.96	Rh(1)-C(5)-H(5)	114.2
C(10)-H(10C)	0.96	C(5)-C(6)-C(7)	125.2(6)
C(11)-N(2)	1.445(7)	C(5)-C(6)-Rh(1)	70.7(4)
C(11)-H(11A)	0.96	C(7)-C(6)-Rh(1)	110.9(4)
C(11)-H(11B)	0.96	C(5)-C(6)-H(6)	114
C(11)-H(11C)	0.96	C(7)-C(6)-H(6)	114
C(12)-N(3)	1.450(7)	Rh(1)-C(6)-H(6)	114
C(12)-H(12A)	0.96	C(8)-C(7)-C(6)	115.4(6)
C(12)-H(12B)	0.96	C(8)-C(7)-H(7A)	108.4
C(12)-H(12C)	0.96	C(6)-C(7)-H(7A)	108.4
C(13)-N(3)	1.456(7)	C(8)-C(7)-H(7B)	108.4
C(13)-H(13A)	0.96	C(6)-C(7)-H(7B)	108.4
C(13)-H(13B)	0.96	H(7A)-C(7)-H(7B)	107.5
C(13)-H(13C)	0.96	C(7)-C(8)-C(1)	116.5(6)
Cl(1)-Rh(1)	2.3773(14)	C(7)-C(8)-H(8A)	108.2
N(1)-Rh(1)	2.097(4)	C(1)-C(8)-H(8A)	108.2
		C(7)-C(8)-H(8B)	108.2
		C(1)-C(8)-H(8B)	108.2
		H(8A)-C(8)-H(8B)	107.3
		N(1)-C(9)-N(3)	122.3(4)
		N(1)-C(9)-N(2)	122.4(5)
		N(3)-C(9)-N(2)	115.3(4)

N(2)-C(10)-H(10A)	109.5
N(2)-C(10)-H(10B)	109.5
H(10A)-C(10)-H(10B)	109.5
N(2)-C(10)-H(10C)	109.5
H(10A)-C(10)-H(10C)	109.5
H(10B)-C(10)-H(10C)	109.5
N(2)-C(11)-H(11A)	109.5
N(2)-C(11)-H(11B)	109.5
H(11A)-C(11)-H(11B)	109.5
N(2)-C(11)-H(11C)	109.5
H(11A)-C(11)-H(11C)	109.5
H(11B)-C(11)-H(11C)	109.5
N(3)-C(12)-H(12A)	109.5
N(3)-C(12)-H(12B)	109.5
H(12A)-C(12)-H(12B)	109.5
N(3)-C(12)-H(12C)	109.5
H(12A)-C(12)-H(12C)	109.5
H(12B)-C(12)-H(12C)	109.5
N(3)-C(13)-H(13A)	109.5
N(3)-C(13)-H(13B)	109.5
H(13A)-C(13)-H(13B)	109.5
N(3)-C(13)-H(13C)	109.5
H(13A)-C(13)-H(13C)	109.5
H(13B)-C(13)-H(13C)	109.5
C(9)-N(1)-Rh(1)	128.4(3)
C(9)-N(2)-C(11)	121.7(5)
C(9)-N(2)-C(10)	119.7(4)
C(11)-N(2)-C(10)	114.8(5)
C(9)-N(3)-C(12)	121.5(5)
C(9)-N(3)-C(13)	119.4(4)
C(12)-N(3)-C(13)	114.2(5)
N(1)-Rh(1)-C(5)	91.4(2)
N(1)-Rh(1)-C(1)	164.7(2)
C(5)-Rh(1)-C(1)	93.2(3)
N(1)-Rh(1)-C(6)	93.2(2)

C(5)-Rh(1)-C(6)	38.2(2)
C(1)-Rh(1)-C(6)	81.6(3)
N(1)-Rh(1)-C(2)	157.2(2)
C(5)-Rh(1)-C(2)	82.1(3)
C(1)-Rh(1)-C(2)	38.1(3)
C(6)-Rh(1)-C(2)	95.0(3)
N(1)-Rh(1)-Cl(1)	88.20(12)
C(5)-Rh(1)-Cl(1)	162.02(19)
C(1)-Rh(1)-Cl(1)	91.8(2)
C(6)-Rh(1)-Cl(1)	159.8(2)
C(2)-Rh(1)-Cl(1)	91.3(2)

Table A.13: Anisotropic displacement parameters ($Å^2$ x 10^3) for [Rh(COD)(TMG)Cl]. The Anisotropic displacement factor exponent takes the form: $-2\pi^2(h^2a^*2U_{11} + \ldots + 2hka^*b^*U_{12})$.

	U_{11}	U_{22}	U_{33}	U_{23}	U_{13}	U_{12}
C(1)	89(2)	68(2)	52(2)	-10(2)	2(2)	6(2)
C(2)	89(2)	64(2)	46(2)	-12(2)	3(2)	6(2)
C(3)	101(3)	67(2)	77(3)	-10(2)	19(2)	4(2)
C(4)	92(3)	65(2)	62(2)	-7(2)	12(2)	1(2)
C(5)	84(2)	47(2)	54(2)	0(2)	4(2)	7(2)
C(6)	84(2)	47(2)	51(2)	5(2)	3(2)	7(2)
C(7)	88(2)	70(2)	56(2)	-3(2)	0(2)	6(2)
C(8)	105(3)	77(2)	66(2)	-12(2)	-10(2)	15(2)
C(9)	42(3)	27(2)	36(2)	-3(2)	4(2)	1(2)
C(10)	53(3)	78(4)	54(3)	16(3)	-14(3)	-19(3)
C(11)	83(5)	97(6)	41(3)	-4(3)	14(3)	-12(4)
C(12)	54(3)	49(3)	77(4)	8(3)	7(3)	-11(3)
C(13)	43(3)	67(4)	58(3)	-3(3)	-4(3)	-5(3)
Cl(1)	73(1)	33(1)	68(1)	2(1)	4(1)	15(1)
N(1)	51(3)	34(2)	35(2)	-3(2)	4(2)	-6(2)
N(2)	48(2)	54(3)	35(2)	1(2)	0(2)	-12(2)
N(3)	40(2)	40(2)	48(2)	-1(2)	2(2)	-2(2)
Rh(1)	38(1)	28(1)	34(1)	-6(1)	-1(1)	2(1)

Table A.14: Hydrogen coordinates (x 10^4) and isotropic displacement parameters ($Å^2$ x 10^3) for [Rh(COD)(TMG)Cl].

	x	y	z	U(eq)
H(1)	3572	-755	844	83

H(2)	5176	-453	951	79
H(3A)	6053	1272	766	98
H(3B)	5289	1371	222	98
H(4A)	4725	3043	547	87
H(4B)	5646	3073	993	87
H(5)	4535	3191	1755	74
H(6)	2937	2835	1679	72
H(7A)	2094	1981	879	85
H(7B)	2878	2749	504	85
H(8A)	3490	1205	121	99
H(8B)	2538	512	358	99
H(10A)	5372	759	3389	92
H(10B)	5296	646	4108	92
H(10C)	5162	1939	3789	92
H(11A)	2705	1059	4167	110
H(11B)	3600	1824	4439	110
H(11C)	3546	390	4546	110
H(12A)	2450	-1523	3065	90
H(12B)	1807	-890	3581	90
H(12C)	2963	-1056	3672	90
H(13A)	1977	1448	2487	84
H(13B)	1282	345	2681	84
H(13C)	2168	119	2221	84

Table A.15: Torsion angles (°) for [Rh(COD)(TMG)Cl].

Atoms	Torsion angles (°)
C(8)-C(1)-C(2)-C(3)	2.9(10)
Rh(1)-C(1)-C(2)-C(3)	-102.1(6)
C(8)-C(1)-C(2)-Rh(1)	105.0(6)
C(1)-C(2)-C(3)-C(4)	60.3(10)
Rh(1)-C(2)-C(3)-C(4)	-20.2(9)
C(2)-C(3)-C(4)-C(5)	12.1(11)
C(3)-C(4)-C(5)-C(6)	-79.3(9)
C(3)-C(4)-C(5)-Rh(1)	2.1(9)
C(4)-C(5)-C(6)-C(7)	2.6(10)
Rh(1)-C(5)-C(6)-C(7)	-102.5(6)
C(4)-C(5)-C(6)-Rh(1)	105.1(6)
C(5)-C(6)-C(7)-C(8)	60.3(10)
Rh(1)-C(6)-C(7)-C(8)	-20.3(8)

C(6)-C(7)-C(8)-C(1)	14.0(11)
C(2)-C(1)-C(8)-C(7)	-81.8(10)
Rh(1)-C(1)-C(8)-C(7)	-0.8(10)
N(3)-C(9)-N(1)-Rh(1)	-45.8(7)
N(2)-C(9)-N(1)-Rh(1)	134.8(4)
N(1)-C(9)-N(2)-C(11)	136.8(6)
N(3)-C(9)-N(2)-C(11)	-42.6(7)
N(1)-C(9)-N(2)-C(10)	-20.1(8)
N(3)-C(9)-N(2)-C(10)	160.5(5)
N(1)-C(9)-N(3)-C(12)	137.4(5)
N(2)-C(9)-N(3)-C(12)	-43.2(7)
N(1)-C(9)-N(3)-C(13)	-16.5(7)
N(2)-C(9)-N(3)-C(13)	162.9(5)

Table A.16: Hydrogen bond distances (Å) and angles (°) for [Rh(COD)(TMG)Cl].

D-H...A	d(D-H)	d(H...A)	d(D...A)	<(DHA)
C(11)-H(11A)...N(3)	0.96	2.47	2.855(8)	103.9
C(12)-H(12C)...N(2)	0.96	2.45	2.855(7)	104.9

Symmetry transformations used to generate equivalent atoms: x, y, z .

Appendix B

i. [Rh(COD)(DBU)Cl]

The DBU substitution reaction between [Rh(COD)(DBU)Cl] and 4-dimethylaminopyridine (DMAP) as entering ligand were followed. The reaction was performed at three temperatures (15.1, 25.1 and 34.9 ºC) and the concentration of the rhodium complex was kept constant at 0.359 mM throughout.

Table B.1: The k_{obs} values for the DMAP substitution reaction with [Rh(COD)(DBU)Cl] at different temperatures. [Rh] = 0.359 mM, [DMAP] = 3.52 – 35.20 mM, λ = 320 nm.

DMAP (mM)	15.1 °C	25.1 °C	34.9 °C
3.52	13.8 ± 0.1	15.3 ± 0.1	30.3 ± 0.9
7.04	20.5 ± 0.1	26.2 ± 0.1	33.5 ± 0.2
14.08	32.7 ± 0.1	43.9 ± 0.3	58.4 ± 0.7
21.28	44.8 ± 0.2	55.9 ± 0.3	75.5 ± 0.7
28.24	55.4 ± 0.2	71.8 ± 0.2	99 ± 1
35.20	64.4 ± 0.3	84.9 ± 0.2	111 ± 1

ii. [Rh(COD)(TMG)Cl]

The TMG substitution reaction between [Rh(COD)(TMG)Cl] and 4-dimethylaminopyridine (DMAP) as entering ligand were followed. The reaction was performed at three temperatures (15.1, 25.2 and 35.0 ºC) and the concentration of the rhodium complex was kept constant at 0.359 mM throughout.

Table B.2: The k_{obs} values for the DMAP substitution reaction with [Rh(COD)(TMG)Cl] at different temperatures. The value in brackets shows the error on the last digit. [Rh] = 0.370 mM, [DMAP] = 3.93 – 38.72 mM, λ = 320 nm.

DMAP (mM)	15.1 °C	25.2 °C	35.0 °C
3.93	95.3 ± 0.3	131.4 ± 0.6	160.2 ± 0.8
7.78	163.5 ± 0.6	228 ± 1	308 ± 2
15.55	307 ± 1	438 ± 4	528 ± 6
23.25	446 ± 4	585 ± 7	775 ± 17
31.02	566 ± 5	762 ± 13	918 ± 23
38.72	733 ± 13	908 ± 15	1149 ± 33